Designing Quantum Dot Interfaces for Photoredox Catalysis

Florence Yimin Dou

A dissertation

submitted in partial fulfillment of the

requirements for the degree of

Doctor of Philosophy

University of Washington

2023

Reading Committee:

Brandi M. Cossairt, Chair

Dianne J. Xiao

Cody W. Schlenker

Program Authorized to Offer Degree:

Chemistry

University of Washington

Abstract

Designing Quantum Dot Interfaces for Photoredox Catalysis

Florence Yimin Dou

Chair of the Supervisory Committee:
Brandi M. Cossairt
Chemistry

Chemical manufacturing accounts for 10% of total global energy consumption and 7% of greenhouse emissions. Thermodynamically uphill reactions may be driven by photoredox catalysts under ambient conditions, converting solar to chemical energy. Semiconductor quantum dots (QDs) are efficient photoredox catalysts due to their high absorptivity and easily tuneable redox potentials. They are routinely used in the hydrogen evolution reaction, but there remains much to be understood when applying QDs to organic synthesis. In this work, we present several strategies to synthesise more active QD photocatalysts for organic reactions via modulation of the semiconductor interface.

In the first chapter, we explore catalyst speciation under reaction conditions and elucidate a mechanism for unwanted reactions happening at the catalyst surface that affect its stability. In the second chapter, we make more stable and active catalysts via ligand shell engineering using charge

transfer mediators. In the third chapter, we use infrared (IR) spectroscopy to measure relative binding energies of common aliphatic ligands on nanocluster surfaces, which appear to be more labile than previously thought. Lastly in chapter four, we make anisotropic heterostructures with long-lived excited states and study their optoelectronic properties and charge transfer rates to molecular acceptors. This work increases our atomistic understanding of mechanisms involved in QD organic photoredox catalysis and provides design principles for making stable and more active catalysts.

ACKNOWLEDGEMENTS

I left this part for last because I knew it would be the hardest part for me to write, emotionally. It really takes a village! There are so many people without whom I could have never finished this journey. First and foremost, I need to thank Brandi. I picked her lab based on my first impressions in her office of her being one of the most caring PI's that stood out to me on my visits, and it was the right decision. We have had an eventful journey together, filled with a lot of learning moments and growth for both of us, and I think we can both pinpoint the moment where we grew closer as mentor and mentee. Brandi has always had my back and believed in me and has been incredibly understanding and supportive over the years. There could have been no other lab for me and if I had to do it all over again knowing what I know now, I would 1000 % choose the same group again.

My home system has also been integral to my support network. I didn't get to see my family much, especially because of the pandemic, and those moments were particularly hard for me not to be able to go home. But they have always been unwaveringly supportive, on the phone or over WhatsApp, trying their best to understand the research summaries on the lab website or when I sent them my first paper. I was so impressed the first time they precisely described the lab's research back to me in Cantonese! I appreciate them asking every time we called if I've made any more discoveries and if I'm writing anything new for magazines.

I really want to give a special shout out to the Chemistry Department at Trinity College. I have always told anyone who asked that the reason I chose to become a chemistry major was because of the Professors in that department. It was one of the most special environments I've ever been in. Some of my favourite Profs are in Clement, and I will never forget when Prof. Morrison took

us all in during Thanksgiving, and the way Prof. Kovarik researched UK graduate schools and wrote up a summary for me when I was considering applying, and the tubing trip we all took together during the summer. I miss the annual Chemis-tree decorating, and I miss Prof. Curran's cheesy, cheeky sense of humour and I wish I could be his student again with the new skills and knowledge that I've picked up and give it another go. I also know that the environment was in large part due to his tenure as Chair. The Chemistry Department was amazing at Trinity and so warm, inviting, and *together*. It will always hold an extremely special place in my heart.

I save my labmates for last because they were the ones who got me through grad school day by day. I should start with David and Nayon – the other reason I joined the Cossairt group. When I first met David in the chemistry stockroom, he handed me the XS lab coat he was thinking of taking, and it would be the first of many hand-me-downs he would later come to pass on to me. At the time I had barely known him, but he kindly sat down with me for over an hour at a coffee shop when I was torn over what lab to join. He has always been someone that I trust completely and unconditionally. I am sorry I stole your nook in the office, and that all you give is "doo doo doo", but I will always cherish the stupid silly moments we had together at work. David also taught me a lot about being a scientist, and I always admired how careful, thoughtful, and knowledgeable he was as a grad student. He is still the example in lab – if it has his name on it, it can be trusted completely. I am forever grateful to have made a lifelong friend at work.

When I rotated I immediately formed a connection with David and Nayon because they were the only Asians in the lab, and looking back now I am so grateful for the effort they put in to make me feel welcome. Nayon went above and beyond to welcome me both in lab and into her personal life, taking me out to our first dinner together at Annapurna, and also to New Years' at Ather's. I learned so much from her as a scientist, an organizer, a friend, and a voracious snacker and

restaurateur. I am grateful for the friendship and bond that we formed and how much it meant being the only two women of colour in the lab at the time (so she was the first!!) What a trendsetter and role model.

My third ride-or-die was Hao. I can't even begin to describe how grateful I am for Hao. After Nayon and David left, he really pushed me through the second half of my PhD. Hao goes *above* above and beyond for me. We have shared so many fun moments and experiences together, always scheming, and travelling together to the Laver Cup!! I never thought I would meet someone who was also in the niche club of liking both tennis and Taylor Swift. Hao has always been there to support me unconditionally, and I am so excited to see what the future has in store for this star.

My first mentor in grad school was Michael and I will also be forever grateful to him for all he taught me and all the tetrapods we made together. Really early on, I was so touched by how late Michael would stay to finish up things that I had started, and how he would already defend me fiercely. We grew to become friends outside of grad school through fantasy football, where I still consider him my mentor (along with Ben Leipzig), and had such a fun and memorable group trip together in Maine for Danielle's wedding.

Ian and Cecilia were part of the core Left Office degenerate early 90's crew that I remember so fondly. Cecilia has been there for me in my weakest moments and I am eternally grateful to her for helping me process my accident. She is endlessly kind and funny and dorky and has been supportive since day one. Ramsess was not in the Cossairt group, but I would have never made it through grad school without him. Fittingly, I remember meeting him as early as our visit weekend, where we formed an instant connection. He has been there for me ever since, sharing the same sense of humour, and experiencing life together!

To my partner Sidney, who I met on my very first day in Seattle. How fitting was it that we practiced our rotation talks to each other, and ended grad school defending together. Sidney has been a consistent source of joy, support, love, understanding, and patience at home since day one. I have learned so much about the world, using my voice, and caring for others from him. I am also lucky to have witnessed and been inspired by his genuine curiosity and passion for science. I am excited for our next steps in life together.

TABLE OF CONTENTS

Chapter 1. Introduction 1
1.1 Photoredox Catalysis 1
1.2 QDs and Hydrogen Evolution Reaction 2
1.3 QDs and Organic Photoredox Catalysis 4
1.4 This Work 6
1.5 References 6
Chapter 2. Is Quantum Dot Photocatalysis Really Homogeneous? 10
2.1 Introduction 10
2.2 CdS Degradation During Photocatalysis 11
2.3 Conclusions 18
2.4 Experimental 19
2.4.1 Materials 19
2.4.2 Synthesis of CdS QDs 19
2.4.3 Photocatalysis 20
2.4.4 XRD and Scherrer analysis 22
2.4.5 Characterisation methods 23
2.5 References 23
Chapter 3. Effect of a redox-mediating ligand shell on photocatalysis by CdS quantum dots 27
3.1 Introduction 27
3.2 Ligand Exchanges on CdS Quantum Dots 29
3.2.1 Ferrocene carboxylic acids 29
3.2.2 Phenazine-1-carboxylic acid 31
3.2.3 2-(3,5-di-tert-butylphenyl)acetic acid 32
3.3 Catalysis Using Redox-Active and Redox-Innocent Ligands 33
3.3.1 Photocatalytic model reaction 33
3.3.2 Effect of redox-innocent ligand exchange on catalysis 34
3.3.3 Effect of hole-mediating ligands on catalysis 35
3.3.4 Effect of electron-mediating ligands on catalysis 35
3.4 Rationalising Differences in Catalysis 36
3.4.1 Ligand steric profiles 36
3.4.2 Charge transfer from QD to Fc 37
3.4.3 Charge transfer from Fc to PhPyr 42
3.4.4 Effect of electron-trapping on hole transfer 45

3.5 STABILITY 47
3.6 CONCLUSIONS 48
3.7 EXPERIMENTAL 49
3.7.1 Materials 49
3.7.2 Synthesis of cadmium oleate 50
3.7.3 Synthesis of CdS QDs 50
3.7.4 Synthesis of 3,5-di-tert-butylphenylacetic acid 51
3.7.5 Photocatalysis 52
3.7.6 Electrochemical titrations 53
3.7.7 Electrochemical simulations 54
3.7.8 Transient absorption 54
3.7.9 Photoluminescence quenching 57
3.7.10 Characterisation methods 58
3.8 REFERENCES 58
Chapter 4. Probing Ligand Binding on Nanocrystal Surfaces using Temperature-Dependent FTIR and Ultrafast IR Spectroscopy 63
4.1 INTRODUCTION 63
4.2 InP MAGIC-SIZED CLUSTERS 66
4.2.1 Temperature dependent FTIR 66
4.2.2 Markov chain Monte Carlo Global Fitting 70
4.2.3 Interpretation of Fitted FTIR Parameters 74
4.3 CONCLUSIONS 77
4.4 EXPERIMENTAL 78
4.4.1 InP MSC Synthesis and Characterisation 78
4.4.2 FTIR Measurements 79
4.4.3 MCMC Sampling 79
4.5 REFERENCES 80
Chapter 5. Seeded Growth of Nanoscale Semiconductor Tetrapods: Generality and Cation Exchange 86
5.1 INTRODUCTION 86
5.2 GENERAL SYNTHESIS OF CORE/CdS TETRAPODS WITH TWO DISTINCT ARM MORPHOLOGIES 88
5.3 EVIDENCE FOR CATION EXCHANGE 92
5.4 CONCLUSIONS 94
5.5 EXPERIMENTAL 95

5.5.1 Materials 95
5.5.2 Synthesis of ZnTe QDs 96
5.5.3 Synthesis of Copper Indium Sulphide QDs 97
5.5.4 Synthesis of Spherical InP QDs 97
5.5.5 Synthesis of Tetrahedron InP and InP/ZnS QDs 98
5.5.6 Synthesis of InP/ZnSeS QDs 98
5.5.7 Synthesis of Cd_3P_2 QDs 99
5.5.8 Synthesis of Tetrapods with CdS Arms 99
5.5.9 Characterisation methods 100
5.6 REFERENCES 101

LIST OF FIGURES

Figure 1.1. Thermodynamics of uphill and downhill photocatalysis: (a) uphill process with $\Delta G > 0$, (b) downhill process with $\Delta G < 0$. Reprinted with permission from reference 1. Copyright 2018 American Chemical Society. 1

Figure 1.2. Diagram of relaxation pathways for a photo-excited QD – 1) intraband relaxation, 2) carrier trapping, 3) electron-hole recombination. 3

Figure 1.3. Schematic of photocatalytic proton reduction with a QD, illustrating relevant photoinduced charge transfer processes necessary to the photocatalytic process: electron transfer (ET) to the catalyst and hole transfer to a molecular acceptor (A), to maintain charge balance in the system following ET. Ligands typically coat the surface of the QD to maintain colloidal stability, with a common ligand, mercaptopropionic acid, shown here. Reprinted from reference 12, with the permission of AIP Publishing..... 4

Figure 1.4. Number of publications about QD photoredox catalysis for organic synthesis since 2000..... 5

Scheme 2.1. Proposed mechanism of reductive dehalogenation of 2-bromobenzonitrile (blue) by CdS QDs with DIPEA as a sacrificial hole quencher.1**Error! Bookmark not defined.**

Scheme 2.2 Optimised reaction conditions for photocatalysis.1**Error! Bookmark not defined.**

Figure 2.1. Conversion of 2-bromobenzonitrile to benzonitrile over time. (A) Quantification by ^{1}H NMR spectroscopy. (B) Image showing complete depletion of CdS absorbance accompanied by black precipitate formation over time (left to right). 13

Figure 2.2. XRD patterns of precipitate over the course of the reaction. (A) Precipitate from 0-7 hours. (B) Precipitate showing formation of DIPAB salt. (C) Precipitate showing formation of cadmium metal using DIPEA or tripropylamine as the hole quencher for the reaction. 14

Figure 2.3. TEM images of reaction mixture after catalysis. (A) Bright field image of faceted microcrystals formed during catalysis. (B) STEM image of microcrystals. (C) EDS elemental mapping of microcrystals showing primarily Cd co-localisation. 15

Figure 2.4. Sulphur XPS measurements referenced to carbon. (A) CdS before catalysis and (B) Precipitate after catalysis. 16

Figure 2.5. Illumination of QDs with reagents. (A) UV-vis absorption of QDs after 2 hours of illumination under catalytic conditions. (B) Image of reaction mixture of QDs, DIPEA and MV^{2+} after 2 hours of illumination. 17
Figure 2.6. Properties of oleate-capped CdS QDs. (A) Absorption and photoluminescence spectra. (B) TEM image. (C) XRD pattern. 20
Figure 2.7. ^{1}H NMR of reaction mixture after 24 hours at literature conditions. NMR shows full conversion to product along with oleate signal between 5-6 ppm. Inset shows formation of black precipitate after catalysis. C_6D_6, 500 MHz, d1=10s. 21
Figure 2.8. ^{1}H NMR of reaction progress at 0.006 mol% loading under optimised conditions showing disappearance of starting material (blue) and growth of product (yellow) over time. C_6D_6, 500 MHz, d1=2s. 21
Figure 2.9. ^{1}H NMR before catalysis (blue) and after catalysis (red) showing increase in unbound oleate peak concurrent with the formation of product. C_6D_6, 500 MHz, d1=10s. 22
Figure 2.10. ^{1}H NMR over the course of the reaction showing (A) DIPAB ammonium proton (blue) and (B) acetone by-product (yellow). C_6D_6, 500 MHz, d1=2s. 22
Figure 3.1. CVs of 1 mM (A) Fc-(COOH)2, (B) Fc-COOH, and (C) Fc-CH2COOH titrated with 0.024 equivalents of CdS QDs (black arrow); 0.15 M [NBu4][PF6], THF, glassy carbon working, Pt auxiliary, and Ag pseudo reference electrodes, 10 mV/s. 30
Figure 3.2. Absorbance profiles of CdS QDs exchanged with 100 equivalents of Fc ligand and purified by column chromatography 31
Figure 3.3. (A) Molecular structure of phenazine-1-carboxylic acid. (B) 1H NMR of titration of CdS QDs with increasing amounts of ligand showing decreasing bound oleate and increasing unbound oleate ligands. C6D6, 500 MHz, d1=10s. (C) CV of phenazine-1-carboxylic acid; 0.15 M [NBu4][PF6], MeCN, glassy carbon working, Pt auxiliary, and Pt reference electrodes, 100 mV/s 32
Figure 3.4. (A) Molecular structure of 2-(3,5-di-tert-butylphenyl)acetic acid. (B) 1H NMR of tsitration of CdS QDs with increasing amounts of ligand showing decreasing bound oleate and increasing unbound oleate ligands. C6D6, 500 MHz, d1=10s 32
Scheme 3.1. Proposed reaction mechanism for carbon–carbon coupling of 1-phenylpyrrolidine to phenyl trans-beta-styryl sulfone based on reports from Noble and Macmillan and Zhang et al 33

Scheme 3.2. Optimised reaction conditions for this study 34
Figure 3.5. Product quantification after 30 minutes under photocatalytic conditions of CdS QDs exchanged with increasing equivalents of 2-(3,5-di-tert-butylphenyl)acetic acid 34
Figure 3.6. Catalytic results as a function of ligand identity and surface coverage. (A) Catalysis results of CdS QDs ligated with ten equivalents of Fc ligands. (B) Catalysis results at 30-min timepoint of CdS QDs ligated with increasing equivalents of Fc ligands 35
Figure 3.7. Catalytic results using phenazine-1-carboxylic acid (phenazine-COOH) ligand. (A) Catalysis using CdS dots ligated with ten equivalents of phenazine-COOH. (B) Catalysis results at 30-min timepoints of CdS dots ligated with increasing equivalents of phenazine ligand..... 36
Figure 3.8. TA spectra of (A-B) CdS, (C-D) CdS + Fc-$(COOH)_2$, (E-F) CdS + Fc-COOH, (G-H) CdS + Fc-CH_2COOH in the fs - ns regime (left column) and ns - µs regime (right column) 38
Figure 3.9. Weighted average charge transfer rates of Fc-$(COOH)_2$ (green), Fc-COOH (blue), and Fc-CH_2COOH (red) fit from TA spectra 40
Figure 3.10. Charge transfer from CdS QD to Fc ligands probed via fluorescence quenching. (A) Stern–Volmer plot for quenching of CdS QD fluorescence by successive addition of Fc-$(COOH)_2$ (green), Fc-COOH (blue), and Fc-CH_2COOH (red) (0–20 equivalents relative to CdS) monitored at 470 nm. (b) Stern–Volmer plot for quenching of CdS QD fluorescence monitored at 720 nm 41
Figure 3.11. Driving force and charge transfer measurements from Fc ligands to PhPyr. (A) CVs of 0.5 mM Fc ligands and PhPyr; 0.15 M [NBu4][PF6], THF, glassy carbon working, Pt auxiliary, and Pt reference electrodes, 100 mV/s. (B) Estimated driving force of hole transfer from Fc^+ to PhPyr calculated from CVs. (C) Stern–Volmer plot for fluorescence quenching of CdS QDs ligated with oleate (black), Fc-$(COOH)_2$ (green), Fc-COOH (blue), and Fc-CH_2COOH (red) by successive addition of PhPyr (0–2500 equivalents relative to CdS) monitored at 470 nm [1]..... 42
Figure 3.12. Weighted average charge transfer rates of QDs ligated with 10 eq of Fc ligands in the absence (filled triangle) and presence (empty triangle) or PhPyr 44
Figure 3.13. Decay kinetics of ground state bleach at 434 nm of CdS (blue) and CdS in the presence of phenazine (red) in the (A) fs - ns and (B) ns - µs regime 45

Figure 3.14. Decay kinetics of photoinduced absorption at 540 nm of CdS (blue) and CdS in the presence of phenazine (red) in the (A) fs – ns and (B) ns - μs regime 46
Figure 3.15. ^{1}H NMR of vinyl proton region of CdS QDs with native oleate ligands during catalysis, showing etching behaviour over time as product is formed. C_6D_6, 500 MHz, d1=10s 47
Figure 3.16. Stability and surface chemistry characterization during and after catalysis. (A) DLS measurements of CdS with different ligands before and after catalysis. (B) Ratio of bound vs unbound oleate ligands fit from ^{1}H NMR of QDs during catalysis and in solvent under illumination 47
Scheme 3.3. Different charge transfer pathways explored in this study and effects on catalysis 48
Figure 3.17. Properties of oleate-capped CdS QDs. (A) Absorption and photoluminescence spectra. (B) TEM image 51
Figure 3.18. Representative ^{1}H NMR spectrum in C_6D_6 (red) used for quantification of product using 1,3,5-trimethoxybenzene as an internal standard. Starting material shown in blue (1-phenylpyrrolidine) and green (phenyl trans-styryl sulfone), red spectrum was taken after photocatalysis. A 500 MHz instrument with d1=10 s was used 52
Figure 3.19. TA spectra of (A-B) CdS + PhPyr, (C-D) CdS + Fc-$(COOH)_2$ + PhPyr, (E-F) CdS + Fc-COOH + PhPyr, (G-H) CdS + Fc-CH_2COOH + PhPyr in the fs - ns regime (left column) and ns - μs regime (right column) 55
Figure 3.20. TA spectra of (A-B) CdS and (C-D) CdS + phenazine-1-carboxylic acid in the fs - ns regime (left column) and ns - μs regime (right column) 56
Figure 3.21. Raw PL quenching spectra of CdS QDs titrated with (A) Fc-$(COOH)_2$, (B) Fc-COOH, (C) Fc-CH_2COOH, (D) PhPyr 57
Figure 4.1. Temperature dependent FTIR spectra of (A) myristic acid and (B) indium myristate 68
Figure 4.2. Representative FTIR spectra from the temperature-dependent measurement of myristate-capped InP MSCs spanning from 25 °C (bottom) to 100 °C (top) in increments of 15 °C, demonstrating changes that occur with increasing temperature along with peak assignment of the asymmetric carboxylate stretching region. From left to right, binding

groups shown include chelating (yellow), bridging syn–anti (green), bridging syn–syn (light blue), monodentate (dark blue), and dative (pink)..... 69
Figure 4.3. (a) Depiction of the MCMC global fit process. For a given subset of walkers, stretch moves are randomly generated to propose new positions in parameter space. These new walker positions are used to generate the Gaussian peaks corresponding to those parameters of means μ_i and widths σ_i, with a temperature-dependent broadening factor β. These peaks are then fit by least squares to the measured FTIR spectra at each temperature point. The log likelihood of this fit is taken as the negative sum of squared residuals; combined with the prior probabilities of the parameters, the resulting posterior probability is used to stochastically decide whether to accept or reject the new walker positions. The walker ensemble is then updated, and the algorithm iterates to the next subset of walkers and repeats the process. (b) Global MCMC fit results (blue lines) for the temperature-dependent InP MSC FTIR spectra (orange lines). The standard deviation across the top 15,000 fits is depicted by the blue shaded area..... 73
Figure 4.4. (a) Differences of the log of peak areas with respect to the monodentate binding motif, plotted against inverse thermal energy with units of inverse wavenumbers. Markers and error bars represent mean and standard deviation at each temperature point across sampled global fits comprising the top 15,000 posterior probabilities. Lighter lines depict log area differences from the fits corresponding to the 100 highest posterior probabilities. Note the highly correlated error between temperature points, which is not conveyed from the error bars alone. While log area differences might vary in magnitude between fits, the temperature trends stay rather consistent. Arrow denotes data points above 40 °C (black dashed line), which demonstrate near linear behavior and were fit using linear regression. (b) Extracted slopes from linear regressions of the 45–110 °C regime in (a). These values correspond to energy differences relative to the monodentate binding motif, assuming an equilibrated system following Boltzmann statistics. Markers and error bars respectively denote mean and standard deviation of slopes taken from sampled global fits comprising the top 15,000 posterior probabilities 75
Figure 4.5. UV-vis absorption of InP MSC after purification 78
Scheme 5.1. General reaction conditions for the synthesis of thick and thin arm tetrapods. TEM of example thick and thin arm tetrapods grown from ZnTe seeds..... 89

Figure 5.1. TEM images of thick (left column) and thin (right column) tetrapods grown from (A-B) ZnTe, (C-D) 3 nm CuInS2, (E-F) 6 nm CuInS2 and (G-H) spherical InP QD seeds 90
Figure 5.2. TEM images of thick (left column) and thin (right column) tetrapods grown from (A-B) tetrahedron InP, (C-D) InP/ZnSeS, (E-F) InP/ZnS and (G-H) Cd_3P_2..... 91
Figure 5.3. Absorbance and emission spectra of (A) thick and (B) thin CdS arms..... 92
Figure 5.4. ICP-OES of indium and zinc over the course of tetrapod growth..... 93
Figure 5.5. Emission of Cd_3P_2 nanocrystals, Cd_3P_2/CdS tetrapods, and CdS arms with thick and thin arm morphologies. Strong emission features from the Cd_3P_2 core are observed at 1100 nm (1.13 eV) prior to tetrapod assembly. This emission shifts up to 82 meV when incorporated into tetrapods. 94

LIST OF TABLES

Table 2.1. Crystallite sizes of CdS over the course of the reaction calculated by XRD Scherrer equation. 23
Table 3.1. Equilibrium binding constants for reduced and oxidised forms of Fc ligands to CdS 30
Table 3.2. Fitted lifetimes from TA spectra 39
Table 3.3. Stern-Volmer quenching constants from CdS QDs titrated with Fc ligands and PhPyr 41
Table 3.4. Fitted lifetimes from TA spectra 45
Table 4.1. Extracted parameters from the MCMC global fit on a temperature series of FTIR spectra from an InP MSC sample 74
Table 4.2. Summary of relative binding energies extracted from slopes of temperature-dependent log area differences 76
Table 5.1. Arm dimensions of library of 16 tetrapod heterostructures 89

Chapter 1. Introduction

1.1 PHOTOREDOX CATALYSIS

The photocatalysis process is generally understood as the absorption of light by a catalyst to form an excited state, interaction of the excited state with a reaction partner to form a high-energy intermediate, the induction of a chemical transformation by the reaction intermediate, finally followed by regeneration of the catalyst after each cycle of interaction. There are slight nuances depending on the thermodynamics of the chemical transformation being catalysed – if the reaction is thermodynamically uphill ($\Delta G > 0$), the process is technically defined as "photosynthesis" and if the reaction is downhill ($\Delta G < 0$), the process is a "photocatalysis" (Figure 1.1), however the term has come to be used interchangeably.[1] Examples of important thermodynamically uphill reactions studied include water splitting, carbon dioxide reduction, and nitrogen fixation in solar to chemical energy fuels conversion.[2]

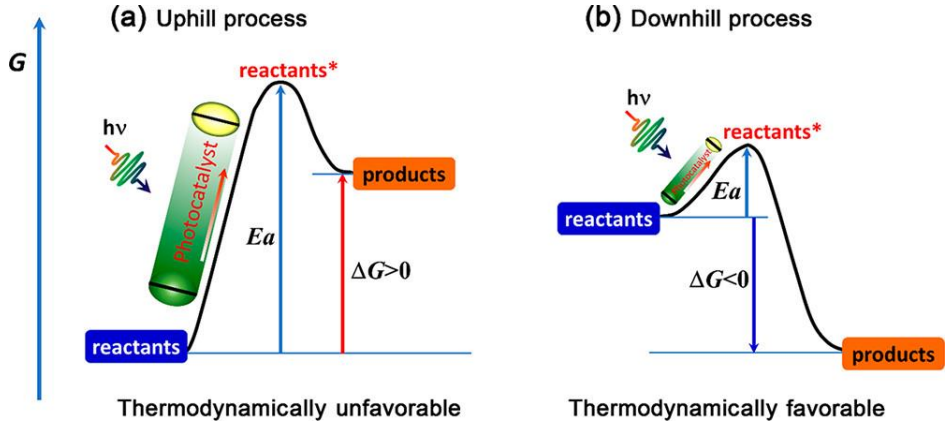

Figure 1.1. Thermodynamics of uphill and downhill photocatalysis: (a) uphill process; (b) downhill process. Reprinted with permission from reference (1). Copyright 2018 American Chemical Society.

When the interaction between the photo-excited state of a catalyst and a reaction partner is in the form of a single electron transfer, the process is now specified as photoredox catalysis. Since the absorption of light generates an excited electron-hole pair, photoredox catalysts can do oxidation *and* reduction chemistry. Challenging reactivity can be accessed by tuning the redox potentials of the catalyst. The most common photoredox catalysts can be grouped into three classes of materials – organic dyes, transition metal complexes, and semiconductors. Work pioneered by Macmillan, Knowles, and Yoon, to name a few, has led to rapid advancement of transition metal complexes as photoredox catalysts for organic synthesis.[3] The most commonly used polypyridyl complexes of ruthenium (II) or iridium (III) absorb visible light to generate a singlet excited state that rapidly undergoes intersystem crossing to the triplet excited state. The triplet state is long-lived, up to microseconds, allowing more efficient electron transfer with substrates to generate high-energy radical intermediates.

1.2 QDs and Hydrogen Evolution Reaction

This work has paved the way for the development of quantum dots (QDs) as photoredox catalysts. QDs are semiconductor nanoparticles that are quantum-confined in three dimensions, leading to discrete energy levels near the band edges. The general processes involved in charge transfer are similar to transition metal complexes. The QD undergoes light absorption, charge separation to generate the QD excited state, followed by charge transfer. Sometimes, sacrificial quenchers may be used for charge balancing purposes, or sometimes a redox neutral reaction can be catalysed. When a QD is photoexcited, there are a number of possible relaxation pathways – 1) intraband relaxation (Auger recombination, exciton-phonon coupling, ligand vibronic coupling), 2) carrier trapping, and 3) electron-hole recombination (Figure 1.2).[4] Radiative and non-radiative

recombination pathways directly compete with charge transfer. QDs boast several properties that make them good photoredox catalysts – 1) highly tuneable band edge potentials allowing for difficult reactivity, 2) high extinction coefficients allowing low catalyst loading, and 3) broad absorption profiles, allowing catalysis that spans visible to infrared light.[5]

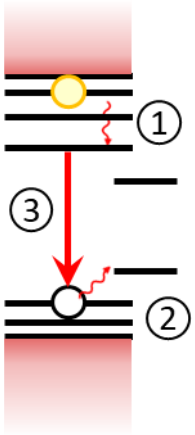

Figure 1.2. Diagram of relaxation pathways for a photo-excited QD – 1) intraband relaxation, 2) carrier trapping, 3) electron-hole recombination.

One of the most studied reactions using QDs as photoredox catalysts is the hydrogen evolution reaction (HER), involving the 2-electron 2-proton reaction to form hydrogen gas. QDs are commonly used as a photosensitiser to transfer electrons to molecular co-catalysts made of earth-abundant transition metals that perform the proton reduction instead (Figure 1.3).[6,7] A sacrificial hole quencher is used to maintain charge balance. More complex architectures such as CdS nanorods tipped with platinum or other metals have shown efficient charge separation with electrons migrating to the metal tip.[8,9] The tip acts as an electron sink and the active site for HER. Ligand shell engineering has been shown to improve activity when QDs are ligated with hole-quenching ligands, as this is commonly accepted as the rate-limiting step for HER.[10,11]

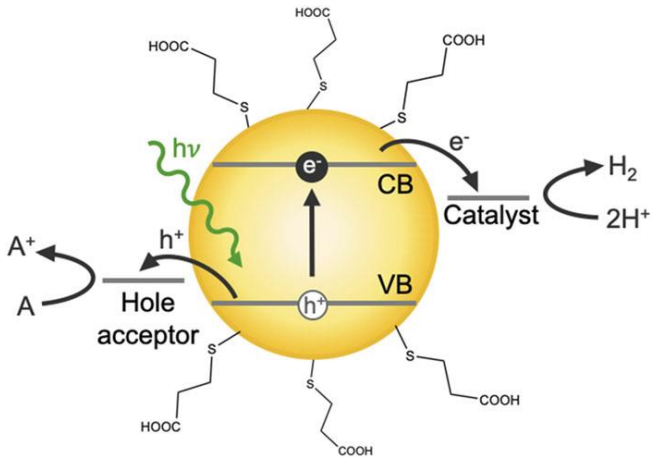

Figure 1.3. Schematic of photocatalytic proton reduction with a QD, illustrating relevant photoinduced charge transfer processes necessary to the photocatalytic process: electron transfer (ET) to the catalyst and hole transfer to a molecular acceptor (A), to maintain charge balance in the system following ET. Ligands typically coat the surface of the QD to maintain colloidal stability, with a common ligand, mercaptopropionic acid, shown here. Reprinted from reference [12], with the permission of AIP Publishing.

1.3 QDs and Organic Photoredox Catalysis

Beyond HER, QDs are gaining momentum as homogeneous photoredox catalysts for more complex organic reactions (Figure 1.4). The field began with ZnS QD-catalysed reactions,[13,14] then progressed to CdS as a more visible light-absorbing catalyst that still maintained very reducing and oxidising band edges.[15,16] The field really took off in the mid-2010s when Weiss and Weix almost simultaneously demonstrated that cadmium chalcogenide QDs were capable of driving carbon-carbon coupling reactions.[17,18] Since then, QDs have also been shown to catalyse alcohol oxidation,[19,20] dehalogenation,[21,22] lignin depolymerisation,[23,24] nitro reduction,[25,26] transfer hydrogenation,[27] and various polymerisation reactions.[28,29] There have also been examples using more benign and lower energy-absorbing InP/ZnS[30] and $CuInS_2$,[31] as well as nanorods as catalysts.[32,33]

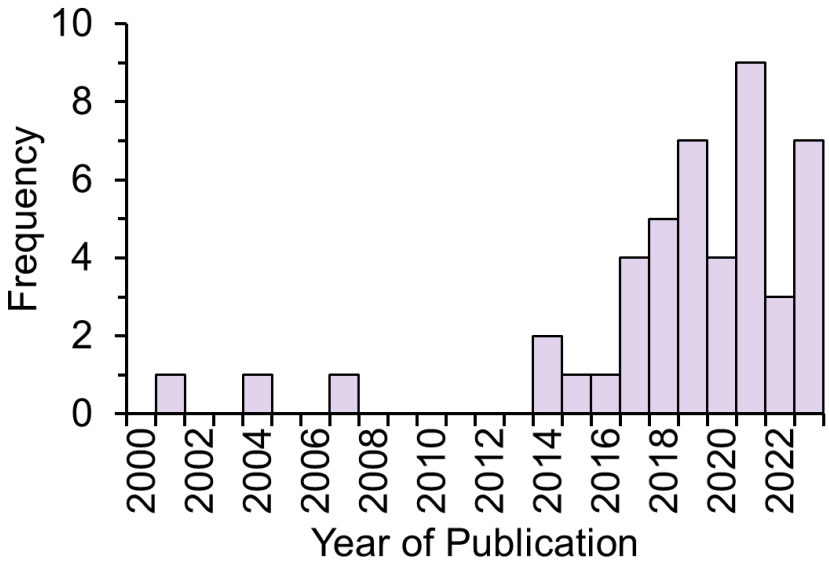

Figure 1.4. Number of publications about QD photoredox catalysis for organic synthesis since 2000.

Compared to HER, much less is understood about what makes a good catalyst, what are the mechanisms for charge transfer, and what is happening to the catalyst for QD organic photoredox catalysis. There are many similar concepts to HER, but organic reactions are far more complex, with bulkier reagents, more complicated reaction mechanisms, and consequently more unwanted side products. We can also gain information from spectroscopic studies of QDs with molecular acceptors, but often effects may be specific to the reaction being catalysed. Nevertheless, there are some strategies for improving QD catalysts that are generally well accepted. For instance, several studies indicate that the sterics of the ligand shell are important for substrate access to the QD surface for charge transfer.[18,24,34] Heterostructures such as core/shells and dot-in-rods have also begun to be used because they have longer excited state lifetimes due to good charge separation of electrons and holes.[32,35]

1.4 This Work

In this dissertation, we catalyse a model reaction with the goal of understanding catalyst evolution and elucidating a mechanism for reactions occurring to the surface of a quantum dot with implications for stability. We also utilise a model reaction to improve the activity and stability of a QD catalyst via a charge-shuttling ligand shell. We employ infrared (IR) spectroscopy to show that the ligand shell is more labile than previously thought, which has implications for catalysis. Finally, we design complex anisotropic heterostructures, probe their intrinsic optoelectronic properties and compare charge transfer between two different morphologies.

1.5 References

(1) Yang, X.; Wang, D. Photocatalysis: From Fundamental Principles to Materials and Applications. *ACS Appl. Energy Mater.* **2018**, *1* (12), 6657–6693. https://doi.org/10.1021/acsaem.8b01345.

(2) Gust, D.; Moore, T. A.; Moore, A. L. Solar Fuels via Artificial Photosynthesis. *Acc. Chem. Res.* **2009**, *42* (12), 1890–1898. https://doi.org/10.1021/ar900209b.

(3) Shaw, M. H.; Twilton, J.; MacMillan, D. W. C. Photoredox Catalysis in Organic Chemistry. *J. Org. Chem.* **2016**, *81* (16), 6898–6926. https://doi.org/10.1021/acs.joc.6b01449.

(4) Kambhampati, P. Unraveling the Structure and Dynamics of Excitons in Semiconductor Quantum Dots. *Acc. Chem. Res.* **2011**, *44* (1), 1–13. https://doi.org/10.1021/ar1000428.

(5) Baek, W.; Chang, H.; Bootharaju, M. S.; Kim, J. H.; Park, S.; Hyeon, T. Recent Advances and Prospects in Colloidal Nanomaterials. *JACS Au* **2021**, *1* (11), 1849–1859. https://doi.org/10.1021/jacsau.1c00339.

(6) Han, Z.; Qiu, F.; Eisenberg, R.; Holland, P. L.; Krauss, T. D. Robust Photogeneration of H2 in Water Using Semiconductor Nanocrystals and a Nickel Catalyst. *Science* **2012**, *338* (6112), 1321–1324. https://doi.org/10.1126/science.1227775.

(7) Huang, J.; Mulfort, K. L.; Du, P.; Chen, L. X. Photodriven Charge Separation Dynamics in CdSe/ZnS Core/Shell Quantum Dot/Cobaloxime Hybrid for Efficient Hydrogen Production. *J. Am. Chem. Soc.* **2012**, *134* (40), 16472–16475. https://doi.org/10.1021/ja3062584.

(8) Wolff, C. M.; Frischmann, P. D.; Schulze, M.; Bohn, B. J.; Wein, R.; Livadas, P.; Carlson, M. T.; Jäckel, F.; Feldmann, J.; Würthner, F.; Stolarczyk, J. K. All-in-One Visible-Light-Driven Water Splitting by Combining Nanoparticulate and Molecular Co-Catalysts on CdS Nanorods. *Nat Energy* **2018**, *3* (10), 862–869. https://doi.org/10.1038/s41560-018-0229-6.

(9) Acharya, K. P.; Khnayzer, R. S.; O'Connor, T.; Diederich, G.; Kirsanova, M.; Klinkova, A.; Roth, D.; Kinder, E.; Imboden, M.; Zamkov, M. The Role of Hole Localization in Sacrificial Hydrogen Production by Semiconductor–Metal Heterostructured Nanocrystals. *Nano Lett.* **2011**, *11* (7), 2919–2926. https://doi.org/10.1021/nl201388c.

(10) Yu, S.; Fan, X.-B.; Wang, X.; Li, J.; Zhang, Q.; Xia, A.; Wei, S.; Wu, L.-Z.; Zhou, Y.; Patzke, G. R. Efficient Photocatalytic Hydrogen Evolution with Ligand Engineered All-Inorganic InP and InP/ZnS Colloidal Quantum Dots. *Nat Commun* **2018**, *9* (1), 4009. https://doi.org/10.1038/s41467-018-06294-y.

(11) Li, X.-B.; Liu, B.; Wen, M.; Gao, Y.-J.; Wu, H.-L.; Huang, M.-Y.; Li, Z.-J.; Chen, B.; Tung, C.-H.; Wu, L.-Z. Hole-Accepting-Ligand-Modified CdSe QDs for Dramatic Enhancement of Photocatalytic and Photoelectrochemical Hydrogen Evolution by Solar Energy. *Advanced Science* **2016**, *3* (4), 1500282. https://doi.org/10.1002/advs.201500282.

(12) Burke, R.; Bren, K. L.; Krauss, T. D. Semiconductor Nanocrystal Photocatalysis for the Production of Solar Fuels. *J. Chem. Phys.* **2021**, *154* (3), 030901. https://doi.org/10.1063/5.0032172.

(13) Yanagida, S.; Azuma, T.; Midori, Y.; Pac, C.; Sakurai, H. Semiconductor Photocatalysis. Part 4. Hydrogen Evolution and Photoredox Reactions of Cyclic Ethers Catalysed by Zinc Sulphide. *J. Chem. Soc., Perkin Trans. 2* **1985**, No. 9, 1487–1493. https://doi.org/10.1039/P29850001487.

(14) Yanagida, S.; Kizumoto, H.; Ishimaru, Y.; Pac, C.; Sakurai, H. Zinc Sulfide-Catalyzed Photochemical Conversion of Primary Amines to Secondary Amines. *Chem. Lett.* **1985**, *14* (1), 141–144. https://doi.org/10.1246/cl.1985.141.

(15) Yin, H.; Wada, Y.; Kitamura, T.; Yanagida, S. Photoreductive Dehalogenation of Halogenated Benzene Derivatives Using ZnS or CdS Nanocrystallites as Photocatalysts. *Environ. Sci. Technol.* **2001**, *35* (1), 227–231. https://doi.org/10.1021/es001114d.

(16) Warrier, M.; Lo, M. K. F.; Monbouquette, H.; Garcia-Garibay, M. A. Photocatalytic Reduction of Aromatic Azides to Amines Using CdS and CdSe Nanoparticles. *Photochem. Photobiol. Sci.* **2004**, *3* (9), 859–863. https://doi.org/10.1039/B404268A.

(17) Caputo, J. A.; Frenette, L. C.; Zhao, N.; Sowers, K. L.; Krauss, T. D.; Weix, D. J. General and Efficient C–C Bond Forming Photoredox Catalysis with Semiconductor Quantum Dots. *J. Am. Chem. Soc.* **2017**, *139* (12), 4250–4253. https://doi.org/10.1021/jacs.6b13379.

(18) Zhang, Z.; Edme, K.; Lian, S.; Weiss, E. A. Enhancing the Rate of Quantum-Dot-Photocatalyzed Carbon–Carbon Coupling by Tuning the Composition of the Dot's Ligand Shell. *J. Am. Chem. Soc.* **2017**, *139* (12), 4246–4249. https://doi.org/10.1021/jacs.6b13220.

(19) Zhao, L.-M.; Meng, Q.-Y.; Fan, X.-B.; Ye, C.; Li, X.-B.; Chen, B.; Ramamurthy, V.; Tung, C.-H.; Wu, L.-Z. Photocatalysis with Quantum Dots and Visible Light: Selective and Efficient Oxidation of Alcohols to Carbonyl Compounds through a Radical Relay Process in Water. *Angewandte Chemie International Edition* **2017**, *56* (11), 3020–3024. https://doi.org/10.1002/anie.201700243.

(20) McClelland, K. P.; Weiss, E. A. Selective Photocatalytic Oxidation of Benzyl Alcohol to Benzaldehyde or C–C Coupled Products by Visible-Light-Absorbing Quantum Dots. *ACS Appl. Energy Mater.* **2019**, *2* (1), 92–96. https://doi.org/10.1021/acsaem.8b01652.

(21) Pal, A.; Ghosh, I.; Sapra, S.; König, B. Quantum Dots in Visible-Light Photoredox Catalysis: Reductive Dehalogenations and C–H Arylation Reactions Using Aryl Bromides. *Chem. Mater.* **2017**, *29* (12), 5225–5231. https://doi.org/10.1021/acs.chemmater.7b01109.

(22) Hu, J.; Pu, T.-J.; Xu, Z.-W.; Xu, W.-Y.; Feng, Y.-S. Cadmium Sulfide Quantum-Dot-Photocatalyzed Cascade Cyclization of Functionalized Difluoromethyl Chlorides with Unactivated Olefins. *Advanced Synthesis & Catalysis* **2019**, *361* (4), 708–713. https://doi.org/10.1002/adsc.201801246.

(23) Enright, M. J.; Gilbert-Bass, K.; Sarsito, H.; Cossairt, B. M. Photolytic C–O Bond Cleavage with Quantum Dots. *Chem. Mater.* **2019**, *31* (7), 2677–2682. https://doi.org/10.1021/acs.chemmater.9b00943.

(24) Wu, X.; Xie, S.; Liu, C.; Zhou, C.; Lin, J.; Kang, J.; Zhang, Q.; Wang, Z.; Wang, Y. Ligand-Controlled Photocatalysis of CdS Quantum Dots for Lignin Valorization under Visible Light. *ACS Catal.* **2019**, *9* (9), 8443–8451. https://doi.org/10.1021/acscatal.9b02171.

(25) Eskandari, P.; Kazemi, F.; Zand, Z. Photocatalytic Reduction of Aromatic Nitro Compounds Using CdS Nanostructure under Blue LED Irradiation. *Journal of Photochemistry and Photobiology A: Chemistry* **2014**, *274*, 7–12. https://doi.org/10.1016/j.jphotochem.2013.09.011.

(26) Jensen, S. C.; Bettis Homan, S.; Weiss, E. A. Photocatalytic Conversion of Nitrobenzene to Aniline through Sequential Proton-Coupled One-Electron Transfers from a Cadmium Sulfide Quantum Dot. *J. Am. Chem. Soc.* **2016**, *138* (5), 1591–1600. https://doi.org/10.1021/jacs.5b11353.

(27) Xi, Z.-W.; Yang, L.; Wang, D.-Y.; Pu, C.-D.; Shen, Y.-M.; Wu, C.-D.; Peng, X.-G. Visible-Light Photocatalytic Synthesis of Amines from Imines via Transfer Hydrogenation Using Quantum Dots as Catalysts. *J. Org. Chem.* **2018**, *83* (19), 11886–11895. https://doi.org/10.1021/acs.joc.8b01651.

(28) Zhu, Y.; Jin, T.; Lian, T.; Egap, E. Enhancing the Efficiency of Semiconducting Quantum Dot Photocatalyzed Atom Transfer Radical Polymerization by Ligand Shell Engineering. *J. Chem. Phys.* **2021**, *154* (20), 204903. https://doi.org/10.1063/5.0051893.

(29) McClelland, K. P.; Clemons, T. D.; Stupp, S. I.; Weiss, E. A. Semiconductor Quantum Dots Are Efficient and Recyclable Photocatalysts for Aqueous PET-RAFT Polymerization. *ACS Macro Lett.* **2020**, *9* (1), 7–13. https://doi.org/10.1021/acsmacrolett.9b00891.

(30) Chakraborty, I. N.; Roy, S.; Devatha, G.; Rao, A.; Pillai, P. P. InP/ZnS Quantum Dots as Efficient Visible-Light Photocatalysts for Redox and Carbon–Carbon Coupling Reactions. *Chem. Mater.* **2019**, *31* (7), 2258–2262. https://doi.org/10.1021/acs.chemmater.9b00086.

(31) Perez, K. A.; Rogers, C. R.; Weiss, E. A. Quantum Dot-Catalyzed Photoreductive Removal of Sulfonyl-Based Protecting Groups. *Angewandte Chemie* **2020**, *132* (33), 14195–14199. https://doi.org/10.1002/ange.202005074.

(32) Verbitsky, L.; Waiskopf, N.; Magdassi, S.; Banin, U. A Clear Solution: Semiconductor Nanocrystals as Photoinitiators in Solvent Free Polymerization. *Nanoscale* **2019**, *11* (23), 11209–11216. https://doi.org/10.1039/C9NR03086G.

(33) Sha, Y.; Lin, X.-M.; Niklas, J.; Poluektov, O. G.; Diroll, B. T.; Lin, Y.; Wen, J.; Hood, Z. D.; Lei, A.; Shevchenko, E. V. Insights into the Extraction of Photogenerated Holes from CdSe/CdS Nanorods for Oxidative Organic Catalysis. *J. Mater. Chem. A* **2021**, *9* (21), 12690–12699. https://doi.org/10.1039/D1TA01124C.

(34) Dabbous, A.; Colson, E.; Chakravorty, D.; Mouesca, J.-M.; Lombard, C.; Caillat, S.; Ravanat, J.-L.; Dubois, F.; Dénès, F.; Renaud, P.; Maurel, V. Fine Tuning of Quantum Dots Photocatalysts for the Synthesis of Tropane Alkaloid Skeletons**. *Chemistry – A European Journal n/a* (n/a), e202300303. https://doi.org/10.1002/chem.202300303.

(35) Xi, Z.-W.; Yang, L.; Wang, D.-Y.; Feng, C.-W.; Qin, Y.; Shen, Y.-M.; Pu, C.; Peng, X. Visible Light Induced Reduction and Pinacol Coupling of Aldehydes and Ketones Catalyzed by Core/Shell Quantum Dots. *J. Org. Chem.* **2021**, *86* (3), 2474–2488. https://doi.org/10.1021/acs.joc.0c02627.

Chapter 2. Is Quantum Dot Photocatalysis Really Homogeneous?

2.1 INTRODUCTION

Cadmium chalcogenide quantum dots have been the material of choice for visible light photoredox catalysis largely due to their wide band gaps, tuneable band edge potentials, and high absorptivity, making them suitable for both reduction and oxidation reactions.[1] CdSe and CdS have bulk band gaps of 1.7 eV and 2.4 eV respectively and may both be tuned across the visible spectrum. However, CdS is the preferred photocatalyst when trying to access more difficult reactivity or higher turnover frequency due to its greater driving force for charge transfer. In addition, CdS nanocrystals of both dot and rod morphologies have been demonstrated as viable catalysts of several organic reactions.[2,3]

However, CdS catalysts are susceptible to photo-degradation, which significantly hinders catalytic activity and the practical implementation of this system at scale. The photocorrosion of CdS catalysts in aqueous conditions has been well documented.[4,5] It is thought that there are two main pathways of irreversible photo-oxidation – 1) accumulation of excess holes leading to elemental sulphur formation and leached cadmium ions (equation 2), and 2) the reactivity of surface sulphides with molecular water or oxygen to form sulphates (equation 3).[4] Strategies to alleviate this decomposition focus on rapidly extracting photogenerated holes to prevent their reactivity with S^{2-} in the lattice, such as constructing heterojunctions with metal oxides or metal catalysts.[6] These strategies have been shown to not only confer stability but also enhance activity.

$$CdS + hv \rightarrow e^- + h^+ \text{ (eq. 1)}$$

$$CdS + 2H_2O \rightarrow Cd^{2+}(aq) + S + H_2 + 2OH^- \text{ (eq. 2)}$$

$$CdS + 2O_2 \rightarrow Cd^{2+} + SO_4^{2-} \text{ (eq. 3)}$$

In non-aqueous colloidal systems, photocorrosion has also been observed, however the phenomenon is less understood and studied. Changes in QD colour and evidence of aggregation have been observed that appear to be alleviated by the addition of excess capping ligand.[7] Increases in QD absorbance scattering have also been observed after catalysis or under illumination with common hole quenchers such is N,N-diisopropylethylamine (DIPEA).[2,8] In a study by Bartlett et al, the photo-oxidation of benzylamine by CdS was studied and XPS measurements showed that surface SO_4^{2-} increased under inert conditions.[9] There remains a lack of understanding and characterisation of QD degradation during organic photocatalysis, and likewise a lack of catalyst recyclability studies. The problem is usually alleviated by using a high loading of catalyst, making these systems inefficient and difficult to scale.

In this work, we use a simple dehalogenation model reaction catalysed by CdS QDs to characterise the photo-decomposition product and propose a mechanism of QD degradation during photocatalysis. We find that concurrent with the formation of product, there is ligand etching, leading to loss of colloidal stability, and also cadmium reduction to form metal deposits measurable by XRD. We also see evidence of surface sulphide oxidation to sulphates. We propose that these are QD surface-localized reactions resulting from an imbalance of charge carriers during the constant flux of catalysis. With this new understanding of catalyst speciation, we can design more stable catalysts and gain a more atomistic understanding of QD photocatalysis.

2.2 CdS Degradation During Photocatalysis

We chose a reductive dehalogenation model reaction studied by the König group.[8] The proposed mechanism (Scheme 2.1) is photoexcitation, followed by reductive quenching of the hole by DIPEA to generate a charged, anionic QD. Next, a single electron transfer to the aryl ring of

the substrate 2-bromobenzonitrile occurs with C-X bond cleavage being triggered, forming bromide as a leaving group. Finally, the radical abstracts an H atom from DIPEA or solvent to form the product, benzonitrile.

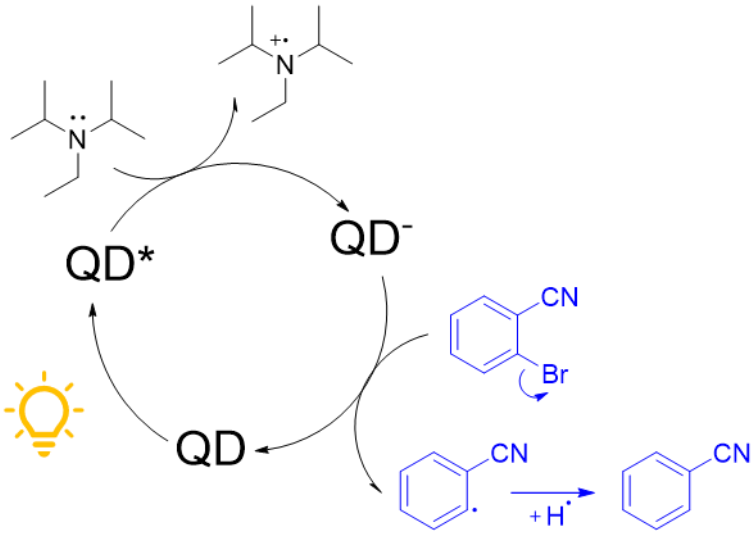

Scheme 2.1. Proposed mechanism of reductive dehalogenation of 2-bromobenzonitrile (blue) by CdS QDs with DIPEA as a sacrificial hole quencher.

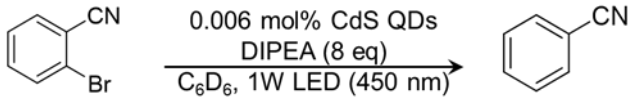

Scheme 2.2 Optimised reaction conditions for photocatalysis.

We first attempted to recreate literature conditions using 5 nm oleate-capped CdS QDs as our catalyst instead of ZnSe/CdS. We observed full conversion of 2-bromobenzonitrile to benzonitrile after 24 hours but found that a large amount of grey-black precipitate accumulated after catalysis (Figure 2.7). We lowered the catalyst loading from the reported number of 0.6 mol % (or 320 nmol) to 0.006 mol % under optimised conditions (Scheme 2.2). At this lower loading, we again observed a large amount of precipitation accompanied by full depletion of the CdS absorbance

during catalysis (Figure 2.1B). We monitored substrate conversion over time by ^{1}H NMR spectroscopy (Figure 2.8) and found that catalysis does not seem to slow down despite precipitation (Figure 2.1A). We report an impressive TOF of 0.67 s^{-1}, however this number becomes less meaningful if the catalyst is evolving over time. We observed no product formation in the absence of light or QD.

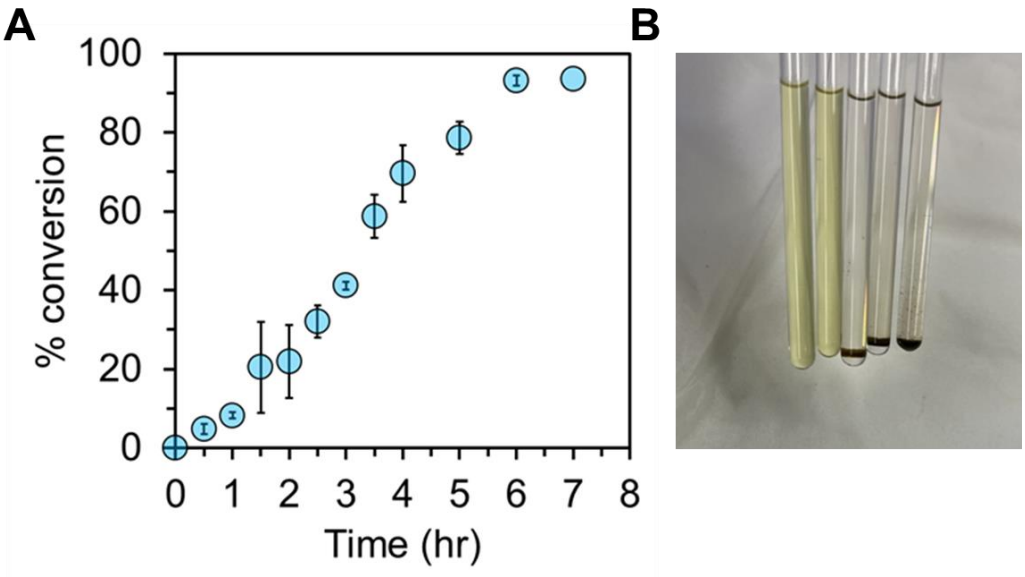

Figure 2.1. Conversion of 2-bromobenzonitrile to benzonitrile over time. (A) Quantification by ^{1}H NMR spectroscopy. (B) Image showing complete depletion of CdS absorbance accompanied by black precipitate formation over time (left to right).

We next analysed the precipitate by powder X-ray diffraction (XRD). From Figure 2.2 (panel A), we can still observe the broad features of zinc blende CdS nanocrystals with sharp features growing in on top of the CdS signal. We can calculate the crystalline domain sizes of CdS using the Scherrer equation and we find that the CdS domains are ~ 3 nm (Table 2.1). It appears that the CdS remains nanocrystalline but may have been etched slightly from their original size of ~ 5 nm. We corroborate this with evidence of ligand etching during catalysis by ^{1}H NMR spectroscopy

(Figure 2.9). The persistence of nanocrystalline CdS is consistent with the observation of continuous product formation. We analysed two later time points (panel B) and clearly observe the formation of crystals of diisopropylammonium bromide (DIPAB). This confirms the mechanism of H atom abstraction from DIPEA to form an iminium ion, followed by hydrolysis to form the ammonium salt.[10] By ^{1}H NMR spectroscopy, we see the ammonium protons as a wide peak at later time points and acetone as a hydrolysis by-product (Figure 2.10).

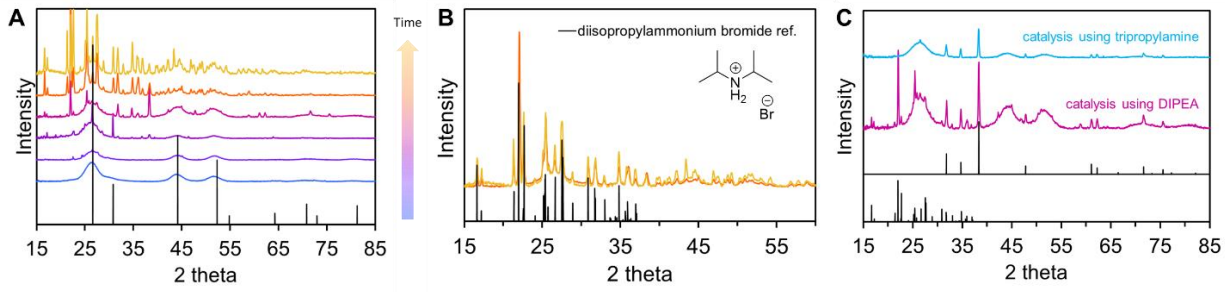

Figure 2.2. XRD patterns of precipitate over the course of the reaction. (A) Precipitate from 0-7 hours. (B) Precipitate showing formation of DIPAB salt. (C) Precipitate showing formation of cadmium metal using DIPEA or tripropylamine as the hole quencher for the reaction.

Lastly, we observe a significant amount of cadmium metal in the precipitate (Panel C). If we use a different quencher tripropylamine, as expected we no longer see the DIPAB salt, but we still observe clear formation of cadmium metal. This tells us that the quencher is not solely responsible for the formation of metallic cadmium. When we image the reaction mixture after catalysis by transmission electron microscopy (TEM), we observe faceted microcrystals that primarily co-localise with cadmium by energy dispersive X-ray spectroscopy (EDS) (Figure 2.3). We therefore hypothesise that the surface passivating layer of $Cd(oleate)_2$ etches off during catalysis and leads to loss of CdS colloidal stability, with either surface cadmium atoms or $Cd(oleate)_2$ being reduced to Cd^0.

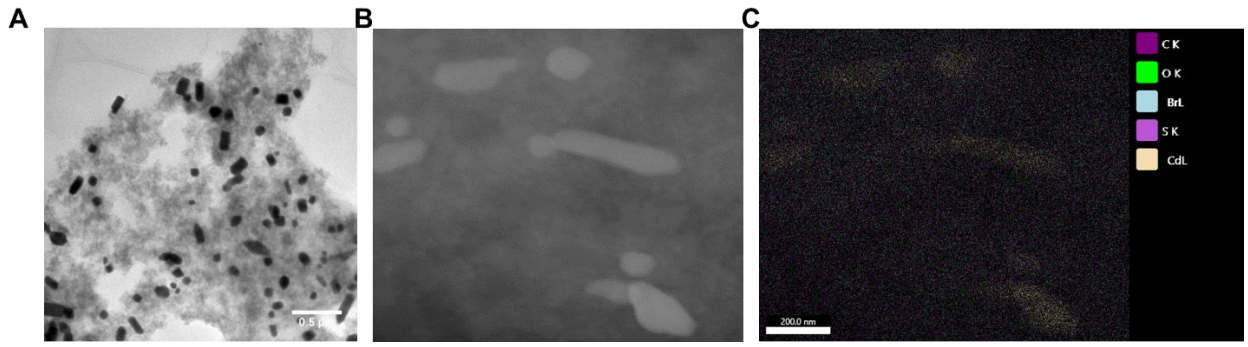

Figure 2.3. TEM images of reaction mixture after catalysis. (A) Bright field image of faceted microcrystals formed during catalysis. (B) STEM image of microcrystals. (C) EDS elemental mapping of microcrystals showing primarily Cd co-localisation.

This mechanism has previously been proposed to occur on the surfaces of QDs that were n-doped by external reductants.[11] The authors doped CdSe QDs with excess electrons using a strong chemical reductant sodium naphthalenide ($Na[C_{10}H_8]$) and saw the dissociation of ligands by NMR and FTIR spectroscopy. They propose that this occurred via reduction of surface Cd^{2+} sites to form Cd^0 deposits with dissociation of the anionic oleate ligands. Evidence of Cd^0 up to this point has been invoked but not experimentally measured, other than by colour change.[12,13] Metal deposits are commonly used as electron sinks for reduction reactions.[14] Therefore, it is possible that as more metallic cadmium is formed, they can rapidly extract electrons and become the active sites for reduction. This can also explain why we never see a decrease in the product formation rate. In fact, looking at the shape of the curve in Figure 2.1, there may be two regimes – 1) catalysis by colloidal CdS (up to ~3 hours) followed by 2) catalysis by Cd^0 and heterogeneous CdS. This finding adds to our atomic level understanding of the processes occurring on QD surfaces during catalysis.

We also observe mild sulphur oxidation by X-ray photoelectron spectroscopy (XPS) of our precipitate after catalysis (Figure 2.4). Since XPS is a surface technique, we hypothesise that these changes are also occurring on the QD surface. Since our experimental setup is under inert

conditions, possible sources of oxidation could be accumulated photo-induced holes, the DIPAB salt by-product, or the oxygen atoms of the ligand binding groups.

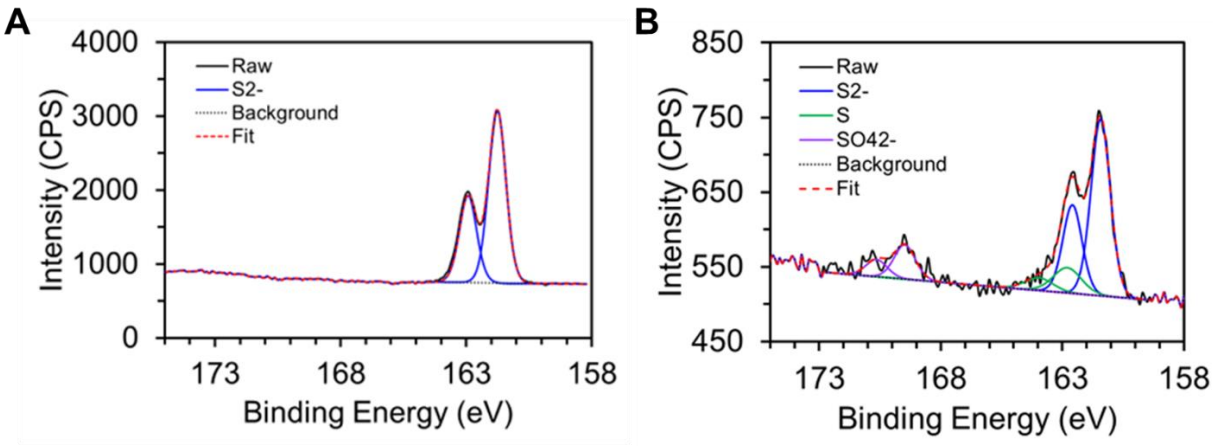

Figure 2.4. Sulphur XPS measurements referenced to carbon. (A) CdS before catalysis and (B) Precipitate after catalysis.

Notably, these degradation phenomena *do not occur* in the absence of product formation. If CdS QDs are illuminated with any singular reagent (DIPEA, ammonium bromide salt, or 2-bromobenzonitrile), there are slight changes in the absorption spectra that are reversible and the QDs remain intact (Figure 2.5). We used tetrabutylammonium bromide (TBABr) as a proxy for bromide salts formed during the reaction. There are slight changes to the second and third optical transitions in the presence of DIPEA and TBABr with a slight increase in scattering (blue and green). This has previously been seen with surface ligand etching.[15] There is also a slight decrease in absorption in the presence of 2-bromobenzonitrile. These results indicate that the reagents themselves could react with the surface of the QDs during catalysis.

When CdS QDs are illuminated in the presence of DIPEA and a classic reversible electron acceptor, methyl viologen MV^{2+}, complete degradation of the QDs is also observed (Figure 2.5).

This tells us that a complete turnover cycle of hole quenching *and* electron extraction is necessary to observe these effects, although this exact degradation product in this case was not characterised.

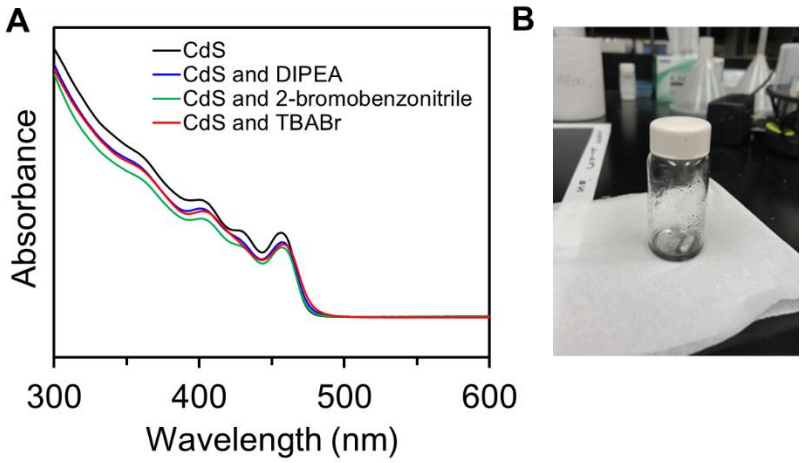

Figure 2.5. Illumination of QDs with reagents. (A) UV-vis absorption of QDs after 2 hours of illumination under catalytic conditions. (B) Image of reaction mixture of QDs, DIPEA and MV^{2+} after 2 hours of illumination.

We propose the degradation that we observe is due to the unbalanced accumulation of charge carriers in the QD during catalysis.[16] Specifically for our system, we see greater evidence for an accumulation of electrons. When CdS is illuminated with DIPEA or 2-bromobenzonitrile alone, the QD becomes doped,[17] but the system reaches an equilibrium and there is likely back electron transfer or Auger recombination with minimal chemical change. However, when both DIPEA and 2-bromobenzonitrile are present and the cycle is complete, the generation of product shifts the equilibrium toward a continuous flux of charges being transferred, leading to charge accumulation and reactivity to the QD surface. It is also possible that reaction by-products such as DIPAB or other transient radical species play a role in interacting with / degrading the QD.

Our results elucidate mechanisms by which CdS QDs evolve during photocatalysis. We primarily see the effects of electron accumulation resulting in ligand etching and cadmium metal

formation. We also see slight photo-oxidation effects as S^{2-} becomes S and SO_4^{2-} at the QD surface. This also highlights that there are many chemical reactions that can occur on the surface of QDs during catalysis, so charge carriers involved in charge transfer are not necessarily always excitonic or band-edge in nature. There is a growing amount of evidence that shows that photo-excited charges localise at surface states before being extracted.[18–20] This is extremely plausible given the poor luminescence of our material, the abundance of trap states, and the fast rates of charge trapping observed in CdS QDs.[21]

We also highlight the need for more rigorous benchmarking of QD catalysts in this field and show that QD photocatalysis is often a "black box" with many side reactions that are not well understood. Given our results, it makes sense that adding in excess ligand to re-passivate the surface can prevent degradation, but a more atom economic method is still desired. In terms of designing better catalysts, a thin shell that does not impede extraction of either electron or hole may be beneficial, but the shell may be subject to the same degradation pathways as a core-only QD. One method of designing QDs that stands out as potentially beneficial for catalysis and stability is the "ligand locking" method reported by several groups.[22,23] If the catalyst can withstand the flux of charge transfer and maintain its structure, then we can achieve a system that is both recyclable and scalable.

2.3 Conclusions

This work demonstrates QD photocatalyst degradation pathways that remain under-reported. We show that a complete catalytic cycle leads to the etching of CdS QD surfaces, loss of colloidal stability, and the formation of micro-crystalline cadmium metal that may serve as active sites for substrate reduction. We also show surface sulphide oxidation to sulphur and sulphates. This work

pushes the community toward a more atomistic understanding of the processes that can occur on the QD surface during photocatalysis and can help us design more stable catalysts that are highly active and scalable.

2.4 EXPERIMENTAL

2.4.1 *Materials*

All experiments, unless otherwise noted, were performed under an inert N_2 atmosphere using a glovebox or standard Schlenk techniques. All glassware was dried in a 160 °C oven overnight prior to use. Oleic acid (90%), anhydrous hexadecane (≥99%), tetramethylthiourea (98%), biphenyl (99.5%), diphenyl ether (98%), anhydrous methanol (99.8%), 2-bromobenzonitrile (99%), N,N-Diisopropylethylamine, tripropylamine (>98%), paraquat dichloride hydrate, were purchased from MilliporeSigma and used as received. Tetrabutylammonium bromide (99+%) was purchased from Fisher Scientific and used as received. Benzene-D6 (D, 99.5%) was purchased from Cambridge Isotope Lab and purified by distillation and stored over activated 4 Å molecular sieves. Toluene (HPLC grade) was purchased from Fisher Scientific, purged with argon, and stored over activated 4 Å molecular sieves. Royal-Blue (448nm) Rebel LEDs were purchased from Luxeon Star LEDs.

2.4.2 *Synthesis of CdS QDs*

The procedure was modified from Hamachi et al.[24] In a 250 mL 3-neck flask, degas cadmium oleate (1.215 g, 1.8 mmol), technical grade oleic acid (1.15 mL, 3.6 mmol) and hexadecane (60 mL) for ~1 hr under vacuum at 90 °C. Meanwhile, dissolve tetramethylthiourea (0.198 g, 1.5 mmol) in biphenyl/diphenyl ether (3 mL). Under N2, raise temperature of reaction flask to 230 °C.

Swiftly inject sulphur precursor solution and monitor reaction by UV-vis absorption spectroscopy. Quench reaction when absorbance profile stops changing by removing the flask from heat. This reaction proceeded for 2.5 hr. To purify the particles, vacuum distill off hexadecane. Re-dissolve particles in toluene and precipitate with methanol for a total of three rounds of purification. Perform one final centrifuge spin in toluene and filter dissolved QDs through 0.45 µm PTFE filter. The QDs were quantified using a sizing curve established by Yu et al.[25] The dots were 4.5 nm with an absorbance maximum at 454 nm, an emission maximum at 470 nm and a broad trap emission feature centred at 720 nm, and low/negligible photoluminescence quantum yield (~2 %) (Figure 2.6). The crystal phase was found to be zinc blende by XRD.

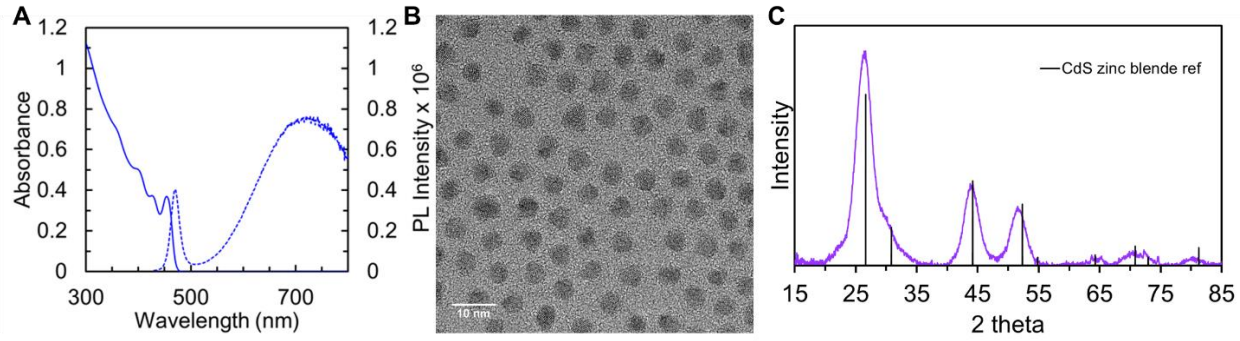

Figure 2.6. Properties of oleate-capped CdS QDs. (A) Absorption and photoluminescence spectra. (B) TEM image. (C) XRD pattern.

2.4.3 *Photocatalysis*

A scintillation vial was prepared with 0.56 nmol of CdS QDs (0.006% loading), 2-bromobenzonitrile (0.00875 mmol, 1.59 mg), 700 uL C_6D_6 and DIPEA (0.07 mmol, 9 mg). The vial was sealed and entirely wrapped with electrical tape and illuminated with a 450 nm LED at 1W (700 mA). The solution was transferred to an NMR tube and quantified by the integral ratio between product and starting material.

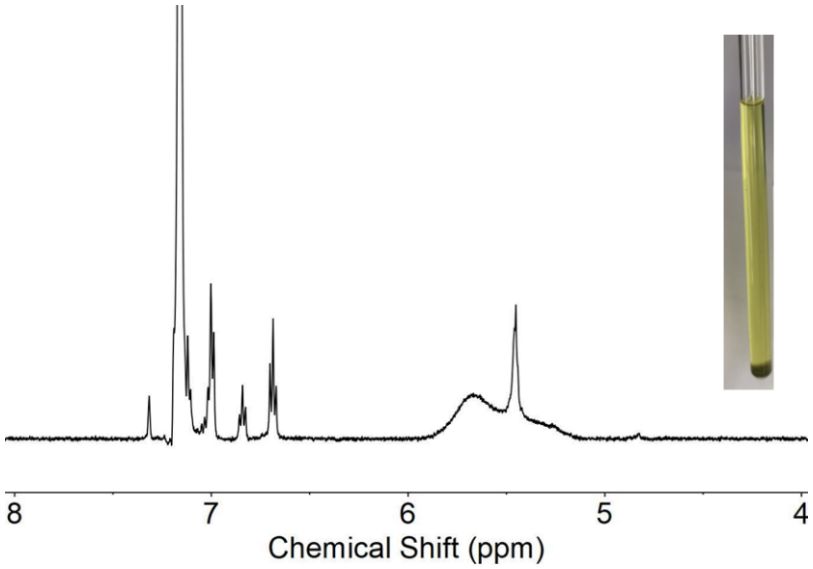

Figure 2.7. ^{1}H NMR of reaction mixture after 24 hours at literature conditions. NMR shows full conversion to product along with oleate signal between 5-6 ppm. Inset shows formation of black precipitate after catalysis. C_6D_6, 500 MHz, d1=10s.

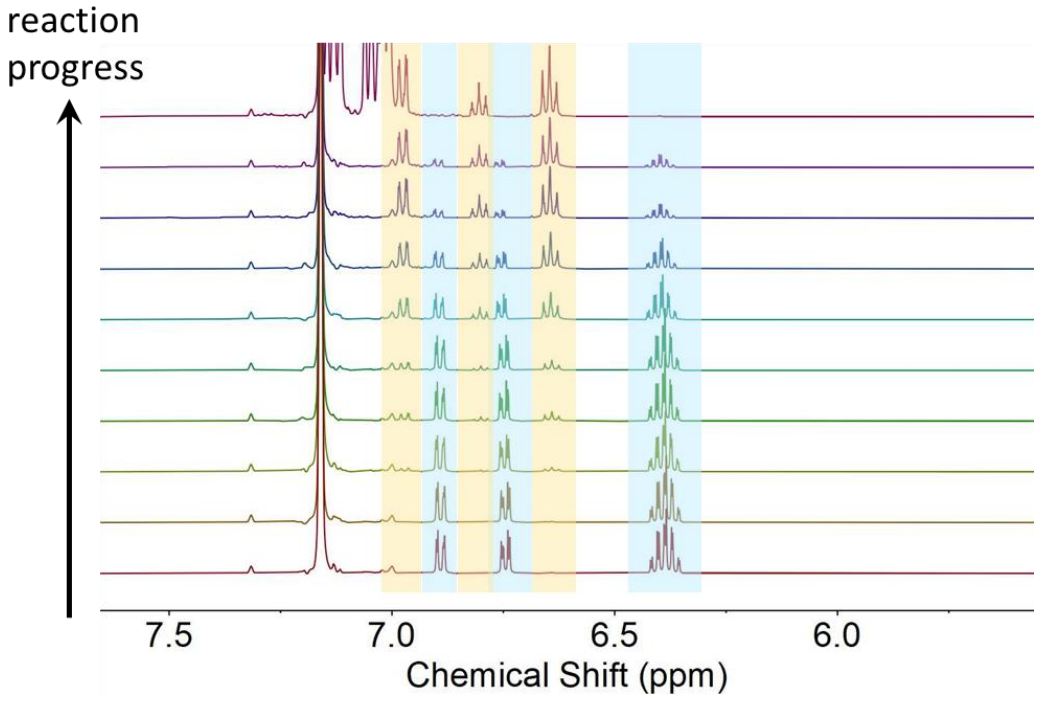

Figure 2.8. ^{1}H NMR of reaction progress at 0.006 mol% loading under optimised conditions showing disappearance of starting material (blue) and growth of product (yellow) over time. C_6D_6, 500 MHz, d1=2s.

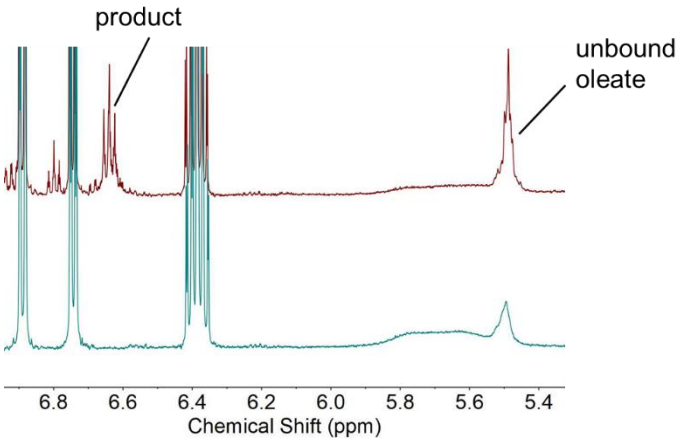

Figure 2.9. ^{1}H NMR before catalysis (blue) and after catalysis (red) showing increase in unbound oleate peak concurrent with the formation of product. C_6D_6, 500 MHz, d1=10s.

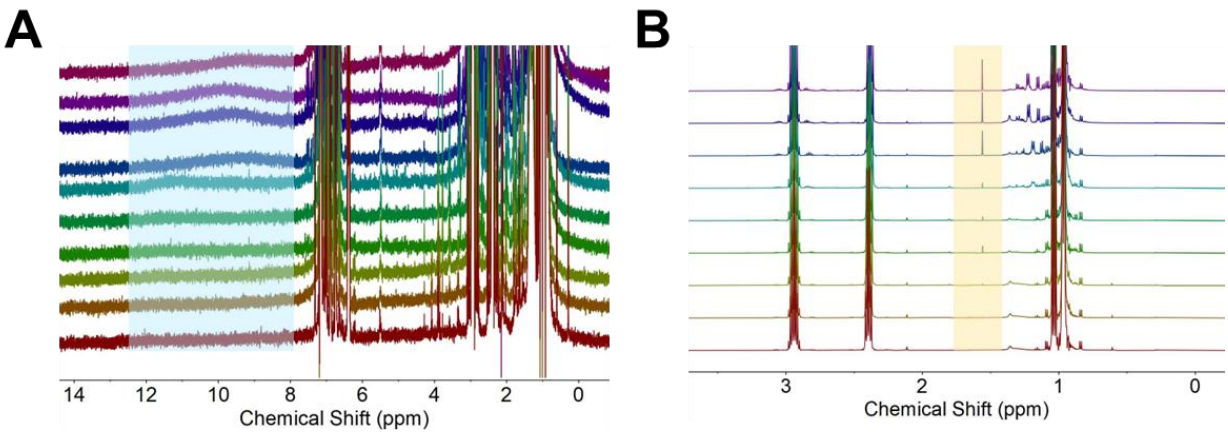

Figure 2.10. ^{1}H NMR over the course of the reaction showing (A) DIPAB ammonium proton (blue) and (B) acetone by-product (yellow). C6D6, 500 MHz, d1=2s.

2.4.4 *XRD and Scherrer analysis*

Crystallite sizes were estimated from powder XRD patterns using Scherrer equation below, where K = 0.94, λ = 1.5406 Å, β = FWHM, θ = Bragg angle, and τ is the mean size of ordered crystalline domains.

$$\tau = \frac{K\lambda}{\beta cos\theta}$$

Table 2.1. Crystallite sizes of CdS over the course of the reaction calculated by XRD Scherrer equation.

Time (hour)	Crystallite size (nm)
0	4.5
1.5	3.4
2	2.9
5	2.9
6	3.1
7	2.7
48 (tripropylamine)	2.1

2.4.5 *Characterisation methods*

UV-Vis spectra were collected on a Cary 5000 spectrophotometer from Agilent. Fluorescence spectra were collected on a Horiba Jobin Yvon FluoroMax4 fluorescence spectrophotometer. ^{1}H NMR spectra were collected on a 500 MHz Bruker Avance spectrometer. TEM images were collected on an FEI Tecnai G2 F20 microscope. Powder XRD diffraction patterns were collected on solid films drop-cast onto a Si wafer by using a Bruker D8 Discover diffractometer. X-ray photoelectron spectroscopy (XPS) was conducted on a Surface Science Instruments S-Probe. The pass energy for high-resolution spectra was 50 eV, with a data point spacing of 0.065 eV. All spectra were calibrated to align carbon peak intensities at 285 eV.

2.5 REFERENCES

(1) Yuan, Y.; Jin, N.; Saghy, P.; Dube, L.; Zhu, H.; Chen, O. Quantum Dot Photocatalysts for Organic Transformations. *J. Phys. Chem. Lett.* **2021**, *12* (30), 7180–7193. https://doi.org/10.1021/acs.jpclett.1c01717.

(2) Widness, J. K.; Enny, D. G.; McFarlane-Connelly, K. S.; Miedenbauer, M. T.; Krauss, T. D.; Weix, D. J. CdS Quantum Dots as Potent Photoreductants for Organic Chemistry Enabled by Auger Processes. *J. Am. Chem. Soc.* **2022**, *144* (27), 12229–12246. https://doi.org/10.1021/jacs.2c03235.

(3) Sha, Y.; Lin, X.-M.; Niklas, J.; Poluektov, O. G.; Diroll, B. T.; Lin, Y.; Wen, J.; Hood, Z. D.; Lei, A.; Shevchenko, E. V. Insights into the Extraction of Photogenerated Holes from CdSe/CdS Nanorods for Oxidative Organic Catalysis. *J. Mater. Chem. A* **2021**, *9* (21), 12690–12699. https://doi.org/10.1039/D1TA01124C.

(4) Weng, B.; Qi, M.-Y.; Han, C.; Tang, Z.-R.; Xu, Y.-J. Photocorrosion Inhibition of Semiconductor-Based Photocatalysts: Basic Principle, Current Development, and Future Perspective. *ACS Catal.* **2019**, *9* (5), 4642–4687. https://doi.org/10.1021/acscatal.9b00313.

(5) Ning, X.; Lu, G. Photocorrosion Inhibition of CdS-Based Catalysts for Photocatalytic Overall Water Splitting. *Nanoscale* **2020**, *12* (3), 1213–1223. https://doi.org/10.1039/C9NR09183A.

(6) Cheng, L.; Xiang, Q.; Liao, Y.; Zhang, H. CdS-Based Photocatalysts. *Energy Environ. Sci.* **2018**, *11* (6), 1362–1391. https://doi.org/10.1039/C7EE03640J.

(7) Caputo, J. A.; Frenette, L. C.; Zhao, N.; Sowers, K. L.; Krauss, T. D.; Weix, D. J. General and Efficient C–C Bond Forming Photoredox Catalysis with Semiconductor Quantum Dots. *J. Am. Chem. Soc.* **2017**, *139* (12), 4250–4253. https://doi.org/10.1021/jacs.6b13379.

(8) Pal, A.; Ghosh, I.; Sapra, S.; König, B. Quantum Dots in Visible-Light Photoredox Catalysis: Reductive Dehalogenations and C–H Arylation Reactions Using Aryl Bromides. *Chem. Mater.* **2017**, *29* (12), 5225–5231. https://doi.org/10.1021/acs.chemmater.7b01109.

(9) DiMeglio, J. L.; Bartlett, B. M. Interplay of Corrosion and Photocatalysis During Nonaqueous Benzylamine Oxidation on Cadmium Sulfide. *Chem. Mater.* **2017**, *29* (17), 7579–7586. https://doi.org/10.1021/acs.chemmater.7b02899.

(10) Yue, W.-J.; Day, C. S.; Brenes Rucinski, A. J.; Martin, R. Catalytic Hydrodifluoroalkylation of Unactivated Olefins. *Org. Lett.* **2022**, *24* (28), 5109–5114. https://doi.org/10.1021/acs.orglett.2c01941.

(11) Hartley, C. L.; Dempsey, J. L. Electron-Promoted X-Type Ligand Displacement at CdSe Quantum Dot Surfaces. *Nano Lett.* **2019**, *19* (2), 1151–1157. https://doi.org/10.1021/acs.nanolett.8b04544.

(12) Zhao, J.; Holmes, M. A.; Osterloh, F. E. Quantum Confinement Controls Photocatalysis: A Free Energy Analysis for Photocatalytic Proton Reduction at CdSe Nanocrystals. *ACS Nano* **2013**, *7* (5), 4316–4325. https://doi.org/10.1021/nn400826h.

(13) McClelland, K. P.; Weiss, E. A. Selective Photocatalytic Oxidation of Benzyl Alcohol to Benzaldehyde or C–C Coupled Products by Visible-Light-Absorbing Quantum Dots. *ACS Appl. Energy Mater.* **2019**, *2* (1), 92–96. https://doi.org/10.1021/acsaem.8b01652.

(14) Wu, K.; Chen, Z.; Lv, H.; Zhu, H.; Hill, C. L.; Lian, T. Hole Removal Rate Limits Photodriven H2 Generation Efficiency in CdS-Pt and CdSe/CdS-Pt Semiconductor Nanorod–Metal Tip Heterostructures. *J. Am. Chem. Soc.* **2014**, *136* (21), 7708–7716. https://doi.org/10.1021/ja5023893.

(15) Anderson, N. C.; Hendricks, M. P.; Choi, J. J.; Owen, J. S. Ligand Exchange and the Stoichiometry of Metal Chalcogenide Nanocrystals: Spectroscopic Observation of Facile Metal-Carboxylate Displacement and Binding. *J. Am. Chem. Soc.* **2013**, *135* (49), 18536–18548. https://doi.org/10.1021/ja4086758.

(16) Wang, J.; Ding, T.; Wu, K. Electron Transfer into Electron-Accumulated Nanocrystals: Mimicking Intermediate Events in Multielectron Photocatalysis II. *J. Am. Chem. Soc.* **2018**, *140* (32), 10117–10120. https://doi.org/10.1021/jacs.8b05942.

(17) Shulenberger, K. E.; Keller, H. R.; Pellows, L. M.; Brown, N. L.; Dukovic, G. Photocharging of Colloidal CdS Nanocrystals. *J. Phys. Chem. C* **2021**. https://doi.org/10.1021/acs.jpcc.1c06491.

(18) Prather, K. V.; Stoffel, J. T.; Tsui, E. Y. Redox Reactions at Colloidal Semiconductor Nanocrystal Surfaces. *Chem. Mater.* **2023**, *35* (9), 3386–3403. https://doi.org/10.1021/acs.chemmater.3c00481.

(19) Wu, K.; Du, Y.; Tang, H.; Chen, Z.; Lian, T. Efficient Extraction of Trapped Holes from Colloidal CdS Nanorods. *J. Am. Chem. Soc.* **2015**, *137* (32), 10224–10230. https://doi.org/10.1021/jacs.5b04564.

(20) Olshansky, J. H.; Balan, A. D.; Ding, T. X.; Fu, X.; Lee, Y. V.; Alivisatos, A. P. Temperature-Dependent Hole Transfer from Photoexcited Quantum Dots to Molecular Species: Evidence for Trap-Mediated Transfer. *ACS Nano* **2017**, *11* (8), 8346–8355. https://doi.org/10.1021/acsnano.7b03580.

(21) Shulenberger, K. E.; Jilek, M. R.; Sherman, S. J.; Hohman, B. T.; Dukovic, G. Electronic Structure and Excited State Dynamics of Cadmium Chalcogenide Nanorods. *Chem. Rev.* **2023**, *123* (7), 3852–3903. https://doi.org/10.1021/acs.chemrev.2c00676.

(22) Loiudice, A.; Segura Lecina, O.; Bornet, A.; Luther, J. M.; Buonsanti, R. Ligand Locking on Quantum Dot Surfaces via a Mild Reactive Surface Treatment. *J. Am. Chem. Soc.* **2021**, *143* (33), 13418–13427. https://doi.org/10.1021/jacs.1c06777.

(23) Wang, D.; Sheridan, M. V.; Shan, B.; Farnum, B. H.; Marquard, S. L.; Sherman, B. D.; Eberhart, M. S.; Nayak, A.; Dares, C. J.; Das, A. K.; Bullock, R. M.; Meyer, T. J. Layer-by-Layer Molecular Assemblies for Dye-Sensitized Photoelectrosynthesis Cells Prepared by Atomic Layer Deposition. *J. Am. Chem. Soc.* **2017**, *139* (41), 14518–14525. https://doi.org/10.1021/jacs.7b07216.

(24) Hamachi, L. S.; Jen-La Plante, I.; Coryell, A. C.; De Roo, J.; Owen, J. S. Kinetic Control over CdS Nanocrystal Nucleation Using a Library of Thiocarbonates, Thiocarbamates, and Thioureas. *Chem. Mater.* **2017**, *29* (20), 8711–8719. https://doi.org/10.1021/acs.chemmater.7b02861.

(25) Yu, W. W.; Qu, L.; Guo, W.; Peng, X. Experimental Determination of the Extinction Coefficient of CdTe, CdSe, and CdS Nanocrystals. *Chem. Mater.* **2003**, *15* (14), 2854–2860. https://doi.org/10.1021/cm034081k.

Chapter 3. Effect of a redox-mediating ligand shell on photocatalysis by CdS quantum dots

Significant portions of the following chapter have previously been published.[1]

3.1 INTRODUCTION

As discussed in Chapter 1, upon photo-excitation, QDs can undergo 1) intraband relaxation, 2) rapid charge carrier trapping, or 3) electron-hole recombination. Radiative and non-radiative recombination directly compete with charge transfer. As-synthesised CdS QDs typically have low photoluminescence quantum yields (PLQY) and a large trap emission feature due to under-passivated surface atoms.[2] With this high density of trap states, holes (< 10 ps) and electrons (< 100 ps) trap rapidly.[3] It is still possible to extract these trapped holes and electrons before they recombine (< 100 ns).[4] In fact, trap-mediated transfer is often observed and can occur on the order of < 5 ns.[5,6] Charge transfer rates have also been found to be proportional to driving force. For both electrons and holes, the Marcus-inverted regime has not been observed. An Auger-assisted mechanism has been proposed to explain this observation.[5,7,8]

The ligand shell may be engineered to improve catalysis. It is known that ligand shell sterics play a large role in charge transfer kinetics – Kuwubata et al showed that with decreasing ligand chain length, the rate of electron transfer to benzoquinone increased, as measured by photoluminescence quenching.[9] The authors rationalised that the ligand shell contained "voids" where acceptors could adsorb onto the particle and decrease the distance to the QD core. A patchier ligand shell with more "voids" or sites for adsorption lead to increased rates of electron transfer.

This has been demonstrated in catalysis where it is generally accepted that shorter ligands can increase the rate of the reaction due to a decreased physical and energetic barrier (tunnelling).[10] In addition, permeable ligand shells that are either comprised of mixed ligands or have lower ligand density have been shown to improve catalysis by facilitating better substrate access to the QD surface.[11,12] However, when approaching the limit of short ligands, a balance must be maintained between transferring charges and maintaining colloidal stability.

The electronic properties of the ligand shell can also be engineered to increase the rate of charge extraction. Hou et al showed that in InP/ZnS QDs, shorter chain thiol ligands better passivate electron traps.[13] With a lower density of trap states, hot electrons in the conduction band are longer lived, and the rate of electron transfer to acceptor molecule anthraquinone was doubled. In HER, it has been extensively shown that using electron-donating (hole-quenching) ligands such as thiols or chalcogenide anions can dramatically increase the rate of hydrogen production[14–16] because hole-quenching is commonly regarded to be the rate-limiting step.[17,18] This concept has yet to be demonstrated in organic systems.

Charge-shuttling ligands could therefore rapidly trap charge carriers, minimise the overlap of electron and hole wavefunctions, extend the excited state lifetime, and increase the probability of charge transfer.[19] We hypothesise that these charge shuttles, which are commonly used in fuel cells and electrocatalysis,[20] could lower the kinetic barrier for charge extraction via two fast steps instead of one slow step. As demonstrated in Chapter 2, if electrons or holes are allowed to accumulate in CdS QDs, the surface can degrade to form Cd^0 and SO_4^{2-}, with ligand etching and loss of colloidal stability. We also hypothesise that QD stability can be improved with redox mediator ligands. Having the catalytic reaction happen at the ligand instead of at the inorganic

surface could prevent the QD degradation. Lastly, since the ligands accept charge reversibly, they would not undergo any chemical change that also causes loss of colloidal stability.

In this work, we ligated the surface of CdS QDs with a series of hole-accepting ligands (ferrocene carboxylic acid derivatives) and electron-accepting ligands (phenazine derivative) and evaluated their effects on photocatalysis and QD stability. We find that the hole-accepting ligands hinder catalysis but are good for stability, except in a low coverage regime where a dynamic ligand shell modestly improves catalysis. We find that trapping the electron on a ligand generates a long-lived, charge separated state that improves the rate of hole transfer and overall rate of reaction.

3.2 Ligand Exchanges on CdS Quantum Dots

3.2.1 *Ferrocene carboxylic acids*

We chose a series of ferrocene carboxylic acid derivatives – 1,1-ferrocenedicarboxylic acid (Fc-$(COOH)_2$), ferrocenecarboxylic acid (Fc-COOH) and ferroceneacetic acid (Fc-CH_2COOH) – to construct a general hole-shuttling ligand shell. Ferrocenes have long been established as effective hole acceptors on photoexcited QDs.[5,21–23] Ferrocenes have also been demonstrated as viable redox mediators or catalysts in various systems due to their clean redox reversibility.[24,25] Even though thiols are commonly used as strongly-binding hole quenchers, we chose not to use thiol derivatives because they can easily undergo irreversible oxidation to form disulphides.

We verified the binding of our Fc ligands using cyclic voltammetry (CV). Our group has previously demonstrated that this technique is a viable tool for calculating equilibrium binding constants of redox-active ligands to QD surfaces.[26] We see from titrating in QDs that all three ligands exchange with native oleate ligands. This is demonstrated by the lower current as more

CdS QDs are added, indicating a decreased diffusion coefficient for Fc as it goes from a freely diffusing molecule to a bound ligand on a much heavier QD (Figure 3.1).

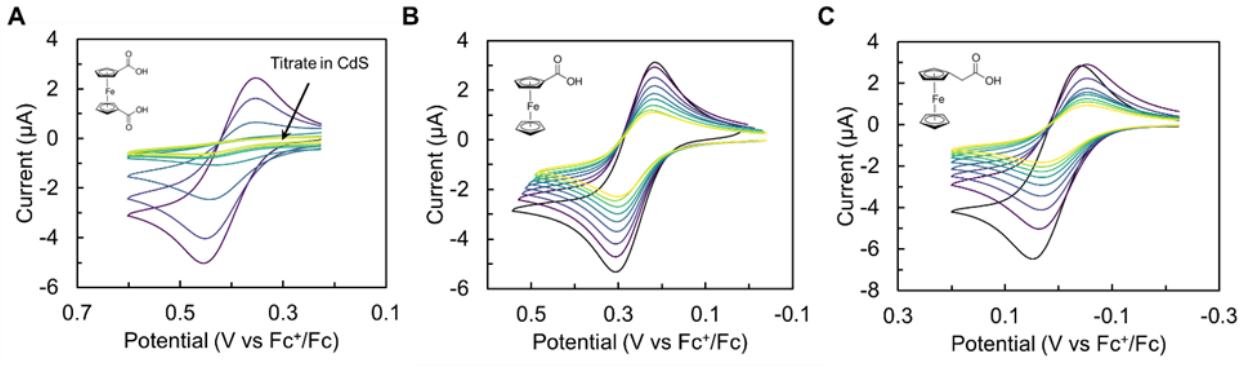

Figure 3.1. CVs of 1 mM (A) Fc-$(COOH)_2$, (B) Fc-COOH, and (C) Fc-CH_2COOH titrated with 0.024 equivalents of CdS QDs (black arrow); 0.15 M [NBu4][PF6], THF, glassy carbon working, Pt auxiliary, and Ag pseudo reference electrodes, 10 mV/s.

We can fit equilibrium binding constants for both the reduced and oxidised forms of Fc and we find that both forms bind to the surface (Table 3.1). This is critical to our hypothesis of redox-mediating ligands conferring stability to QD photocatalysts. We also note that the three ligands have very different binding strengths in the order of Fc-$(COOH)_2$ > Fc-CH_2COOH > Fc-COOH. Intuitively, Fc-$(COOH)_2$ is the strongest binder with two carboxylic acid groups. Lastly, we observe that the redox potentials of the ligands do not change when bound. The redox potentials for Fc-$(COOH)_2$, Fc-COOH and Fc-CH_2COOH are found to be 0.4 V, 0.29 V, and 0 V vs Fc respectively.

Table 3.1. Equilibrium binding constants for reduced and oxidised forms of Fc ligands to CdS.

	Fc-$(COOH)_2$	**Fc-COOH**	**Fc-CH_2COOH**
K_1 (Fc/CdS)	3.99×10^4	3.28×10^2	1.7×10^3
K_2 (Fc^+/CdS)	1.3×10^4	7.94×10^2	1.16×10^3

Since carboxylic acids can bind to the surface in both protonated and deprotonated forms, it could undergo X-type exchange or L-type assisted Z-type exchange.[27,28] This could have implications on the size of the inorganic core of the nanocrystal and therefore the QD's absorptive properties. We exchanged 100 equivalents of Fc ligands onto the surface and saw no changes in the absorption profile of the QDs (Figure 3.2), thus precluding the possibility of an etched surface.

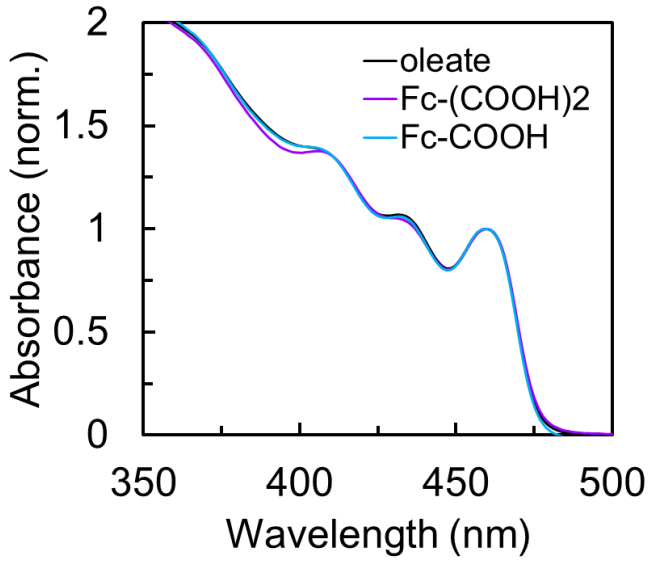

Figure 3.2. Absorbance profiles of CdS QDs exchanged with 100 equivalents of Fc ligand and purified by column chromatography.

3.2.2 *Phenazine-1-carboxylic acid*

We also ligated our QDs with an electron-accepting ligand, phenazine-1-carboxylic acid, to test the effect of an electron-shuttling ligand on catalysis. Phenazine-1-carboxylic acid can undergo two reduction events at -0.88 V and -1.64 V versus ferrocene respectively (Figure 3.3C). We can confirm binding to the surface by ^{1}H NMR spectroscopy by monitoring the evolution of unbound oleate ligands when titrating in increasing amounts of phenazine (Figure 3.3B).

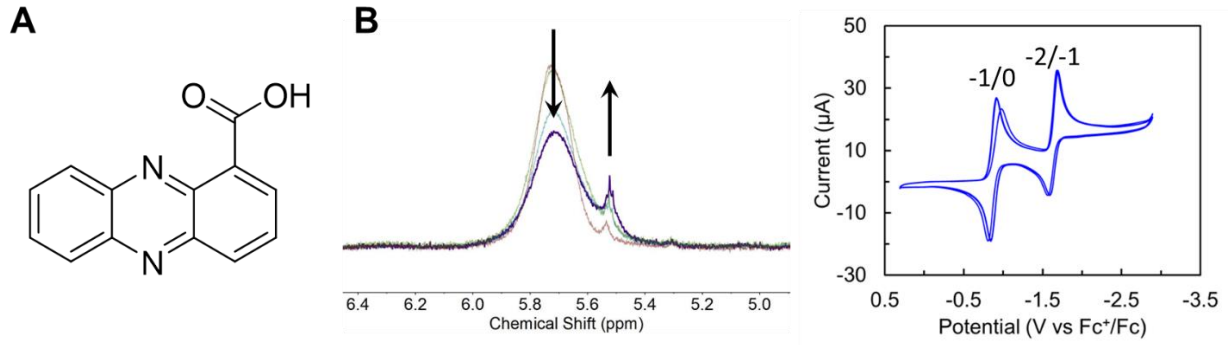

Figure 3.3. (A) Molecular structure of phenazine-1-carboxylic acid. (B) ^{1}H NMR of titration of CdS QDs with increasing amounts of ligand showing decreasing bound oleate and increasing unbound oleate ligands. C6D6, 500 MHz, d1=10s. (C) CV of phenazine-1-carboxylic acid; 0.15 M [NBu_4][PF_6], MeCN, glassy carbon working, Pt auxiliary, and Pt reference electrodes, 100 mV/s.

3.2.3 *2-(3,5-di-tert-butylphenyl)acetic acid*

Since changing the ligands inherently changes the steric profile of the ligand shell, we also used a control of a redox-innocent carboxylic acid ligand – 2-(3,5-di-tert-butylphenyl)acetic acid – to attempt to isolate steric and charge-shuttling effects. We also confirm the binding of this ligand by ^{1}H NMR spectroscopy (Figure 3.4).

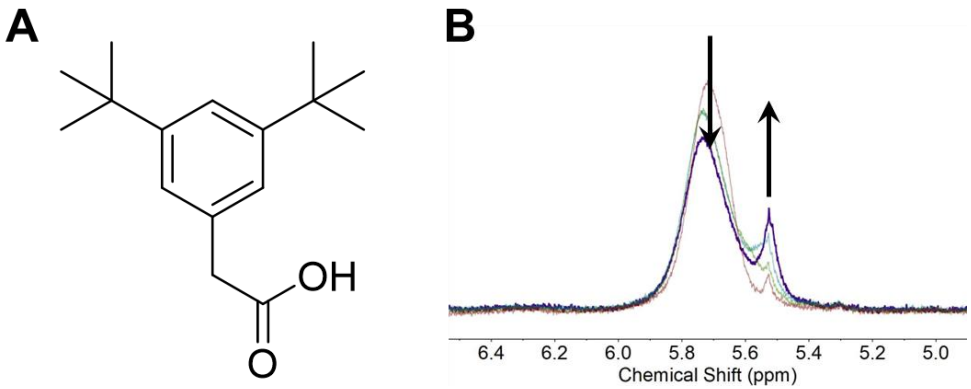

Figure 3.4. (A) Molecular structure of 2-(3,5-di-tert-butylphenyl)acetic acid. (B) ^{1}H NMR of tsitration of CdS QDs with increasing amounts of ligand showing decreasing bound oleate and increasing unbound oleate ligands. C6D6, 500 MHz, d1=10s.

3.3 Catalysis Using Redox-Active and Redox-Innocent Ligands

3.3.1 *Photocatalytic model reaction*

We chose a simple model reaction wherein a photoredox-generated α-amino radical is coupled to a vinyl sulfone to afford an allylic amine. This reaction was first demonstrated by Macmillan et al. using a molecular iridium (III) catalyst.[29] In 2017, the Weiss group showed that 3.7 nm CdS QDs were able to catalyse this reaction, with a more "disordered" ligand shell improving catalysis.[11] In this reaction, the rate-limiting step has been shown by these groups to be hole transfer from catalyst to 1-phenylpyrrolidine (PhPyr). This enables us to elucidate the effect of charge-mediating ligand shells on the rate of hole transfer from QD to substrate and subsequently, catalytic activity. To form the product, the PhPyr radical loses a proton and attacks at the double bond position of phenyl trans-beta-styryl sulfone. This radical adduct then accepts an electron from the QD to regenerate the catalyst and eliminates a phenyl sulfonyl anion to complete the catalytic cycle (Scheme 3.1). Our catalytic conditions were optimised from Weiss et al (Scheme 3.2), and we monitored product formation by ^{1}H NMR spectroscopy. We observed no product formation in the absence of QDs.

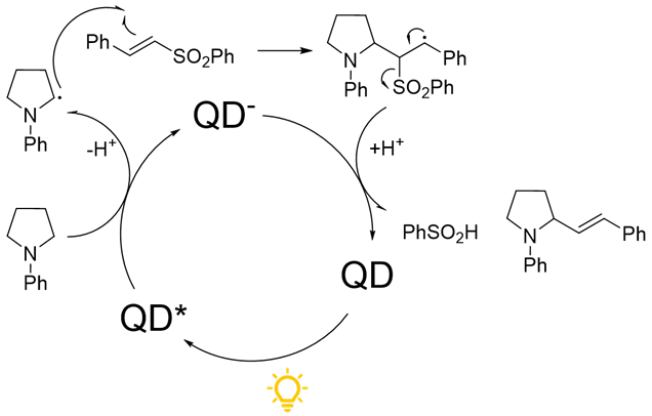

Scheme 3.1. Proposed reaction mechanism for carbon–carbon coupling of 1-phenylpyrrolidine to phenyl trans-beta-styryl sulfone based on reports from Noble and Macmillan[29] and Zhang et al.[11]

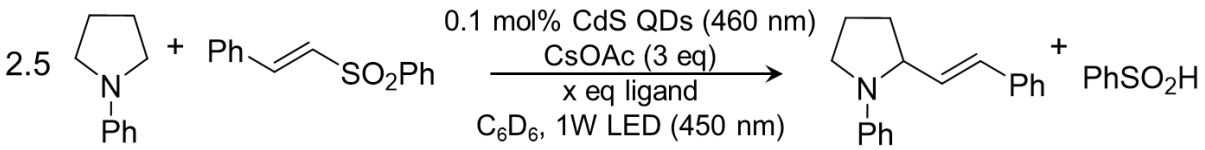

Scheme 3.2. Optimised reaction conditions for this study.

3.3.2 *Effect of redox-innocent ligand exchange on catalysis*

We used 2-(3,5-di-tert-butylphenyl)acetic acid as a control to probe the effect of making changes to the ligand shell without imparting charge-accepting properties. Since the geometries of Fc and phenazine are significantly different from oleic acid, we chose a redox-innocent ligand whose geometry would also significantly perturb the ligand shell. Measuring product formation at the same time point with increasing coverage of 2-(3,5-di-tert-butylphenyl)acetic acid, we found that increased coverage improved catalysis (Figure 3.5).

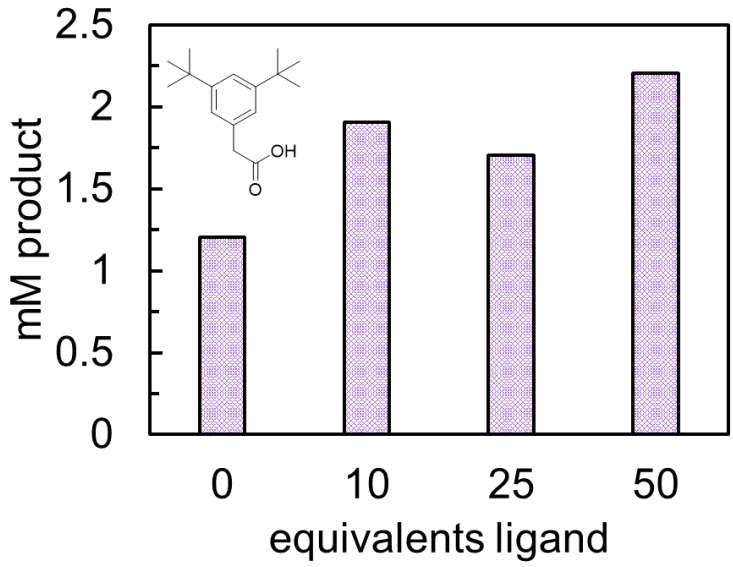

Figure 3.5. Product quantification after 30 minutes under photocatalytic conditions of CdS QDs exchanged with increasing equivalents of 2-(3,5-di-tert-butylphenyl)acetic acid.

3.3.3 *Effect of hole-mediating ligands on catalysis*

We performed ligand exchanges with 10 equivalents of each Fc ligand and monitored the progress of the reaction. We observed the slowest reaction rate with Fc-$(COOH)_2$, and mildly improved catalysis with Fc-COOH and Fc-CH_2COOH compared to native CdS (Figure 3.6A). We also increased the number of Fc's on the surface and measured product formation at 30 minutes. We found that as more Fc's are bound in the cases of Fc-COOH and Fc-CH_2COOH, product formation decreased significantly, whereas with increasing Fc-$(COOH)_2$ coverage, product formation remained roughly constant (Figure 3.6B).

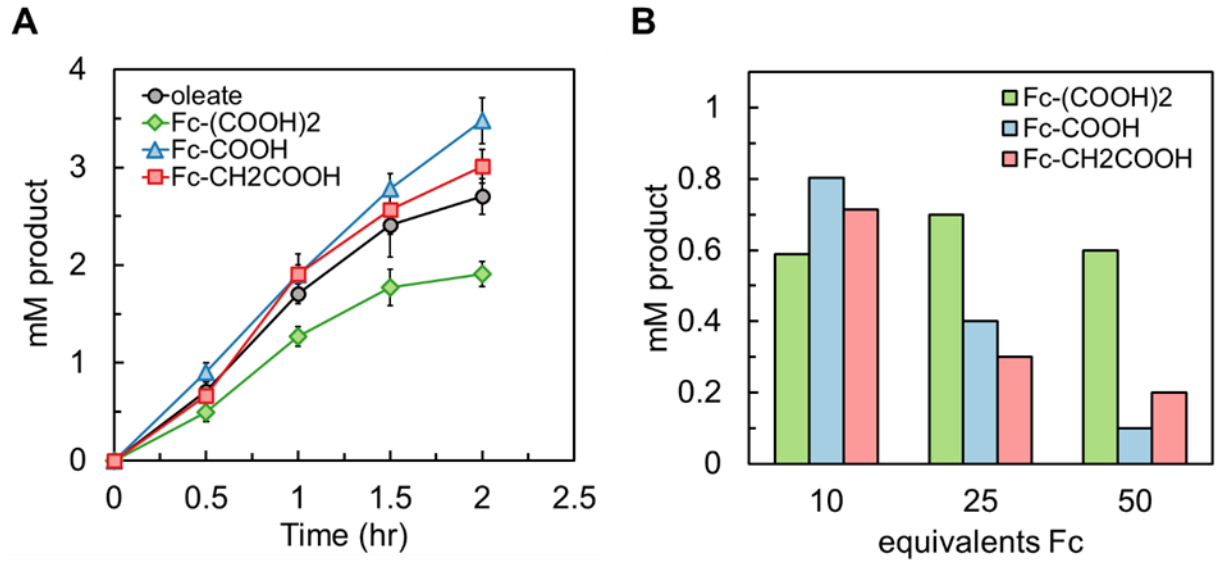

Figure 3.6. Catalytic results as a function of ligand identity and surface coverage. (A) Catalysis results of CdS QDs ligated with ten equivalents of Fc ligands. (B) Catalysis results at 30-min timepoint of CdS QDs ligated with increasing equivalents of Fc ligands.

3.3.4 *Effect of electron-mediating ligands on catalysis*

We also ligated our QDs with an electron-accepting ligand, phenazine-1-carboxylic acid. We observed ~ 4-fold increase in rate of reaction at ten equivalents, with a marginal increase with

increasing phenazine coverage (Figure 3.7). Taking the results of all of our ligands together, we can begin to paint a picture of what factors are affecting catalysis.

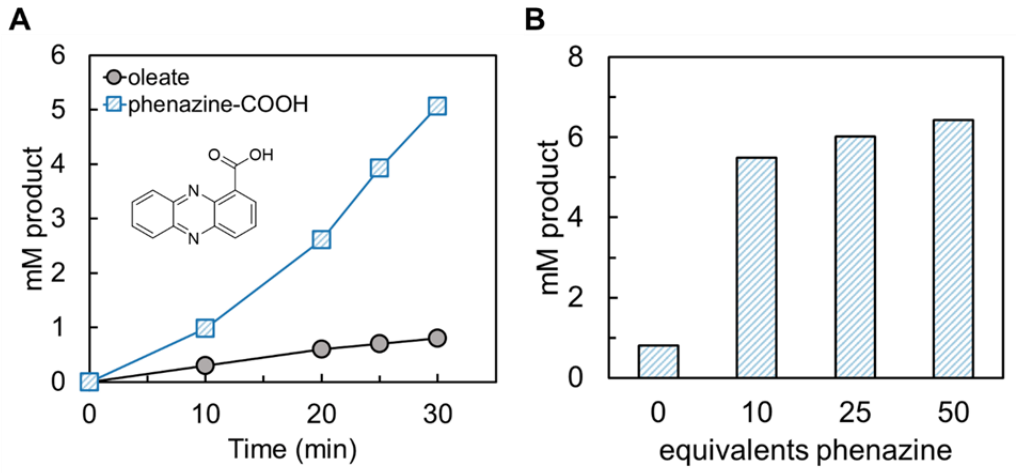

Figure 3.7. Catalytic results using phenazine-1-carboxylic acid (phenazine-COOH) ligand. (A) Catalysis using CdS dots ligated with ten equivalents of phenazine-COOH. (B) Catalysis results at 30-min timepoints of CdS dots ligated with increasing equivalents of phenazine ligand.

3.4 Rationalising Differences in Catalysis

3.4.1 *Ligand steric profiles*

When you consider the geometry of all ligands used in this study, oleic acid is significantly the longest (~ 20 Å). On the other end of the spectrum, a ferrocene molecule bound on its side is about one tenth that length (~ 2 Å). This means that whenever a molecule of oleic acid is displaced, a considerable "valley" forms in the ligand shell where substrates can be buried, decreasing the distance to the inorganic core for charge transfer.[9] This disorder is generally thought to improve catalysis and should be increased for all our ligands. Further, ligand exchange typically occurs on the most reactive facets of the nanocrystal, so a particle's surface is inhomogeneous and some regions could have wider valleys.[30–32]

We see increased activity for 2-(3,5-di-tert-butylphenyl)acetic acid. This tells us that bulky ligands displace more native oleate, creating disorder in the shell. We also see major improvements in catalysis with phenazine-1-carboxylic acid. Since this molecule is a planar aromatic compound, we would expect some stacking in the ligand shell. For this molecule, the large enhancement in catalysis could simply be a result of sterics – it remains to be seen whether the ligand's electron-accepting properties are also at play.

For the ferrocene ligands, we should see the most improvement in catalysis if we only considered the sterics argument, since ferrocenes should create the most disordered ligand shell for substrates to adsorb. However, in the cases of Fc-COOH and Fc-CH_2COOH, we only see a mild improvement at 10 equivalents of coverage, followed by a sharp decrease in activity as coverage goes up to 50 equivalents. For Fc-$(COOH)_2$, the rate of catalysis is slowed at 10 equivalents and remains steady with increasing coverage. This tells us that sterics cannot be the dominant factor for this series of ligands.

3.4.2 *Charge transfer from QD to Fc*

We performed transient absorption spectroscopy (TA) to probe the first charge transfer step of the shuttle from QD to Fc ligand. We collected spectra of CdS, CdS + Fc-$(COOH)_2$, CdS + Fc-COOH and CdS + Fc-CH_2COOH in the fs - μs regime (Figure 3.8). The TA spectra are consistent with other reports of QDs. The spectra are composed of ground state bleach (GSB) signatures and derivative line shapes due to Stark shift. Given the large absorption cross section of CdS compared to the ferrocene derivatives, no signal is observed relating to any molecular radical cation. However, the increased rate of recovery of the GSB is indicative of charge extraction from the QDs.

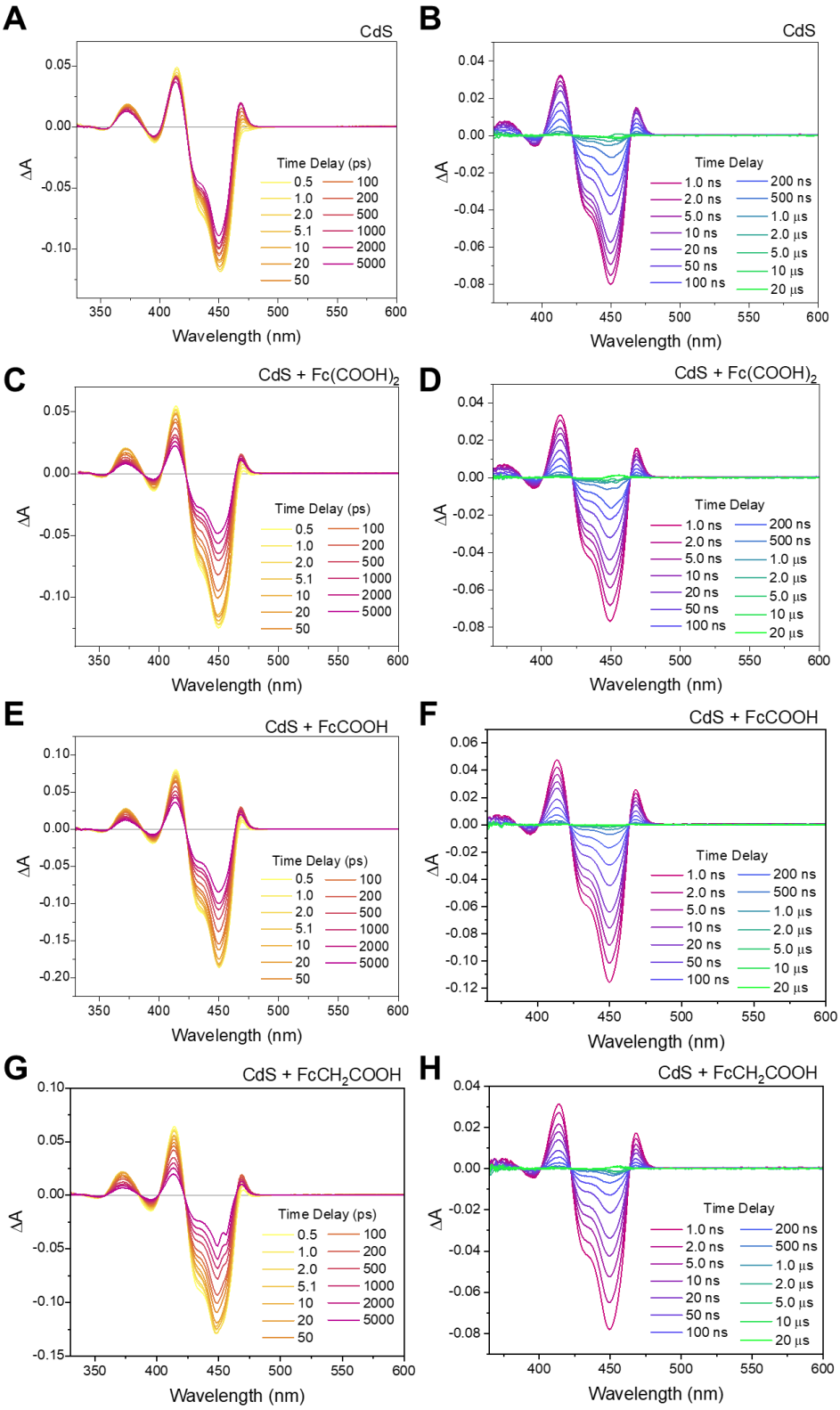

Figure 3.8. TA spectra of (A-B) CdS, (C-D) CdS + Fc-$(COOH)_2$, (E-F) CdS + Fc-COOH, (G-H) CdS + Fc-CH_2COOH in the fs - ns regime (left column) and ns - μs regime (right column).

Table 3.2. Fitted lifetimes from TA spectra.

	t_1 (ps)	t_2 (ps)	t_3 (ns)	t_4 (ns)	t_5 (us)
CdS	3.5 ± 0.1	143 ± 3	22.2 ± 0.6	172 ± 4	2.09 ± 0.08
CdS + Fc-$(COOH)_2$	4.6 ± 0.1	144 ± 2	4.2 ± 0.1	72 ± 1	0.81 ± 0.02
CdS + Fc-COOH	5.5 ± 0.1	211 ± 3	2.9 ± 0.08	53.4 ± 0.9	0.44 ± 0.01
CdS + Fc-CH_2COOH	5.7 ± 0.1	187 ± 3	2.1 ± 0.05	29.3 ± 0.7	0.232 ± 0.006
CdS + PhPyr	5.1 ± 0.2	171 ± 4	59.7 ± 0.2	290 ± 20	4.0 ± 0.6

All TA data was fit using a decay associated model wherein five wavelengths are fit simultaneously (375 nm, 396 nm, 415 nm, 430 nm, 468 nm) to produce decay associated spectra and time constants. The nanoTA data (ns - μs regime) was fit to three exponentials. The femtoTA data (fs - ns regime) were fit using three (or four) exponentials with the longest (or two longest) lifetimes fixed from the nanoTA fits. The need for five exponentials is due to distributed kinetics (e.g. due to particle size inhomogeneity, trap state distribution), which is common throughout QD literature. The first two lifetimes were approximately the same in all samples and we attribute these to intrinsic processes such as intraband relaxation and Auger recombination that occur before charge transfer (Table 3.2). The remaining three lifetimes differed based on the inclusion of Fc ligand, suggesting that charge extraction is occurring. The lifetimes were converted to rates and then a weighted average was calculated using the fitted amplitudes as weighting factors. The lifetimes extracted in the presence of PhPyr did not strongly indicate charge transfer.

In general, the rates extracted for the Fc ligands were on the order of 10^8 s^{-1} (Figure 3.9). This is slower than the hole transfer rate measured by Macdonald et al to a Fe(II)-dithiocarbamate ligand,[33] but faster than those measured by Olshansky et al to a library of ferrocene thiols.[5,23] In our experiments, the rates extracted from TA also increase with more driving force. This is

consistent with prior reports that do not observe the Marcus-inverted regime for hole (or electron) transfer from QDs.[5,34] The TA rates demonstrate that charge is efficiently being transferred from QD to Fc ligand. To the best of our knowledge, carboxylic acid ferrocene derivatives have not been previously established as hole quenchers of QDs and may be advantageous compared to typical Fc-thiols for reasons mentioned previously.

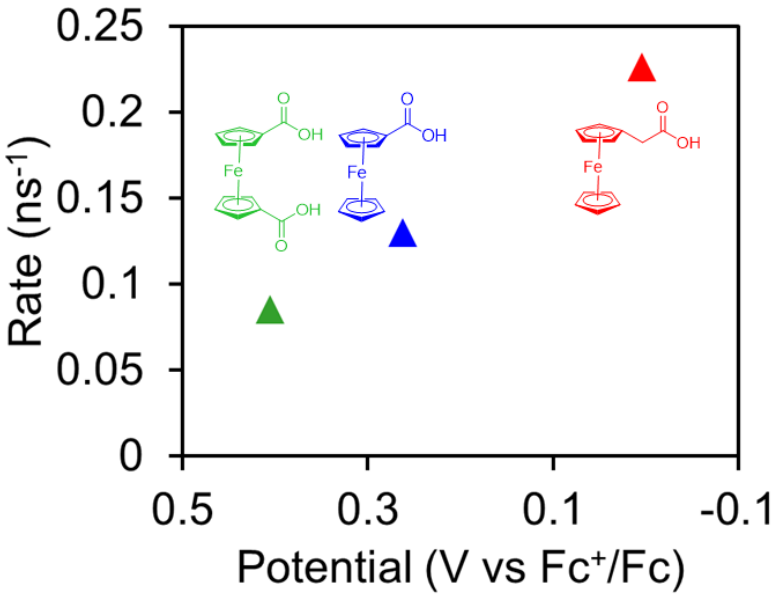

Figure 3.9. Weighted average charge transfer rates of Fc-$(COOH)_2$ (green), Fc-COOH (blue), and Fc-CH_2COOH (red) fit from TA spectra.

We also utilise photoluminescence quenching to measure charge transfer from QD to Fc. We found that both excitonic and trap emission were quenched for all three ligands (Figure 3.21). When Stern-Volmer quenching constants were extracted, we found that the rate constants for all three Fc ligands were on the same order of magnitude (10^5) for both excitonic and trap quenching (Table 3.3), but with opposing trends (Figure 3.10). There was not significant quenching in the presence of PhPyr.

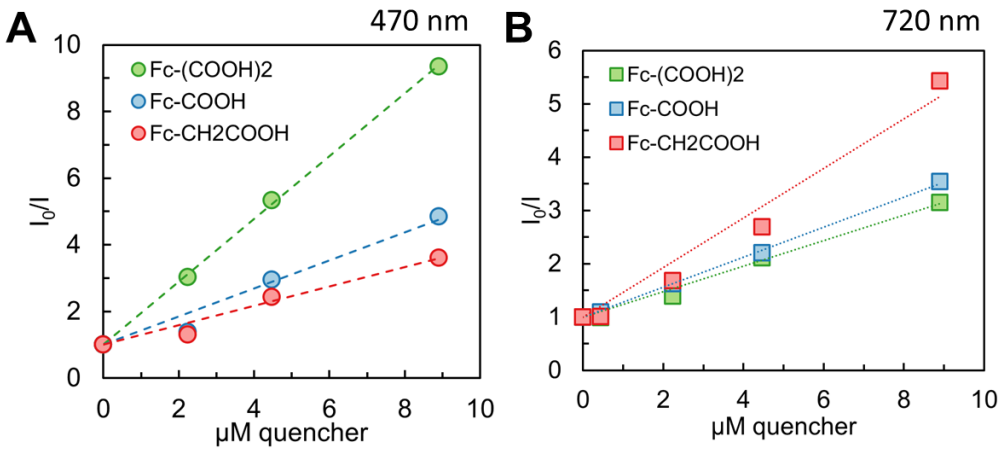

Figure 3.10. Charge transfer from CdS QD to Fc ligands probed via fluorescence quenching. (A) Stern–Volmer plot for quenching of CdS QD fluorescence by successive addition of Fc-$(COOH)_2$ (green), Fc-COOH (blue), and Fc-CH_2COOH (red) (0–20 equivalents relative to CdS) monitored at 470 nm. (b) Stern–Volmer plot for quenching of CdS QD fluorescence monitored at 720 nm.

Table 3.3. Stern-Volmer quenching constants from CdS QDs titrated with Fc ligands and PhPyr.

	V vs Fc^+/Fc	**Log(K_{SV}) at 470 nm**	**Log(K_{SV}) at 720 nm**
Fc-$(COOH)_2$	0.4045	5.97	5.38
Fc-COOH	0.2615	5.90	5.45
Fc-CH_2COOH	0.004	5.73	5.67
PhPyr		3.83	4.11

From the CVs of the Fc ligands, we know that the driving force for hole transfer from QD to Fc increases in the order of Fc-$(COOH)_2$ < Fc-COOH < Fc-CH_2COOH. This is the trend observed for quenching of the trap feature, which has previously been attributed to the recombination of both trapped electrons[2] (to VB hole) and holes[6] (to CB electron). Given the low quantum yield of our material, it is likely that the majority of holes being extracted are trapped holes. Since it is well known that holes trap rapidly onto the surface of CdS,[3] our interpretation is that trapped holes are extracted at rates that increase with more driving force (Figure 3.10B), which is in good agreement with results from other groups mentioned previously.[5] A minority population of valence band holes

are also extracted. The trend is reversed, and we propose that these holes are transferred via a unimolecular process that is more affected by Fc binding strength (Figure 3.10A).[9] We also probed the rate of hole transfer from as-synthesised QDs to the substrate PhPyr. The rates of both band edge and trapped hole transfer to PhPyr were two orders of magnitude lower compared to Fc. The rates calculated from both the TA and PL quenching data show that hole extraction by Fc is competitive to direct hole transfer from QD to PhPyr and validates the choice of hole mediators.

3.4.3 *Charge transfer from Fc to PhPyr*

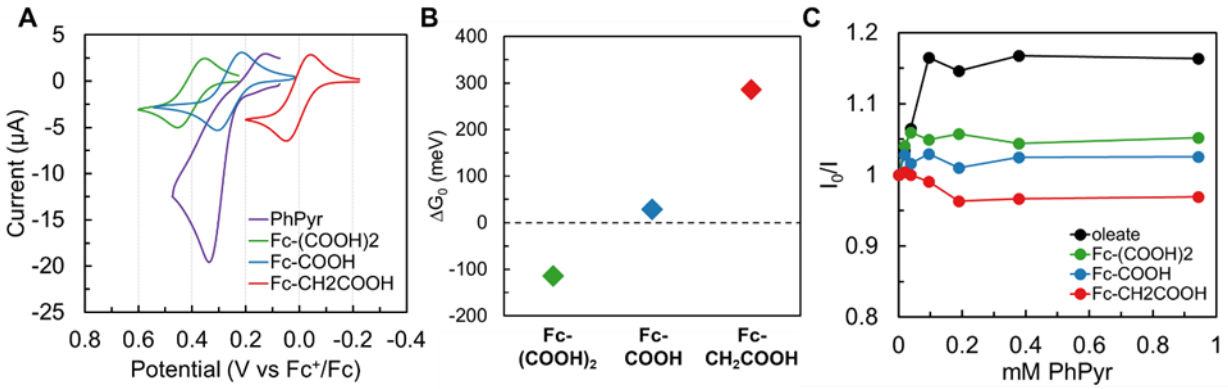

Figure 3.11. Driving force and charge transfer measurements from Fc ligands to PhPyr. (A) CVs of 0.5 mM Fc ligands and PhPyr; 0.15 M [NBu4][PF6], THF, glassy carbon working, Pt auxiliary, and Pt reference electrodes, 100 mV/s. (B) Estimated driving force of hole transfer from Fc^+ to PhPyr calculated from CVs. (C) Stern–Volmer plot for fluorescence quenching of CdS QDs ligated with oleate (black), Fc-$(COOH)_2$ (green), Fc-COOH (blue), and Fc-CH_2COOH (red) by successive addition of PhPyr (0–2500 equivalents relative to CdS) monitored at 470 nm.

We next focused on the second hole transfer step of the shuttle from Fc to the substrate, PhPyr. Typically, the energy levels of the band edges and trap states of QDs are difficult to define without involved spectroscopic or experimental techniques and many assumptions.[35,36] An advantage of our system is that since holes are localising to molecules with well-defined and easily measurable redox potentials, we can say with certainty what energy level the hole is sitting at.[37] We estimated

the potential of PhPyr to be 0.29 V vs Fc^+/Fc from the inflexion point of a CV measured at 100 mV/s.[38] According to the CVs, hole transfer from Fc^+-$(COOH)_2$ to PhPyr is ~115 meV downhill, from Fc^+-COOH is roughly thermoneutral, and from Fc^+-CH_2COOH is ~285 meV uphill (Figure 3.11B). Therefore, only Fc-$(COOH)_2$ may be able to function as a true hole shuttle.

We again performed PL quenching to probe the second hole transfer step of the shuttle (Figure 3.11C). We first ligated our CdS QDs with 10 equivalents of each Fc ligand to mimic catalytic conditions and used PhPyr as the quencher. For as-synthesised QDs, we observe direct transfer from QD to PhPyr and a deviation from linear quenching at higher concentrations, indicating adsorption of PhPyr to the QD.[9] Since we know that $k_{ht\ (Fc)} >> k_{ht\ (PhPyr)}$, we also know that the initial PL intensity I_0 of QDs ligated with Fc already accounts for some population of holes being localised on Fc. We see no quenching with Fc-CH_2COOH, demonstrating that neither direct transfer nor hole shuttling is occurring. We see weak quenching with Fc-COOH and Fc-$(COOH)_2$, which could be via direct or hole shuttling pathways. We hypothesise that the holes are weakly shuttling through Fc for these two ligands since the direct pathway was completely shut down for Fc-CH_2COOH, and it appears that the shuttle pathway is slower than the direct pathway.

We also performed TA on QDs pre-ligated with and added in PhPyr (Figure 3.19). We performed the same fitting procedures discussed in Section 3.4.2 and again extracted rates of charge transfer (Figure 3.12). The rates not significantly increased in the presence of PhPyr. By driving force arguments combined with the TA and PL quenching data, we see weak evidence for the shuttling pathway in the cases of Fc-$(COOH)_2$ and Fc-COOH, which appears to be very slow with minimal improvements on the rates of charge transfer.

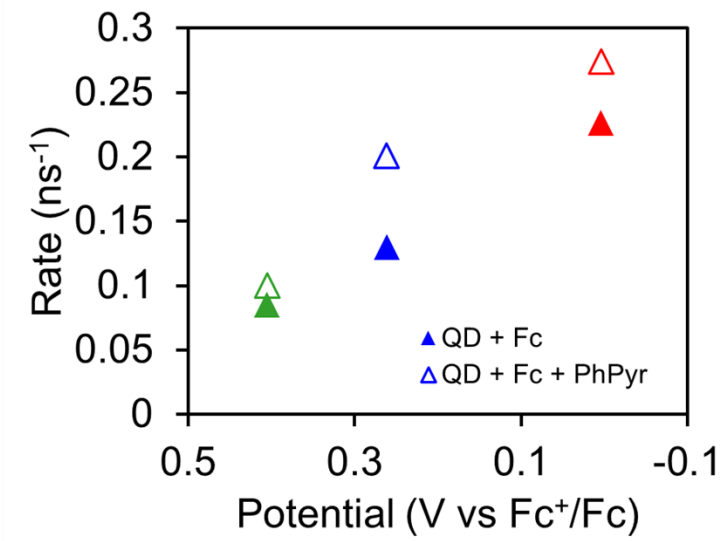

Figure 3.12. Weighted average charge transfer rates of QDs ligated with 10 eq of Fc ligands in the absence (filled triangle) and presence (empty triangle) or PhPyr.

Taking the catalytic and spectroscopic results together, we propose the following mechanism and an interplay between surface binding and hole shuttling. For Fc-$(COOH)_2$, we propose that the hole shuttle is operative but that it is bad for catalysis. Since the hole is localised on a specific location on the QD rather than delocalised, there is effectively lower probability of collision with a substrate molecule for transfer. Increasing coverage does not change the rate of reaction, so the barrier for the second step of the shuttle must still be too high. On the other end of the spectrum, the hole shuttle cannot operate for Fc-CH_2COOH. Therefore, the improved catalysis at 10 equivalents of coverage must be due to other factors. Since it is the weakest binder, we propose that in the 10 eq concentration regime, the ligands are dynamically exchanging and allowing substrates access to the QD. When the coverage is increased to 50 eq, more ligands are bound on the surface, and they are trapping holes but not shuttling them on to PhPyr to do productive catalysis. Since Fc-COOH is such a weak shuttle, we likely are only seeing minimal effects of this pathway, but rather surface binding effects are dominating as in the case of Fc-CH_2COOH.

3.4.4 *Effect of electron-trapping on hole transfer*

We performed TA on CdS QDs with phenazine-1-carboxylic acid and observed rapid charge transfer. When we monitor the ground state bleach at 434 nm, we can see that in the presence of phenazine, the bleach recovers much more quickly than CdS alone, indicative of charge transfer (Figure 3.13). We can fit the decay to five exponentials again and observe that the later time constants are much shorter in the presence of phenazine (Table 3.4). In addition, there is a sixth exponential that is 18 µs long in the presence of phenazine, indicating a long-lived charge-separated state. At this time, it is unclear whether this is the phenazine radical or triplet.

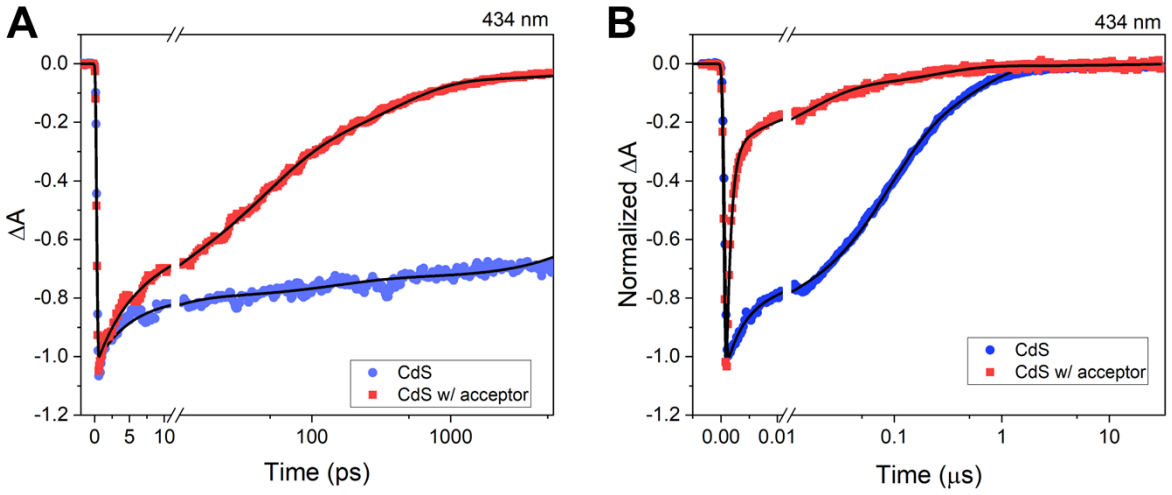

Figure 3.13. Decay kinetics of ground state bleach at 434 nm of CdS (blue) and CdS in the presence of phenazine (red) in the (A) fs - ns and (B) ns - µs regime.

Table 3.4. Fitted lifetimes from TA spectra.

	t_1 (ps)	t_2 (ps)	t_3 (ns)	t_4 (ns)	t_5 (ns)	t_6 (us)
CdS	5.1 ± 0.1	146 ± 4	2.46 ± 0.03	83.7 ± 0.6	551 ± 3	
CdS + phenazine	4.42 ± 0.08	42.2 ± 0.4	0.376 ± 0.004	15.6 ± 0.4	248 ± 9	18 ± 1

We also observe a broad photoinduced absorption feature from 500 – 700 nm in the presence of phenazine that we assign as the anionic radical (Figure 3.20).[39–41] We can monitor the decay of this feature and see a larger amplitude that lives longer compared to CdS (Figure 3.14). This long-lived charge separated state shows that phenazine is able to trap the electron and spatially separate it from the hole in the QD, prevent recombination, and increase the probability of hole transfer to PhPyr for catalysis. Since the hole wavefunction is still delocalised through the nanocrystal, the probability of collision with substrate is not affected as in the case of localisation on Fc.

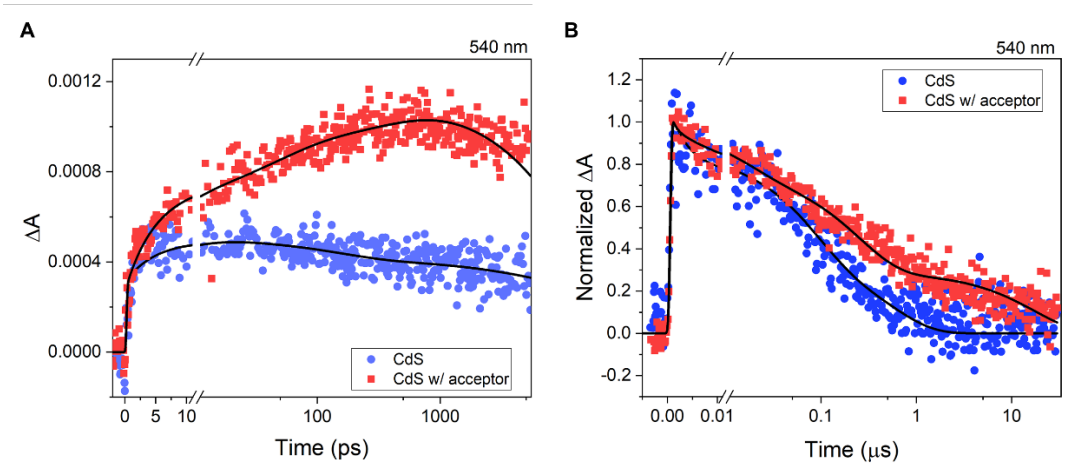

Figure 3.14. Decay kinetics of photoinduced absorption at 540 nm of CdS (blue) and CdS in the presence of phenazine (red) in the (A) fs – ns and (B) ns - μs regime.

This interpretation is complementary to HER systems, where for the 2-electron transfer reaction, trapping or quenching the hole promotes electron transfer for hydrogen production.[15,16,42–44] This concept has also been demonstrated by Eagle et al, who showed that localising holes at a dopant increases the rate of electron transfer to acceptor molecules.[45] Therefore for our particular system, it is possible that electron quenching is rate-limiting for hole transfer.

3.5 STABILITY

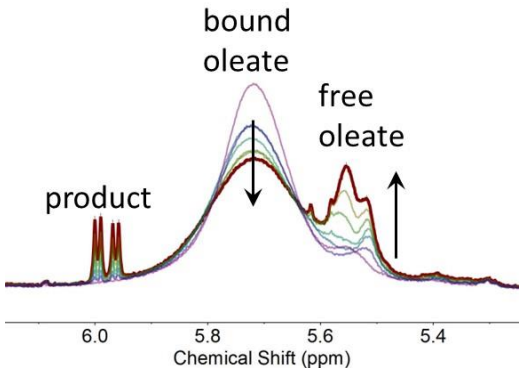

Figure 3.15. ^{1}H NMR of vinyl proton region of CdS QDs with native oleate ligands during catalysis, showing etching behaviour over time as product is formed. C_6D_6, 500 MHz, d1=10s.

While monitoring our reaction by ^{1}H NMR spectroscopy, we observe similar effects seen in Chapter 2 of ligand etching during catalysis (Figure 3.15). If we monitor the vinyl region, we find that as product is formed, oleate ligands are also becoming unbound from the surface.[46–48] Control experiments of QDs in solvent under illumination show that this does not happen in the absence of catalysis and is distinct from the intrinsic photocharging behaviour observed by other groups.[49]

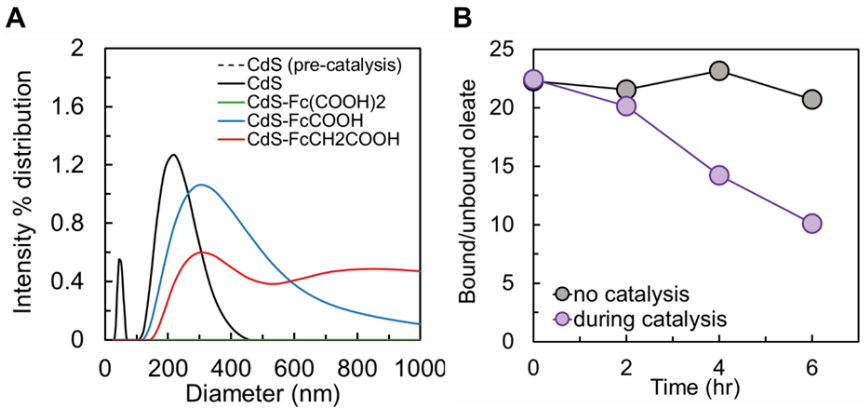

Figure 3.16. Stability and surface chemistry characterization during and after catalysis. (A) DLS measurements of CdS with different ligands before and after catalysis. (B) Ratio of bound vs unbound oleate ligands fit from ^{1}H NMR of QDs during catalysis and in solvent under illumination.

While our hole-accepting ligands do not appear to improve catalysis, we see a very encouraging result with regards to the stability of the catalyst. At the same product formation, we took an aliquot from the reaction solution and measured the size of the particles by dynamic light scattering (DLS). We found evidence of large aggregates up to ~ 400 nm in size for native CdS after catalysis, and over 1 µm in size for CdS ligated in Fc-COOH and Fc-CH_2COOH (Figure 3.16A). This was also reflected in visible precipitation observed in these samples. We saw no aggregation in CdS ligated with Fc-$(COOH)_2$, as in the control case of native CdS before catalysis (baseline of Figure 3.16A). We propose that the Fc-$(COOH)_2$ acting as a hole shuttle slows down the rate of catalysis, but also prevents the degradation of the catalyst by inhibiting the buildup of holes on the inorganic surface that leads to sulphur oxidation as seen in Chapter 2.

3.6 CONCLUSIONS

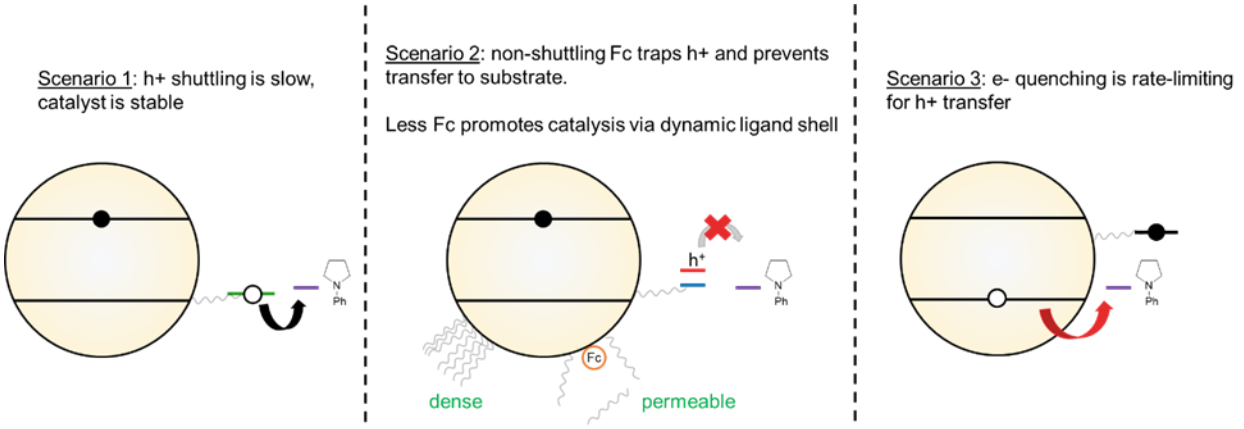

Scheme 3.3. Different charge transfer pathways explored in this study and effects on catalysis.

We have demonstrated the utility of three Fc carboxylic acid derivatives as hole-accepting ligands on the surface of CdS QDs. From our catalytic results, we observe three scenarios illustrated in Scheme 3.3. Firstly, a hole-shuttling system exhibits the worst catalytic activity but confers greater protection from aggregation, presumably by preventing a build-up of destructive

holes (Scenario 1). For non-shuttling Fc's, a dynamic ligand shell increases the rate of reaction via surface access (low equivalents regime) but at higher Fc concentrations, charge transfer to substrate is inhibited (Scenario 2). In contrast, trapping the opposite charge carrier (electron) increases the rate of reaction ~ 4-fold. Drawing parallels with HER systems, where hole quenching is rate-limiting for a 2-electron transfer reaction, it appears that electron quenching is rate-limiting for hole transfer in our system (Scenario 3).

Our work adds to the current understanding of the mechanisms that control charge transfer in organic photoredox transformations and should be explored further to improve QD catalysts. In addition, our strategy is a viable approach for protecting nanostructures that are very susceptible to degradation, such as anisotropic heterostructures that have been shown to improve catalysis in aqueous systems[50] but have scarcely been realised as photocatalysts for organic reactions.

3.7 EXPERIMENTAL

3.7.1 *Materials*

All experiments, unless otherwise noted, were performed under an inert N_2 atmosphere using a glovebox or standard Schlenk techniques. All glassware was dried in a 160 °C oven overnight prior to use. Oleic acid (90%), anhydrous hexadecane (≥99%), tetramethylthiourea (98%), biphenyl (99.5%), diphenyl ether (98%), anhydrous methanol (99.8%), anhydrous benzene (99.8%), 1,1′-ferrocenedicarboxylic acid (96%), ferrocenecarboxylic acid (97%), cesium acetate (99.99% trace metals basis), 1,3,5-trimethoxybenzene (≥99%) were purchased from MilliporeSigma and used as received. Phenazine-1-carboxylic acid (>98%), phenyl trans-beta-styryl sulfone (98%), 1-phenylpyrrolidine (>98%) were purchased from Fisher Scientific and used as received. Ferroceneacetic acid (97%) was purchased from TCI America and used as received.

Benzene-D6 (D, 99.5%) was purchased from Cambridge Isotope Lab and purified by distillation and stored over activated 4 Å molecular sieves. Toluene (HPLC grade) and tetrahydrofuran THF (HPLC grade) were purchased from Fisher Scientific, purged with argon, and stored over activated 4 Å molecular sieves. Tetrabutylammonium hexafluorophosphate ([TBA][PF6], 98%) was purchased from VWR Scientific and recrystallised twice from ethanol. Royal-Blue (448nm) Rebel LEDs were purchased from Luxeon Star LEDs.

3.7.2 *Synthesis of cadmium oleate*

Cadmium oxide (5.14 g, 40 mmol) was stirred with 55 mL acetonitrile. Trifluoroacetic acid (0.86mL, 11.2 mmol) then trifluoroacetic anhydride (6.12 mL, 44 mmol) were added dropwise. This mixture was stirred for an hour and turned from heterogeneous with red CdO to clear. In a separate flask, oleic acid (22.6g, 80 mmol), dichloromethane (400 mL) and triethylamine (13.9 mL, 100 mmol) were combined. The cadmium solution was added dropwise with stirring and then heated to 60 °C. The now clear solution was allowed to slowly cool to room temperature, then put in a freezer. The white powder precipitate was isolated with vacuum filtration and washed with acetonitrile.

3.7.3 *Synthesis of CdS QDs*

The procedure was modified from Hamachi et al.[51] In a 250 mL 3-neck flask, degas cadmium oleate (1.215 g, 1.8 mmol), technical grade oleic acid (1.15 mL, 3.6 mmol) and hexadecane (60 mL) for ~1 hr under vacuum at 90 °C. Meanwhile, dissolve tetramethylthiourea (0.198 g, 1.5 mmol) in biphenyl/diphenyl ether (3 mL). Under N_2, raise temperature of reaction flask to 230 °C. Swiftly inject sulphur precursor solution and monitor reaction by UV-vis absorption spectroscopy.

Quench reaction when absorbance profile stops changing by removing the flask from heat. This reaction proceeded for 2.5 hr. To purify the particles, vacuum distill off hexadecane. Re-dissolve particles in toluene and precipitate with methanol for a total of three rounds of purification. Perform one final centrifuge spin in toluene and filter dissolved QDs through 0.45 µm PTFE filter. The QDs were quantified using a sizing curve established by Yu et al.[52] The dots were ~ 5 nm with an absorbance maximum at 454 nm, an emission maximum at 470 nm and a broad trap emission feature centred at 720 nm, and low/negligible photoluminescence quantum yield (~2 %) (Figure 3.17).

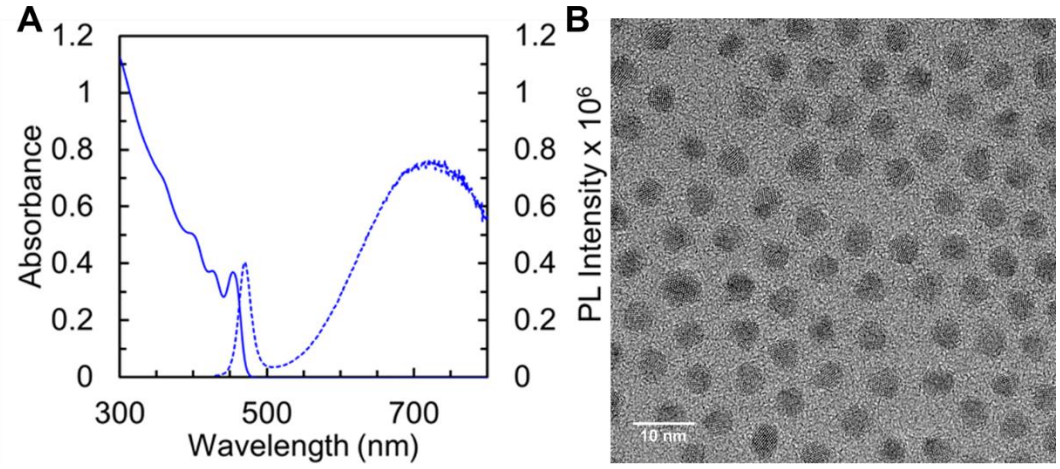

Figure 3.17. Properties of oleate-capped CdS QDs. (A) Absorption and photoluminescence spectra. (B) TEM image.

3.7.4 *Synthesis of 3,5-di-tert-butylphenylacetic acid*

3,5-di-tert-butylbenzyl bromide (9.921 g), KCN (2.279 g), and 18-crown-6 (9.354 g) were placed in a 250 mL round-bottom flask and 110 mL of acetonitrile was added. The solution was refluxed for 4.5 hours, then diluted with water (200 mL). The product was extracted with 3 x 100 mL of ether, which was then removed by rotary evaporation to yield 9.3315 g of crude product.

The crude product was then dissolved in ethanol (300 mL) and to this solution 12.5 M NaOH (100 mL) was added. This solution was brought to reflux and left to react for 16.5 hours which resulted in a biphasic mixture. Conc. HCl was added to the organic layer with stirring until pH 0.5, after which the solution was concentrated by rotary evaporation to yield a white solid. This was redissolved in ether, filtered, and the ether from the filtrate was removed by rotary evaporation. The resulting white solid was suspended in cold pentane and filtered. White crystals were washed with cold pentane and then pumped down at 50 mTorr overnight to remove any residual solvent. The final product was a fluffy white solid (3.300 g, mp = 113 C -120 C).

3.7.5 *Photocatalysis*

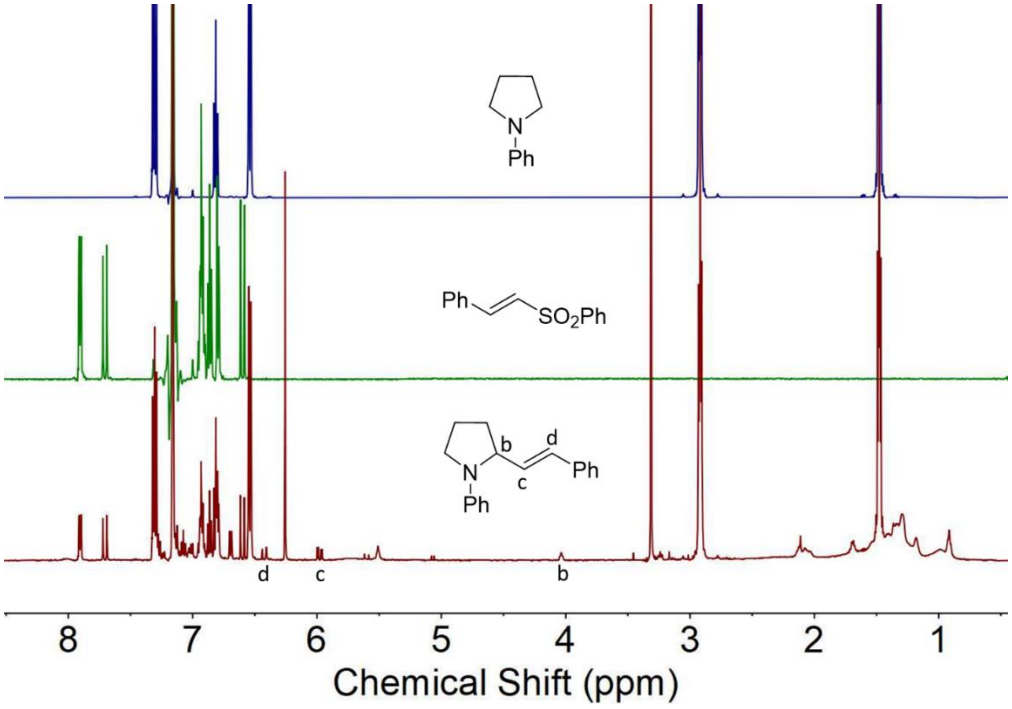

Figure 3.18. Representative ^{1}H NMR spectrum in C_6D_6 (red) used for quantification of product using 1,3,5-trimethoxybenzene as an internal standard. Starting material shown in blue (1-phenylpyrrolidine) and green (phenyl trans-styryl sulfone), red spectrum was taken after photocatalysis. A 500 MHz instrument with d1=10 s was used.

A scintillation vial was prepared with a stir bar, 8.33 nmol of CdS QDs (0.1% loading) and 10 equivalents of each ligand (from stock solutions) and stirred overnight for ligand exchange. Solvent was removed in vacuo and cesium acetate (4.7 mg, 25 μmol) was added. Phenyl trans-styryl sulfone (2 mg, 8.2 μmol) and 1,3,5-trimethoxybenzene were added via a stock solution in C6D6 (1 mL). Lastly, 1-phenylpyrrolidine (3 mg, 20 μmol) was added. The vial was sealed and entirely wrapped with electrical tape and illuminated with a 450 nm LED at 1W (700mA). The solution was transferred to a J-Young tube for NMR quantification with 1,3,5-trimethoxybenzene as the internal standard.

3.7.6 *Electrochemical titrations*

The working electrode was a glassy carbon disc with a diameter of 3.0 mm (BASi) which was polished with 5, 1, and 0.05 μm polishing compound, with 5 minutes sonication in ultrahigh purity water (R = 18 M Ω) between polishing steps. The auxiliary electrode was platinum wire (BASi) and the pseudo-reference electrode was a silver wire in a fritted tube (BASi) filled with 0.15 M electrolyte solution. In a typical titration experiment, oleate-capped CdS QDs were suspended in THF (0.05 mM). With stirring, enough electrolyte to bring the solution to 0.15 M [NBu4][PF6] was added dropwise to prevent precipitation of QDs. Separately, a solution of the ligand to be measured was prepared (1 mM, 5 mL total volume) in 0.15 M [NBu4][PF6]/THF. CV measurements were taken at a relatively slow scan rate of 10 mV/s to minimize effects of ohmic current in the modestly resistive THF solution. For each step of the titration, 0.0025 equivalents of QD were added to the Fc solution. The solution was stirred for 10 seconds and after stirring had completely stopped, a CV measurement was taken and more QDs were added. This was repeated until 0.024 equivalents of QD were added.

3.7.7 *Electrochemical simulations*

All electrochemical simulations were performed in DigiElch v.8. First, the initial voltammogram was fit to determine the diffusion coefficient and the standard heterogeneous rate constant. These values were then retained for the subsequent titration voltammograms. We assumed that the standard heterogeneous rate constant was the same for Fc bound and not bound to QDs and that the diffusion coefficient of the QDs (and therefore the diffusion coefficient of Fc bound to QD) was 1.72*10-6 cm2/s as determined by the Randles-Sevcik equation. Dilution of the Fc during titration was accounted for in the simulation software. Utilizing these known and assumed parameters, the remaining values to be fit were the equilibrium constants of binding (K1 and K2). DigiElch's global minimum finder was used to fit all CVs in a titration series to a single model of these equilibrium constants.

3.7.8 *Transient absorption*

The transient absorption (TA) setup has been described in a previous publication. CdS QDs were exchanged overnight with 10 equivalents of each Fc ligand. The solvent was removed in vacuo and the QDs were redissolved in benzene. An approximately 0.3 OD sample of exchanged QDs in a 1 mm cuvette was pumped with a ~250 µW, 450 nm pulse and probed with a broadband white light probe generated using CaF. Samples were stirred to avoid Auger ionization and provide illumination of the entire sample. Data was collected over the femtosecond to microsecond regime.

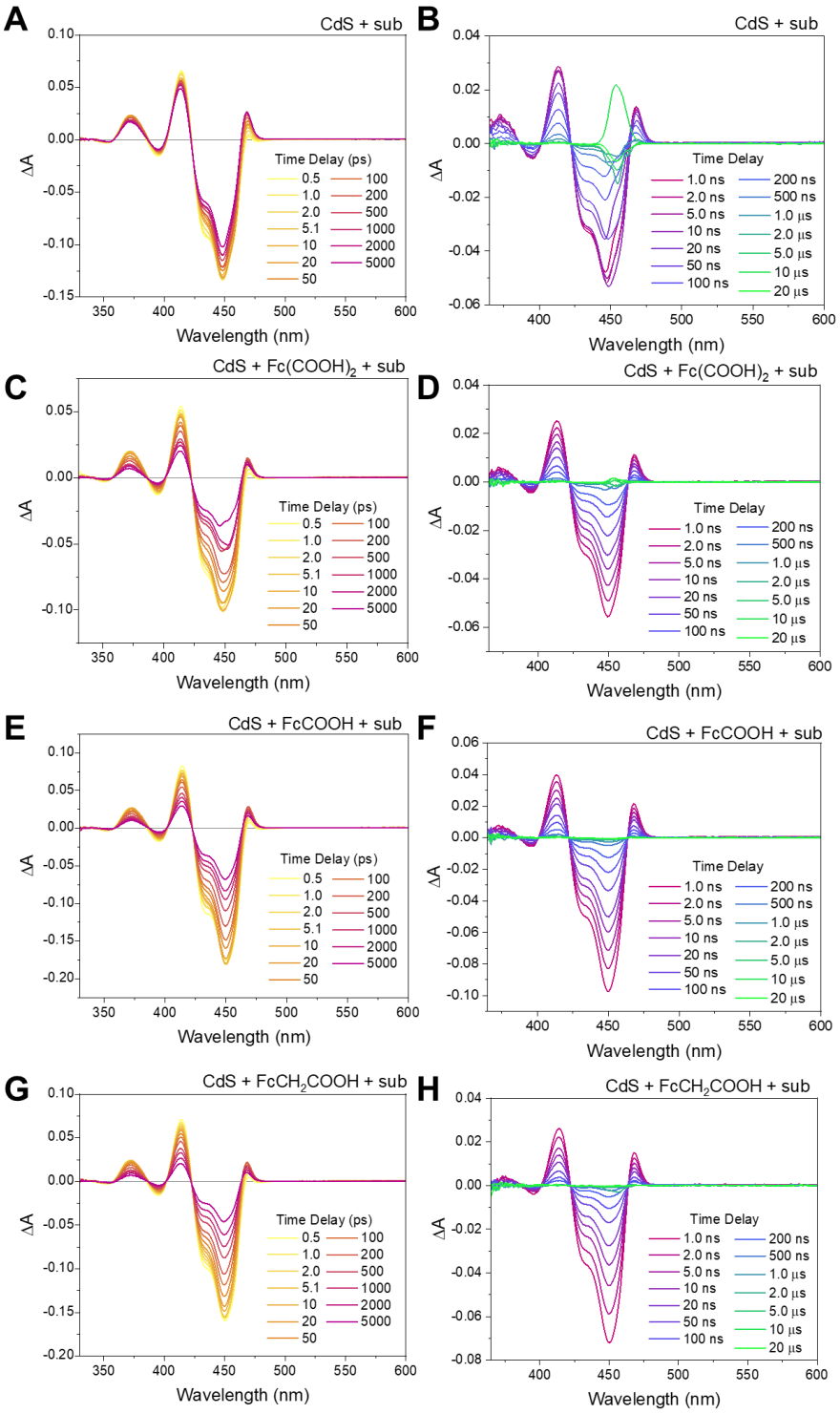

Figure 3.19. TA spectra of (A-B) CdS + PhPyr, (C-D) CdS + Fc-$(COOH)_2$ + PhPyr, (E-F) CdS + Fc-COOH + PhPyr, (G-H) CdS + Fc-CH_2COOH + PhPyr in the fs - ns regime (left column) and ns - μs regime (right column).

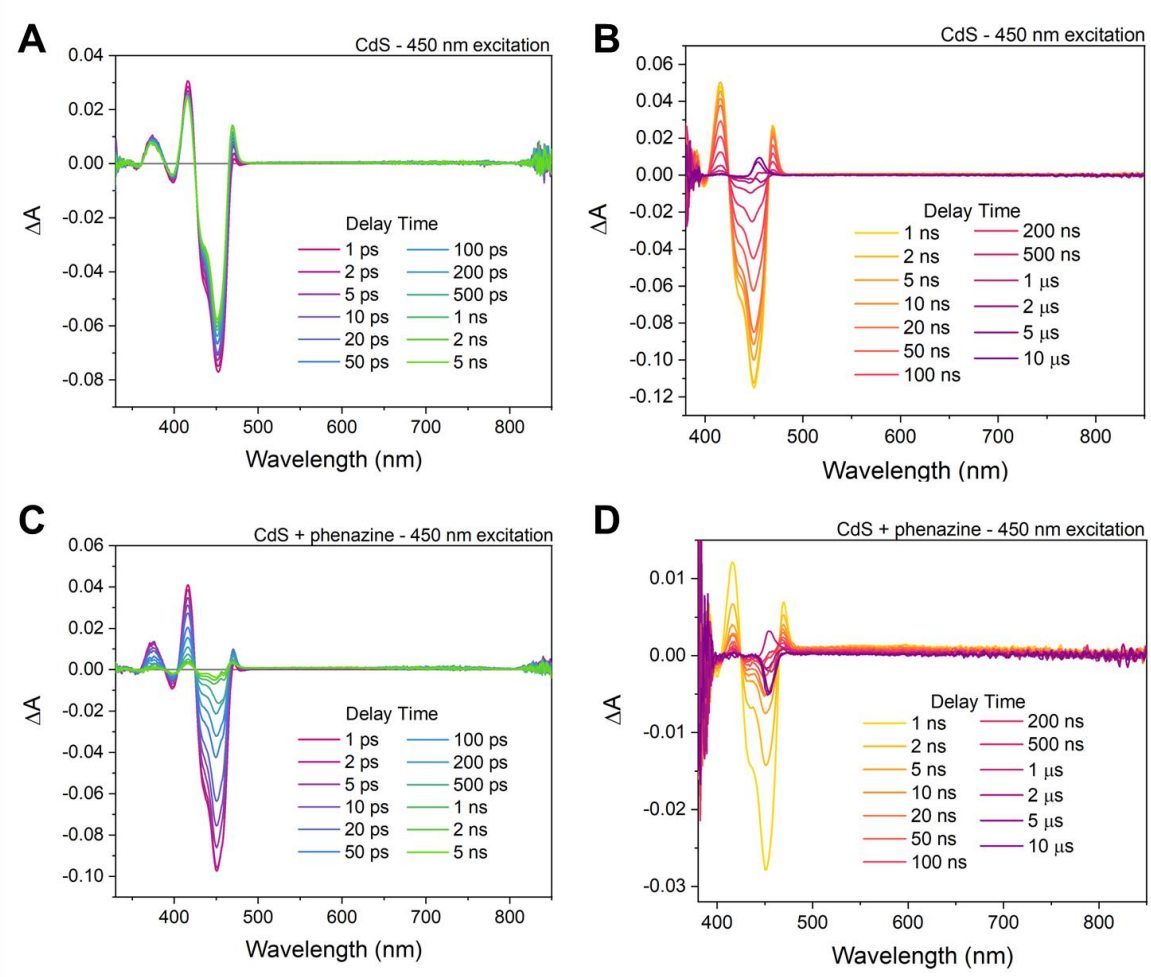

Figure 3.20. TA spectra of (A-B) CdS and (C-D) CdS + phenazine-1-carboxylic acid in the fs - ns regime (left column) and ns - μs regime (right column).

3.7.9 *Photoluminescence quenching*

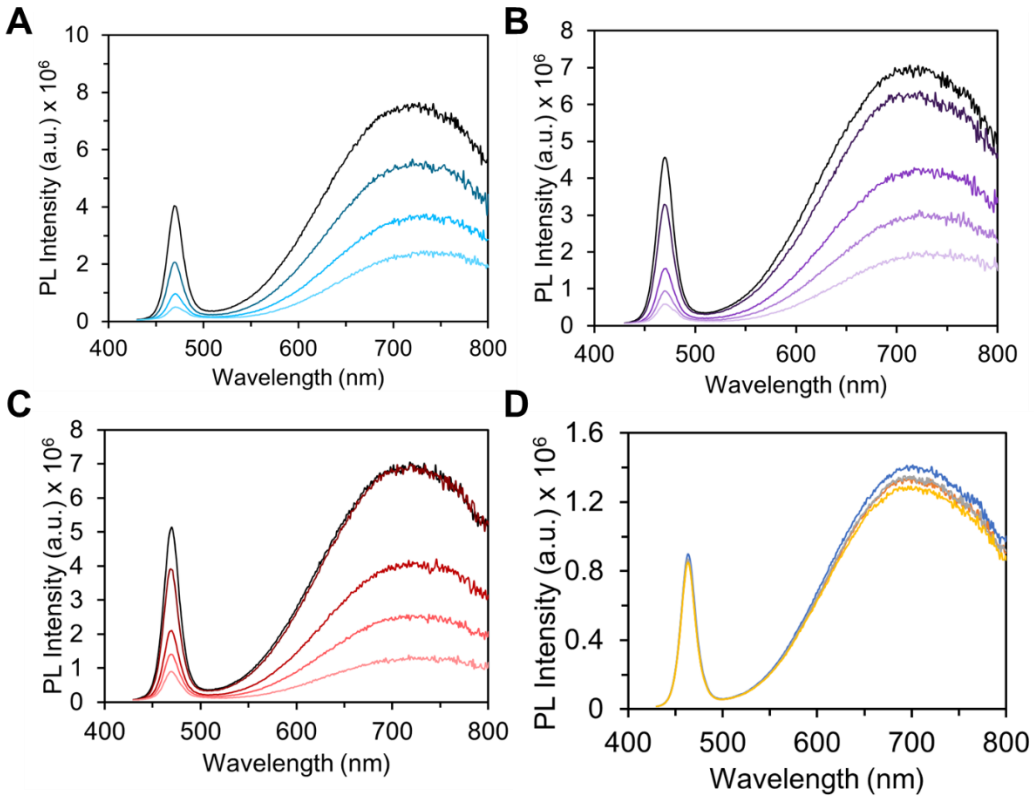

Figure 3.21. Raw PL quenching spectra of CdS QDs titrated with (A) Fc-$(COOH)_2$, (B) Fc-COOH, (C) Fc-CH_2COOH, (D) PhPyr.

A 0.45 µM solution of CdS QDs was prepared in benzene and 2.5 mL (1.125 nmol) were loaded into a quartz cuvette. Stock solutions of 1.13 mM Fc quencher were prepared and titrated into the cuvette. The QD solution was allowed to equilibrate for at least 15 minutes before collecting photoluminescence spectra. For PL quenching with PhPyr, CdS QDs were first exchanged with 10 equivalents of Fc ligands overnight. Next, 0.45 µM solutions of exchanged QDs were prepared in benzene and 2.5 mL (1.125 nmol) were loaded into a quartz cuvette. A stock solution of 56.6 mM PhPyr was prepared and titrated into the cuvettes. The QD solutions were allowed to equilibrate for at least 15 minutes before collecting photoluminescence spectra. Cuvettes were sealed with electrical tape during scans to maintain inert atmosphere.

3.7.10 *Characterisation methods*

UV-Vis spectra were collected on a Cary 5000 spectrophotometer from Agilent. Fluorescence spectra were collected on a Horiba Jobin Yvon FluoroMax4 fluorescence spectrophotometer. 1H NMR spectra were collected on a 500 MHz Bruker Avance spectrometer. TEM images were collected on an FEI Tecnai G2 F20 microscope. DLS measurements were taken on a Malvern Zetasizer Nano ZS.

3.8 REFERENCES

(1) Dou, F. Y.; Harvey, S. M.; Mason, K. G.; Homer, M. K.; Gamelin, D. R.; Cossairt, B. M. Effect of a Redox-Mediating Ligand Shell on Photocatalysis by CdS Quantum Dots. *The Journal of Chemical Physics* **2023**, *158* (18), 184705. https://doi.org/10.1063/5.0144896.

(2) Veamatahau, A.; Jiang, B.; Seifert, T.; Makuta, S.; Latham, K.; Kanehara, M.; Teranishi, T.; Tachibana, Y. Origin of Surface Trap States in CdS Quantum Dots: Relationship between Size Dependent Photoluminescence and Sulfur Vacancy Trap States. *Phys. Chem. Chem. Phys.* **2014**, *17* (4), 2850–2858. https://doi.org/10.1039/C4CP04761C.

(3) Logunov, S.; Green, T.; Marguet, S.; El-Sayed, M. A. Interfacial Carriers Dynamics of CdS Nanoparticles. *J. Phys. Chem. A* **1998**, *102* (28), 5652–5658. https://doi.org/10.1021/jp980387g.

(4) Woodall, D. L.; Tobias, A. K.; Jones, M. Resolving Carrier Recombination in CdS Quantum Dots: A Time-Resolved Fluorescence Study. *Chemical Physics* **2016**, *471*, 2–10. https://doi.org/10.1016/j.chemphys.2015.10.011.

(5) Olshansky, J. H.; Balan, A. D.; Ding, T. X.; Fu, X.; Lee, Y. V.; Alivisatos, A. P. Temperature-Dependent Hole Transfer from Photoexcited Quantum Dots to Molecular Species: Evidence for Trap-Mediated Transfer. *ACS Nano* **2017**, *11* (8), 8346–8355. https://doi.org/10.1021/acsnano.7b03580.

(6) Wu, K.; Du, Y.; Tang, H.; Chen, Z.; Lian, T. Efficient Extraction of Trapped Holes from Colloidal CdS Nanorods. *J. Am. Chem. Soc.* **2015**, *137* (32), 10224–10230. https://doi.org/10.1021/jacs.5b04564.

(7) Nagelj, N.; Brumberg, A.; Peifer, S.; Schaller, R. D.; Olshansky, J. H. Compositionally Tuning Electron Transfer from Photoexcited Core/Shell Quantum Dots via Cation Exchange. *J. Phys. Chem. Lett.* **2022**, *13* (14), 3209–3216. https://doi.org/10.1021/acs.jpclett.2c00333.

(8) Zhu, H.; Yang, Y.; Hyeon-Deuk, K.; Califano, M.; Song, N.; Wang, Y.; Zhang, W.; Prezhdo, O. V.; Lian, T. Auger-Assisted Electron Transfer from Photoexcited Semiconductor Quantum Dots. *Nano Lett.* **2014**, *14* (3), 1263–1269. https://doi.org/10.1021/nl4041687.

(9) Uematsu, T.; Shimomura, E.; Torimoto, T.; Kuwabata, S. Evaluation of Surface Ligands on Semiconductor Nanoparticle Surfaces Using Electron Transfer to Redox Species. *J. Phys. Chem. C* **2016**, *120* (29), 16012–16023. https://doi.org/10.1021/acs.jpcc.5b12698.

(10) Wu, X.; Xie, S.; Liu, C.; Zhou, C.; Lin, J.; Kang, J.; Zhang, Q.; Wang, Z.; Wang, Y. Ligand-Controlled Photocatalysis of CdS Quantum Dots for Lignin Valorization under Visible Light. *ACS Catal.* **2019**, *9* (9), 8443–8451. https://doi.org/10.1021/acscatal.9b02171.

(11) Zhang, Z.; Edme, K.; Lian, S.; Weiss, E. A. Enhancing the Rate of Quantum-Dot-Photocatalyzed Carbon–Carbon Coupling by Tuning the Composition of the Dot's Ligand Shell. *J. Am. Chem. Soc.* **2017**, *139* (12), 4246–4249. https://doi.org/10.1021/jacs.6b13220.

(12) Aruda, K. O.; Bohlmann Kunz, M.; Tagliazucchi, M.; Weiss, E. A. Temperature-Dependent Permeability of the Ligand Shell of PbS Quantum Dots Probed by Electron Transfer to Benzoquinone. *J. Phys. Chem. Lett.* **2015**, *6* (14), 2841–2846. https://doi.org/10.1021/acs.jpclett.5b01256.

(13) Zeng, S.; Li, Z.; Tan, W.; Si, J.; Huang, Z.; Hou, X. Ultrafast Electron Transfer Dynamics Affected by Ligand Chain Length in InP/ZnS Core/Shell Quantum Dots. *J. Phys. Chem. C* **2022**, *126* (21), 9091–9098. https://doi.org/10.1021/acs.jpcc.2c01483.

(14) Levi, A.; Verbitsky, L.; Waiskopf, N.; Banin, U. Sulfide Ligands in Hybrid Semiconductor–Metal Nanocrystal Photocatalysts: Improved Hole Extraction and Altered Catalysis. *ACS Appl. Mater. Interfaces* **2022**, *14* (1), 647–653. https://doi.org/10.1021/acsami.1c17304.

(15) Yu, S.; Fan, X.-B.; Wang, X.; Li, J.; Zhang, Q.; Xia, A.; Wei, S.; Wu, L.-Z.; Zhou, Y.; Patzke, G. R. Efficient Photocatalytic Hydrogen Evolution with Ligand Engineered All-Inorganic InP and InP/ZnS Colloidal Quantum Dots. *Nat Commun* **2018**, *9* (1), 4009. https://doi.org/10.1038/s41467-018-06294-y.

(16) Li, X.-B.; Liu, B.; Wen, M.; Gao, Y.-J.; Wu, H.-L.; Huang, M.-Y.; Li, Z.-J.; Chen, B.; Tung, C.-H.; Wu, L.-Z. Hole-Accepting-Ligand-Modified CdSe QDs for Dramatic Enhancement of Photocatalytic and Photoelectrochemical Hydrogen Evolution by Solar Energy. *Advanced Science* **2016**, *3* (4), 1500282. https://doi.org/10.1002/advs.201500282.

(17) Wu, K.; Chen, Z.; Lv, H.; Zhu, H.; Hill, C. L.; Lian, T. Hole Removal Rate Limits Photodriven H2 Generation Efficiency in CdS-Pt and CdSe/CdS-Pt Semiconductor Nanorod–Metal Tip Heterostructures. *J. Am. Chem. Soc.* **2014**, *136* (21), 7708–7716. https://doi.org/10.1021/ja5023893.

(18) Berr, M. J.; Wagner, P.; Fischbach, S.; Vaneski, A.; Schneider, J.; Susha, A. S.; Rogach, A. L.; Jäckel, F.; Feldmann, J. Hole Scavenger Redox Potentials Determine Quantum Efficiency

and Stability of Pt-Decorated CdS Nanorods for Photocatalytic Hydrogen Generation. *Appl. Phys. Lett.* **2012**, *100* (22), 223903. https://doi.org/10.1063/1.4723575.

(19) Yanagi, R.; Zhao, T.; Solanki, D.; Pan, Z.; Hu, S. Charge Separation in Photocatalysts: Mechanisms, Physical Parameters, and Design Principles. *ACS Energy Lett.* **2022**, *7* (1), 432–452. https://doi.org/10.1021/acsenergylett.1c02516.

(20) Anson, C. W.; Stahl, S. S. Mediated Fuel Cells: Soluble Redox Mediators and Their Applications to Electrochemical Reduction of O2 and Oxidation of H2, Alcohols, Biomass, and Complex Fuels. *Chem. Rev.* **2020**, *120* (8), 3749–3786. https://doi.org/10.1021/acs.chemrev.9b00717.

(21) Tarafder, K.; Surendranath, Y.; Olshansky, J. H.; Alivisatos, A. P.; Wang, L.-W. Hole Transfer Dynamics from a CdSe/CdS Quantum Rod to a Tethered Ferrocene Derivative. *J. Am. Chem. Soc.* **2014**, *136* (13), 5121–5131. https://doi.org/10.1021/ja500936n.

(22) Ding, T. X.; Olshansky, J. H.; Leone, S. R.; Alivisatos, A. P. Efficiency of Hole Transfer from Photoexcited Quantum Dots to Covalently Linked Molecular Species. *J. Am. Chem. Soc.* **2015**, *137* (5), 2021–2029. https://doi.org/10.1021/ja512278a.

(23) Olshansky, J. H.; Ding, T. X.; Lee, Y. V.; Leone, S. R.; Alivisatos, A. P. Hole Transfer from Photoexcited Quantum Dots: The Relationship between Driving Force and Rate. *J. Am. Chem. Soc.* **2015**, *137* (49), 15567–15575. https://doi.org/10.1021/jacs.5b10856.

(24) Dolui, P.; Hazra, S.; Deb, M.; Elias, A. J. Picolinamide Assisted Oxidation of CH2 Groups Bound to Organic and Organometallic Compounds Using Ferrocene as a Catalyst. *Organometallics* **2019**, *38* (9), 2015–2021. https://doi.org/10.1021/acs.organomet.9b00085.

(25) Hernández-Muñoz, L. S.; Galano, A.; Astudillo-Sánchez, P. D.; Abu-Omar, M. M.; González, F. J. The Mechanism of Mediated Oxidation of Carboxylates with Ferrocene as Redox Catalyst in Absence of Grafting Effects. An Experimental and Theoretical Approach. *Electrochimica Acta* **2014**, *136*, 542–549. https://doi.org/10.1016/j.electacta.2014.04.189.

(26) Henckel, D. A.; Enright, M. J.; Panahpour Eslami, N.; Kroupa, D. M.; Gamelin, D. R.; Cossairt, B. M. Modeling Equilibrium Binding at Quantum Dot Surfaces Using Cyclic Voltammetry. *Nano Lett.* **2020**, *20* (4), 2620–2624. https://doi.org/10.1021/acs.nanolett.0c00162.

(27) Kessler, M. L.; Kelm, J. E.; Starr, H. E.; Cook, E. N.; Miller, J. D.; Rivera, N. A.; Hsu-Kim, H.; Dempsey, J. L. Unraveling Changes to PbS Nanocrystal Surfaces Induced by Thiols. *Chem. Mater.* **2022**, *34* (4), 1710–1721. https://doi.org/10.1021/acs.chemmater.1c03888.

(28) Anderson, N. C.; Hendricks, M. P.; Choi, J. J.; Owen, J. S. Ligand Exchange and the Stoichiometry of Metal Chalcogenide Nanocrystals: Spectroscopic Observation of Facile Metal-Carboxylate Displacement and Binding. *J. Am. Chem. Soc.* **2013**, *135* (49), 18536–18548. https://doi.org/10.1021/ja4086758.

(29) Noble, A.; MacMillan, D. W. C. Photoredox α-Vinylation of α-Amino Acids and N-Aryl Amines. *J. Am. Chem. Soc.* **2014**, *136* (33), 11602–11605. https://doi.org/10.1021/ja506094d.

(30) Hens, Z. Ligands on Nanocrystal Surfaces, the 1H Nuclear Magnetic Resonance Fingerprint. *Acc. Chem. Res.* **2023**. https://doi.org/10.1021/acs.accounts.3c00170.

(31) De Roo, J. The Surface Chemistry of Colloidal Nanocrystals Capped by Organic Ligands. *Chem. Mater.* **2023**, *35* (10), 3781–3792. https://doi.org/10.1021/acs.chemmater.3c00638.

(32) Dümbgen, K. C.; Infante, I.; Hens, Z. Localizing Oleylamine Ligands on Amine–Halide Copassivated Indium Phosphide Nanocrystals. *Chem. Mater.* **2023**. https://doi.org/10.1021/acs.chemmater.3c00565.

(33) La Croix, A. D.; O'Hara, A.; Reid, K. R.; Orfield, N. J.; Pantelides, S. T.; Rosenthal, S. J.; Macdonald, J. E. Design of a Hole Trapping Ligand. *Nano Lett.* **2017**, *17* (2), 909–914. https://doi.org/10.1021/acs.nanolett.6b04213.

(34) Homer, M. K.; Kuo, D.-Y.; Dou, F. Y.; Cossairt, B. M. Photoinduced Charge Transfer from Quantum Dots Measured by Cyclic Voltammetry. *J. Am. Chem. Soc.* **2022**, *144* (31), 14226–14234. https://doi.org/10.1021/jacs.2c04991.

(35) Murphy, I. A.; Rice, P. S.; Monahan, M.; Zasada, L. B.; Miller, E. M.; Raugei, S.; Cossairt, B. M. Covalent Functionalization of Nickel Phosphide Nanocrystals with Aryl-Diazonium Salts. *Chem. Mater.* **2021**, *33* (24), 9652–9665. https://doi.org/10.1021/acs.chemmater.1c03255.

(36) Hartley, C. L.; Dempsey, J. L. Revealing the Molecular Identity of Defect Sites on PbS Quantum Dot Surfaces with Redox-Active Chemical Probes. *Chem. Mater.* **2021**, *33* (7), 2655–2665. https://doi.org/10.1021/acs.chemmater.1c00520.

(37) Hartley, C. L.; Kessler, M. L.; Dempsey, J. L. Molecular-Level Insight into Semiconductor Nanocrystal Surfaces. *J. Am. Chem. Soc.* **2021**, *143* (3), 1251–1266. https://doi.org/10.1021/jacs.0c10658.

(38) Espinoza, E. M.; Clark, J. A.; Soliman, J.; Derr, J. B.; Morales, M.; Vullev, V. I. Practical Aspects of Cyclic Voltammetry: How to Estimate Reduction Potentials When Irreversibility Prevails. *J. Electrochem. Soc.* **2019**, *166* (5), H3175. https://doi.org/10.1149/2.0241905jes.

(39) Ghule, S.; Dash, S. R.; Bagchi, S.; Joshi, K.; Vanka, K. Predicting the Redox Potentials of Phenazine Derivatives Using DFT-Assisted Machine Learning. *ACS Omega* **2022**, *7* (14), 11742–11755. https://doi.org/10.1021/acsomega.1c06856.

(40) Cruz, C. de la; Molina, A.; Patil, N.; Ventosa, E.; Marcilla, R.; Mavrandonakis, A. New Insights into Phenazine-Based Organic Redox Flow Batteries by Using High-Throughput DFT Modelling. *Sustainable Energy & Fuels* **2020**, *4* (11), 5513–5521. https://doi.org/10.1039/D0SE00687D.

(41) pH-Induced Changes in Electronic Absorption and Fluorescence Spectra of Phenazine Derivatives. *Spectrochimica Acta Part A: Molecular and Biomolecular Spectroscopy* **2007**, *66* (4–5), 849–859. https://doi.org/10.1016/j.saa.2006.04.027.

(42) Ye, Y.; Wang, X.; Ye, S.; Xu, Y.; Feng, Z.; Li, C. Charge-Transfer Dynamics Promoted by Hole Trap States in CdSe Quantum Dots–Ni2+ Photocatalytic System. *J. Phys. Chem. C* **2017**, *121* (32), 17112–17120. https://doi.org/10.1021/acs.jpcc.7b05061.

(43) Bang, J.; Das, S.; Yu, E.-J.; Kim, K.; Lim, H.; Kim, S.; Hong, J. W. Controlled Photoinduced Electron Transfer from InP/ZnS Quantum Dots through Cu Doping: A New Prototype for the Visible-Light Photocatalytic Hydrogen Evolution Reaction. *Nano Lett.* **2020**, *20* (9), 6263–6271. https://doi.org/10.1021/acs.nanolett.0c00983.

(44) H. Edwards, E.; A. Fertig, A.; P. McClelland, K.; T. Meidenbauer, M.; Chakraborty, S.; D. Krauss, T.; L. Bren, K.; M. Matson, E. Enhancing the Activity of Photocatalytic Hydrogen Evolution from CdSe Quantum Dots with a Polyoxovanadate Cluster. *Chemical Communications* **2020**, *56* (62), 8762–8765. https://doi.org/10.1039/D0CC03163A.

(45) Eagle, F. W.; Harvey, S.; Beck, R.; Li, X.; Gamelin, D. R.; Cossairt, B. M. Enhanced Charge Transfer from Coinage Metal Doped InP Quantum Dots. *ACS Nanosci. Au* **2023**. https://doi.org/10.1021/acsnanoscienceau.3c00029.

(46) Fritzinger, B.; Capek, R. K.; Lambert, K.; Martins, J. C.; Hens, Z. Utilizing Self-Exchange To Address the Binding of Carboxylic Acid Ligands to CdSe Quantum Dots. *J. Am. Chem. Soc.* **2010**, *132* (29), 10195–10201. https://doi.org/10.1021/ja104351q.

(47) Ritchhart, A.; Cossairt, B. M. Quantifying Ligand Exchange on InP Using an Atomically Precise Cluster Platform. *Inorg. Chem.* **2019**, *58* (4), 2840–2847. https://doi.org/10.1021/acs.inorgchem.8b03524.

(48) Knauf, R. R.; Lennox, J. C.; Dempsey, J. L. Quantifying Ligand Exchange Reactions at CdSe Nanocrystal Surfaces. *Chem. Mater.* **2016**, *28* (13), 4762–4770. https://doi.org/10.1021/acs.chemmater.6b01827.

(49) Shulenberger, K. E.; Keller, H. R.; Pellows, L. M.; Brown, N. L.; Dukovic, G. Photocharging of Colloidal CdS Nanocrystals. *J. Phys. Chem. C* **2021**. https://doi.org/10.1021/acs.jpcc.1c06491.

(50) Zhu, H.; Song, N.; Lv, H.; Hill, C. L.; Lian, T. Near Unity Quantum Yield of Light-Driven Redox Mediator Reduction and Efficient H2 Generation Using Colloidal Nanorod Heterostructures. *J. Am. Chem. Soc.* **2012**, *134* (28), 11701–11708. https://doi.org/10.1021/ja303698e.

(51) Hamachi, L. S.; Jen-La Plante, I.; Coryell, A. C.; De Roo, J.; Owen, J. S. Kinetic Control over CdS Nanocrystal Nucleation Using a Library of Thiocarbonates, Thiocarbamates, and Thioureas. *Chem. Mater.* **2017**, *29* (20), 8711–8719. https://doi.org/10.1021/acs.chemmater.7b02861.

(52) Yu, W. W.; Qu, L.; Guo, W.; Peng, X. Experimental Determination of the Extinction Coefficient of CdTe, CdSe, and CdS Nanocrystals. *Chem. Mater.* **2003**, *15* (14), 2854–2860. https://doi.org/10.1021/cm034081k.

Chapter 4. Probing Ligand Binding on Nanocrystal Surfaces using Temperature-Dependent FTIR and Ultrafast IR Spectroscopy

Significant portions of the following chapter have previously been published.[1] The work in sections 4.2.2 and 4.2.3 was carried out by Megan D. Klein and Casey H. Bisted.

4.1 Introduction

In recent years, semiconductor nanocrystal (NC) materials have demonstrated their utility across a range of optoelectronic applications. The emissive properties of these NCs have proven advantageous in the areas of light emitting diodes and lasing,[2] while their absorptive behaviour has led to their use in luminescent solar concentrators and numerous other photovoltaic and photocatalytic applications.[3,4] In particular, the size tunability, narrow emission linewidths, strong absorption, and high quantum yield of NCs are desirable properties for numerous types of devices. Recent work has even begun investigating the potential for colloidally synthesised NCs to be utilised as photon sources in quantum information applications.[5] In order to ensure these materials can be utilised to their fullest extent, it is crucially important to have a fundamental understanding of the properties that dictate NC photophysics.

While the core of a NC determines many of its characteristic photophysical properties, these properties are often highly sensitive to disruption by defects at the surface of the NC. It has been shown that undercoordinated surface anions are a predominant cause of mid-band gap trap states that localise charges and dominate exciton recombination.[6,7] Due to this effect of surface anions, many NC syntheses are performed with an excess of cation precursors or post-synthetically modified to ensure a cation-rich surface.[8] In addition, capping ligands are typically incorporated

on the nanomaterial surface, playing a multifaceted role of passivating dangling surface bonds, ensuring charge balance, and promoting particle stability. Given the critical impact these ligands have on preserving NC properties, they are a subject of significant and continued study in the field.[9–13]

Numerous classes of both organic and inorganic ligands are used to functionalise NC surfaces. Organic ligands with long alkyl tails are a common example as they ensure surface passivation, prevent particle agglomeration, and enable NC suspension in organic solvents. These alkyl tails are frequently used in conjunction with carboxylate head groups, which act as X-type ligands: covalently bonding to surface cations while also ensuring charge balance at the nonstoichiometric surface.[9,14,15] Despite the covalent ligand–NC bond, the ligand shell has been shown to be dynamic with frequent self-exchange aided by solvent, excess ligand, or elevated temperatures.[16–18]

To probe the dynamic nature and energetics of NC-bound ligands, previous studies have often relied on ligand exchange reactions. By monitoring the displacement of one ligand species following the addition of a second, information can be obtained on the difference in free energies between the types of ligands.[19,20] While these experiments are indisputably valuable in understanding binding differences between ligand species, they are unable to give insights into differences between binding motifs of a single species. In the case of carboxylate-capped InP NCs, previous work by Gary et al. has shown that four different binding geometries can be observed via single-crystal X-ray diffraction, with a fifth monodentate geometry observed in NMR studies.[15,21] There is much motivation to understand differences in binding motifs since they may also affect the surface reactivity and kinetics of NC growth, ultimately impacting factors such as shape and size dispersity for high-quality NCs.[22,23] However, unlike ligand displacement reactions, there is

no easy handle by which to titrate between these binding motifs, making it very difficult to gain information about energetics between these configurations.

Several studies have used computational methods to calculate binding energies of ligand head groups on NC surfaces.[24–27] Work by Xie et al. calculated the relative energies involved in rearrangement of carboxylate ligands in clusters of indium acetate complexes and found values ranging from 0 to 3 kcal/mol for converting between chelating and bridging conformations, and around 15–20 kcal/mol for converting between chelating and monodentate.[28] However, both of these values were strongly dependent on the surrounding environment of In atoms and ligand molecules, and we would expect them to change drastically when going from an indium acetate cluster to the surface of an InP magic-sized cluster (MSC). A study by Zhang et al. looked to calculate the binding energy of carboxylate moieties on facets of CdSe NCs and found a significantly larger difference of 50–80 kcal/mol between chelating and bridging conformations.[29] In the limit of low ligand density, this relative energy difference decreased to 3 kcal/mol, which is much closer to the results calculated for the indium acetate clusters. While these computational results have generated some insight into the surface energetics of these binding motifs, there remains an urgent need for experimental measurements.

In this work, we present a temperature-dependent Fourier transform infrared (FTIR) spectroscopy method to study evolving populations of binding configurations for myristate-capped InP MSCs and extract relative energy differences between them. By utilising the variation in the asymmetric COO^- stretching frequencies between binding motifs, we globally fit the series of spectra to a set of five Gaussian peaks across all temperatures via a Markov chain Monte Carlo (MCMC) process. We then used the changes in peak areas to find the relative energy differences between the binding configurations of carboxylate groups, as well as the free carboxylic acid

species. From these results, we observe that the energetic separation between a monodentate ligand and a free ligand is approximately equal to the vibrational stretching frequency of the carboxylate group. This strongly suggests a connection between vibrational excitation of the ligand and its dissociation from the surface. Additionally, we observe that the difference between bidentate and monodentate can be far smaller, and for some bidentate configurations, the additional bond may not provide any increased stability at all. This experimental approach enables measuring energy differences between binding motifs, offers unique insight into NC surface energetics, and further suggests that the ligand shell may be even more dynamic than previously thought.

4.2 InP Magic-Sized Clusters

4.2.1 *Temperature dependent FTIR*

To study the energetics of carboxylate ligand binding modes on nanocrystal surfaces, we used InP MSCs as our model system – their atomic precision allows for more rigorous analysis than their larger, more heterogeneous QD counterparts. InP MSCs were previously crystallised with phenylacetate ligands, and the crystal structure showed that the cluster consists of a charged non-stoichiometric core $[In_{21}P_{20}]^{3+}$, with a cation rich surface of 16 extra indium atoms coordinated to 51 phenylacetate ligands, resulting in an overall stoichiometry of $In_{37}P_{20}(O_2CR)_{51}$.[21] The crystal structure also showed a distribution of carboxylate coordination modes – of the 51 ligands, 12 were chelating (24%), 33 were asymmetric (syn-anti) bridging (65%), 5 were symmetric (syn-syn) bridging (10%), and 1 was bidentate + dative (2%).

In solution, the ligand shell of InP MSCs becomes more dynamic and labile. Using FTIR spectroscopy, the carboxylate stretching region can be monitored to identify carboxylate binding motifs. Previous work on oleate-capped InP MSCs also identified four binding populations – 22%

chelating, 45% syn–anti bridging, 16% syn–syn bridging, and 17% monodentate.[30] The shift in populations from syn-anti bridging to monodentate as we go from solid to liquid phase illustrates the increase in mobility of the ligands. The bidentate/dative mode seen in the crystal structure was not assigned in solution by FTIR. Likewise, the monodentate motif was not observed in the crystal structure.

In this work, we used InP clusters capped with myristate ligands. Myristic acid has a shorter alkyl chain compared to oleic acid and no double bond, which allows us to probe whether slight perturbations in the sterics of the ligand shell have an effect on the carboxylate binding populations. We collected temperature-dependent FTIR spectra of the clusters from 25 °C to 100 °C (Figure 4.2). As seen previously, each binding conformation results in a symmetric and asymmetric carboxylate stretching vibration. The CH_2 bending mode from the alkyl tail overlaps the symmetric region, so our analysis is focused on the asymmetric region.

We assigned a fifth population of dative (L-type) binding, centred at 1608 cm^{-1}. This dative motif is difficult to assign to an exact geometry, but studies on ruthenium dimer complexes with carboxylic acid ligands have shown similar stretching frequencies for datively bound carboxylic acids that formed hydrogen bonds to neighbouring carboxylates.[31] The vibrational energy we observe for this dative binding conformation also agrees with general understanding on the decreased stability of dative L-type binding compared to covalent X-type binding on a cationic surface. This peak was also observed in the FTIR of oleate-capped clusters but not assigned at the time. Overall, from lowest to highest frequency, the order of the binding modes is found to be chelating < syn–anti < syn–syn < monodentate < dative.

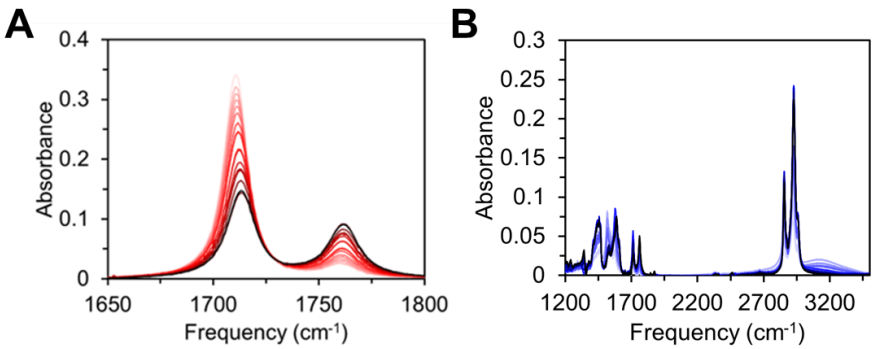

Figure 4.1. Temperature dependent FTIR spectra of (A) myristic acid and (B) indium myristate.

Lastly, in addition to bound carboxylate peaks from 1400 to 1600 cm^{-1}, we have assigned the peaks at 1710 and 1760 cm^{-1} as the C=O stretch of H-bonded dimer and monomer respectively of unbound, protonated myristic acid $CH_3(CH_2)_{12}COOH$.[32] We confirmed these assignments via temperature-dependent FTIR of myristic acid (Figure 4.1). As we increase the temperature, we see a clear isosbestic point between the two species and a shift from dimer to monomer, which is consistent with increasing the energy of the system and breaking apart dimer species. The peaks are also present in complexed indium myristate $In(myr)_3$, along with adventitious water molecules as evidenced by the increased absorption of the O-H stretch. These peaks can offer valuable insights on surface binding equilibrium.

At 25 °C, we fit the asymmetric stretching region of the FTIR spectrum to five Gaussians corresponding to the five binding modes discussed previously (Figure 4.2). We note the absence of any unbound myristic acid or $In(myr)_3$ at this temperature. We find the distribution of populations to be 19% chelating, 25% syn-anti bridging, 21% syn-syn bridging, 27% monodentate, and 7% dative. Comparing to the oleate-capped InP clusters (and not considering the dative population), we observe an even more pronounced shift of the binding modes from syn-anti bridging to monodentate. This demonstrates that even a small change in the ligand sterics can lead

to a significant change in how the ligands bind to the surface. It is possible that ligand surface coverage is different from the 51 ligands measured via single-crystal diffraction. Myristic acid is more crystalline and less bulky than oleic acid – if more myristic acids can fit on the surface of the cluster, that can lead to a preference for monodentate binding in order to accommodate all the ligands.

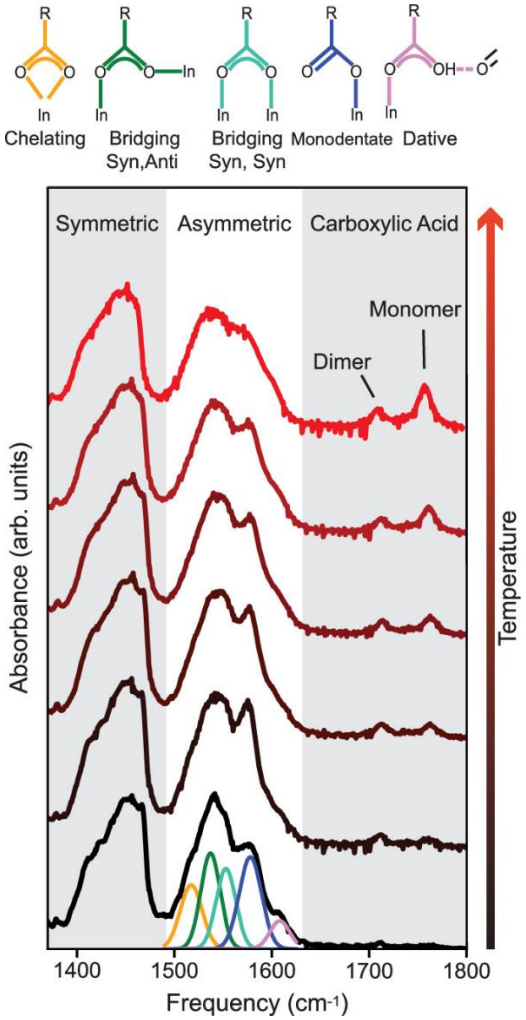

Figure 4.2. Representative FTIR spectra from the temperature-dependent measurement of myristate-capped InP MSCs spanning from 25 °C (bottom) to 100 °C (top) in increments of 15 °C, demonstrating changes that occur with increasing temperature along with peak assignment of the asymmetric carboxylate stretching region. From left to right, binding groups shown include chelating (yellow), bridging syn–anti (green), bridging syn–syn (light blue), monodentate (dark blue), and dative (pink).

While at lower temperatures there is sufficient resolution of the peaks for the spectra to be fit to five Gaussians, at higher temperatures, peak broadening increases uncertainty of typical fitting algorithms and the spectra cannot be accurately fit. This broadening could be explained in part by the work of Friedfeld et al.[33] who observed by ^{13}C NMR that heating InP clusters up to 80 °C resulted in broadening and coalescence of carboxylate resonances, indicating intraparticle ligand exchange. Differential scanning calorimetry data also showed a small endothermic event at 66 °C attributed to the same ligand rearrangement, and a strong endothermic change at 115–130 °C attributed to crystal melting.

As the crystal nears the melting temperature at the high end of our temperature range, we would expect higher phonon occupancy and increased geometric disorder that would lead to vibrational linewidth broadening like we observe. Lastly, as we heat the clusters, the populations of unbound acid monomer and dimer also increase, indicating that not only is there intraparticle ligand exchange, but also that ligands are becoming completely unbound from the surface. As such, a more rigorous method is needed to perform a global fitting and analyse the full temperature FTIR series concurrently.

4.2.2 *Markov chain Monte Carlo Global Fitting*

Extracting quantitative information from complicated spectra often necessitates peak fitting to determine the frequency, width, and amplitude of each component in the spectra. For a single spectrum consisting of only a few peaks, this is relatively straightforward to do with a simple nonlinear least squares algorithm. In cases where a series of spectra are measured, and certain parameters are not expected to vary across the series, a global fit across the whole series can be performed at the cost of significantly increased complexity. To perform a global fit on the

temperature-dependent FTIR spectra, we utilised a Bayesian approach with an MCMC algorithm to sample the parameter space and fit the spectra to a sum of five peaks across all temperatures.

Briefly, the use of a Monte Carlo approach allows stochastic sampling of the parameter space, rather than relying on gradient-based methods, which may get stuck in local minima.[34] Meanwhile, the use of a constructed Markov chain satisfying ergodicity and detailed balance ensures the existence of a single stable solution. To quantify how likely a specific set of parameters is, we turn to Bayes' theorem to calculate the posterior probability for a particular stochastically sampled fit (equation 1)

$$P(\theta|x) = \frac{\mathrm{P}(\theta)\times\mathrm{P}(\mathrm{x}|\theta)}{\int \mathrm{P}(\theta)\times\mathrm{P}(\mathrm{x}|\theta)\mathrm{d}\theta} \quad \text{(eq. 1)}$$

where the posterior probability $\mathrm{P}(x)$, represents the probability that a set of parameters θ, are correct given the observed data x. This is proportional to the product of the prior probability $\mathrm{P}(\theta)$, which describes the chance of a particular set of parameters occurring using some prior knowledge of the system, multiplied with the likelihood $\mathrm{P}(\mathrm{x}|\theta)$, which describes the probability of observing the data given a specific value for the parameters. This product is then normalised to give a probability distribution that integrates to one across the space. Because we are only concerned with finding the maximum posterior probability, we only need to utilise relative changes in probability and can therefore neglect the computationally expensive integral.

To fit the FTIR spectra reported here, we constructed a model consisting of five Gaussian peaks, each with a mean frequency μ_i and a room-temperature width of σ_i. While we assume that the mean vibrational frequencies will not change significantly over the temperature range we probe, as mentioned above, some broadening is observed at elevated temperatures. The exact form of this broadening is too complex to readily model, as it would require a detailed knowledge of the

phonon density of states as well as the nature of how the phonon modes affect the ligand binding geometry. Furthermore, trying to account for those behaviours in detail would result in a vastly overparameterised fit. As such, we rely on a simplified power law broadening term that captures the general behaviour of the sum width, with each peak following the same broadening parameter β. The σ_i parameters are treated as constants across temperatures, and the width of peak *i* is then given by $\sigma_i(\frac{T}{T_0})^{\beta}$, with T_0 taken to be 298 K. The full equation for the fit is therefore as follows in equation 2, where $\tilde{\nu}$ represents the frequency and $c_i(T)$ is the temperature-dependent amplitude for peak *i*, as discussed in more detail below.

$$f(\tilde{\nu},T) = \sum_{i=1}^{5} c_i(T)\, e^{(-(\tilde{\nu}-\mu_i)^2/(2\sigma_i^2(T/T_0)^{2\beta}))} \quad \text{(eq. 2)}$$

With the basis of our fit established, we determined appropriate prior distributions through nonlinear least squares fit of the initial room temperature spectrum (Figure 4.2). The MCMC scheme is depicted in Figure 4.3 (a). An ensemble of Monte Carlo walkers is distributed in parameter space, and in each MCMC iteration, a subset of the walkers is selected and random moves are generated to new proposed positions. The spectral peaks corresponding to these proposed parameters are then constructed, and the temperature-dependent amplitudes are determined by least squares fitting at each temperature point. The fit residuals are evaluated and used to estimate the likelihood function of the parameters. Based on the resulting posterior probability, the moves are then stochastically accepted or rejected and the ensemble positions are updated accordingly. The algorithm iterates through the remaining subsets of walkers and then repeats the process until a preset number of steps have been evaluated. The results of this global fitting process are shown in Figure 4.3 (b), where the data is shown in orange and the average fits

are shown by the blue lines with standard deviations at each point given by the shaded blue region. Because we expect the best fit to occur at the maximum posterior probability, we performed statistical analyses on the set of 15,000 sampled points with the highest posterior probabilities. The obtained parameters and their associated uncertainties are shown in Table 4.1. We note that for our room temperature spectrum, these values agree closely with those found previously for oleate-capped InP clusters.[30,32]

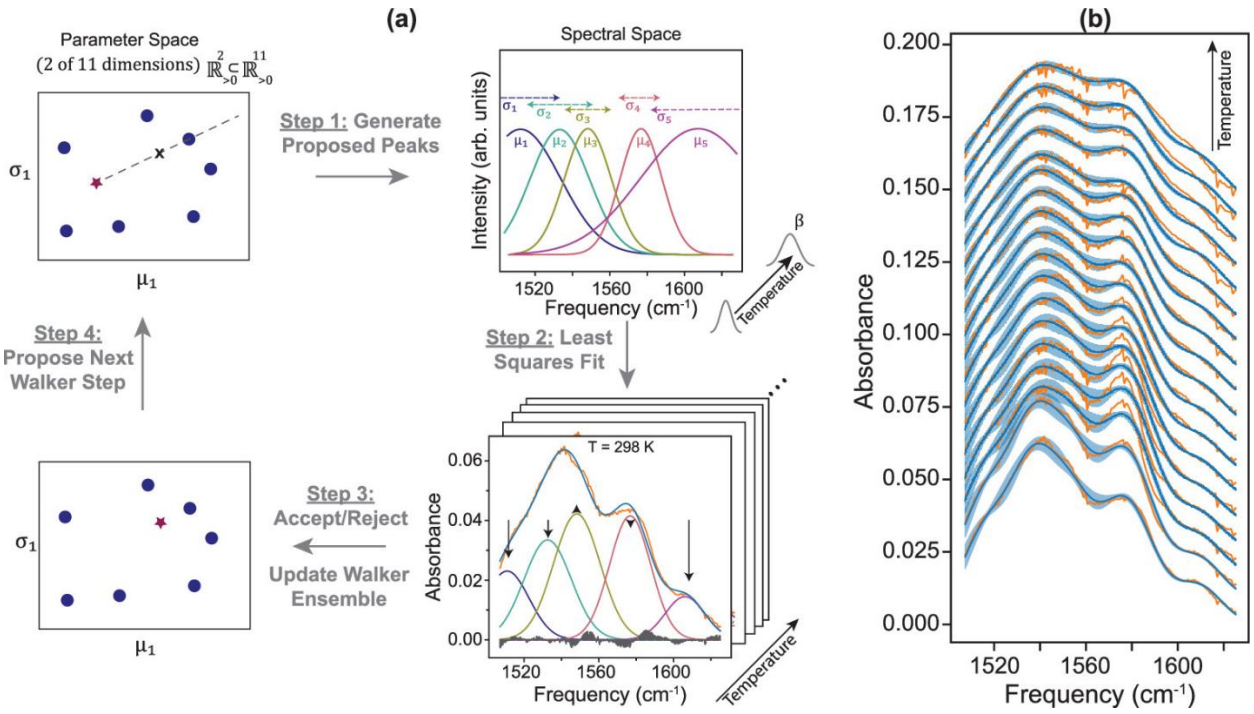

Figure 4.3. (a) Depiction of the MCMC global fit process. For a given subset of walkers, stretch moves are randomly generated to propose new positions in parameter space. These new walker positions are used to generate the Gaussian peaks corresponding to those parameters of means μ_i and widths σ_i, with a temperature-dependent broadening factor β. These peaks are then fit by least squares to the measured FTIR spectra at each temperature point. The log likelihood of this fit is taken as the negative sum of squared residuals; combined with the prior probabilities of the parameters, the resulting posterior probability is used to stochastically decide whether to accept or reject the new walker positions. The walker ensemble is then updated, and the algorithm iterates to the next subset of walkers and repeats the process. (b) Global MCMC fit results (blue lines) for the temperature-dependent InP MSC FTIR spectra (orange lines). The standard deviation across the top 15,000 fits is depicted by the blue shaded area.

Table 4.1. Extracted parameters from the MCMC global fit on a temperature series of FTIR spectra from an InP MSC sample.

μ	1515.0 ± 2.1	1537.1 ± 1.3	1553.9 ± 1.9	1577.0 ± 0.28	1609.0 ± 0.28
σ	10.8 ± 1.0	11.2 ± 1.9	9.1 ± 0.8	12.2 ± 0.27	10.0 ± 0.18
β	0.62 ± 0.10				

4.2.3 *Interpretation of Fitted FTIR Parameters*

From the global fitting results, we can extract amplitude information without needing to enforce any assumptions on the temperature-dependent behaviour of the underlying populations. This allows a more unbiased approach to see how binding motif populations change with temperature. In particular, we can look at the differences of the logs of peak areas to determine whether these populations follow a Boltzmann distribution at any point. This is shown in Figure 4.4 (a) as the log area difference with respect to the monodentate binding mode peak, plotted against inverse thermal energy. Above 40 °C (to the left of the black dashed line in the figure), we observe a linear trend to the log area differences, suggesting that a Boltzmann distribution accurately describes the population, as shown in equation 3. The change in behaviour at 40 °C suggests that once there is sufficient thermal energy, the system can fully equilibrate between various binding motifs and dissociated free ligand.

We proceeded to perform linear regressions on the temperature-dependent log area differences in the high-temperature regime. Taking the data above 40 °C for the fits corresponding to the top 15,000 posterior probabilities sampled by the model, we found the averages and standard deviations of the slopes obtained from those regressions. These values are plotted in Figure 4.4 (b). Through application of the Boltzmann equation, we see that the resulting slopes correspond to the relative energy differences between these binding motifs with respect to the monodentate motif, shown by equation 3,

$$\ln(A_{\text{mono}}) - \ln(A_i) = \ln(\alpha e^{\Delta\varepsilon/k_B T}) = \ln(\alpha) + \Delta\varepsilon\frac{1}{k_B T} \quad \text{(eq. 3)}$$

where A_i denotes the peak area of component i, $\Delta\varepsilon = \varepsilon_i - \varepsilon_{\text{mono}}$ is the change in energy between the two motifs, T is the temperature, k_B is the Boltzmann constant, and α is a proportionality constant.

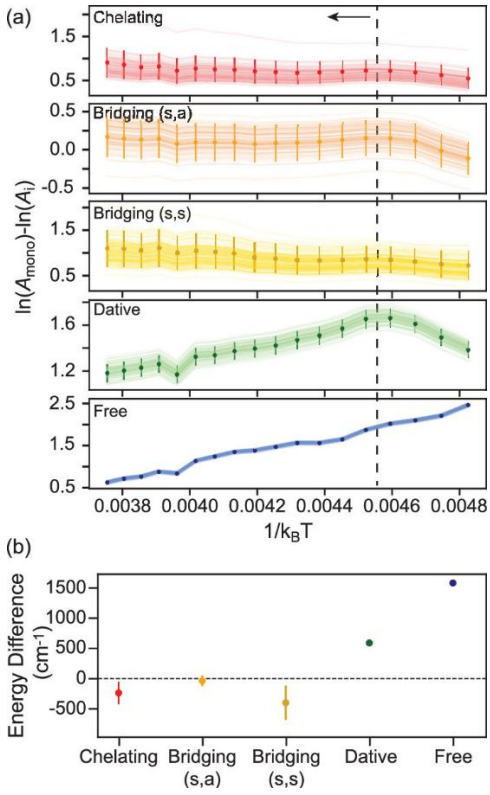

Figure 4.4. (a) Differences of the log of peak areas with respect to the monodentate binding motif, plotted against inverse thermal energy with units of inverse wavenumbers. Markers and error bars represent mean and standard deviation at each temperature point across sampled global fits comprising the top 15,000 posterior probabilities. Lighter lines depict log area differences from the fits corresponding to the 100 highest posterior probabilities. Note the highly correlated error between temperature points, which is not conveyed from the error bars alone. While log area differences might vary in magnitude between fits, the temperature trends stay rather consistent. Arrow denotes data points above 40 °C (black dashed line), which demonstrate near linear behavior and were fit using linear regression. (b) Extracted slopes from linear regressions of the 45–110 °C regime in (a). These values correspond to energy differences relative to the monodentate binding motif, assuming an equilibrated system following Boltzmann statistics. Markers and error bars respectively denote mean and standard deviation of slopes taken from sampled global fits comprising the top 15,000 posterior probabilities.

From Figure 4.4 (b), we can clearly see a varied energy landscape between different binding conformations. While the chelating and syn–syn bridging conformations are lower in energy compared to the monodentate motif, the difference is not as large as might be expected from the formation of an additional ligand–metal bond. The energy difference we observe is on the order of 200–400 cm^{-1}, or 0.57–1.14 kcal/mol, far lower than the 15–20 kcal/mol predicted by theory.[28,29] Notably, the syn–anti bridging conformation is not significantly different in energy from the monodentate motif, suggesting that the energetic bonus of an additional ligand–metal bond is offset by a confounding factor, such as geometric strain.[35,36]

Meanwhile, the dative binding conformation we observe has a higher energy relative to the monodentate. As L-type ligands do not contribute to charge balance on the surface, we would expect them to be able to convert or dissociate more readily like we see here. Finally, we observed a relative energy difference of 1582 ± 19 cm^{-1}, around 4.5 kcal/mol, between the monodentate binding motif and the free ligand. This is of particular note, as this energy is not significantly different from the vibrational frequency we extract for the monodentate asymmetric stretching mode, 1577.0 ± 0.28 cm^{-1}. These results are also summarised in Table 4.2.

Table 4.2. Summary of relative binding energies extracted from slopes of temperature-dependent log area differences.

Binding motif	**Relative energy (w.r.t. monodentate)**
chelating	–236 ± 120 cm^{-1}
bridging (s,a)	–35 ± 57 cm^{-1}
bridging (s,s)	–400 ± 184 cm^{-1}
dative	591 ± 34 cm^{-1}
free ligand	1582 ± 19 cm^{-1}

While these energies do not provide information on the activation barriers between these conformations, they do inform on the relative stability of binding motifs compared to one another. These results suggest that the excitation of this vibrational stretching mode is enough to offset the energy loss associated with ligand dissociation. This is critically relevant for semiconductor NCs where numerous processes, including thermalisation to the band edge and Auger–Meitner recombination of trions or multiexcitons, result in energy loss as phonon emission.[37,38] This heat could easily dissipate through the ligand shell, resulting in dissociation of the binding group, an increase in adsorption sites for substrate molecules, and an increase in photocatalytic performance, as demonstrated in Chapter 3.

MSCs are metastable, kinetic products with high energy surfaces that can grow into larger clusters or quantum dots.[33,39,40] Large quantum dots are the thermodynamic product because as size increases, QD surface energies decrease, as illustrated by Ostwald ripening mechanisms.[41,42] Compared to MSCs, we would expect different ligand binding motifs to be more stable and the energy difference between bound and unbound ligand populations to be larger on the surface of QDs. We would also expect a broader distribution of binding populations given sample polydispersity. However, as we move toward atomic precision in QD synthesis using techniques such as colloidal atomic layer deposition (c-ALD),[43] we should be able to adopt the methods in this study to larger QD systems and precisely calculate the energies of different binding modes.

4.3 CONCLUSIONS

In this work, we have demonstrated that a temperature series of vibrational spectra can be used to measure relative energies of carboxylate binding conformations on the surface of InP MSCs. An MCMC process can be used to optimise a global fit across all spectra and estimate fit

uncertainty. We further show that the relative energies between these binding motifs is much lower than previously thought. A ligand with one bond to the surface is not significantly different in energy from a bidentate ligand bridging two In atoms in a syn–anti geometry. Last, we demonstrate that the energy difference between a monodentate binding motif and a free ligand is equal to the energy of the monodentate carboxylate asymmetric stretching mode. This suggests that the ligand-functionalised surface of an NC is far more dynamic and labile than previously thought and that ligand vibrational excitation has the potential to impact surface coverage.

4.4 EXPERIMENTAL

4.4.1 *InP MSC Synthesis and Characterisation*

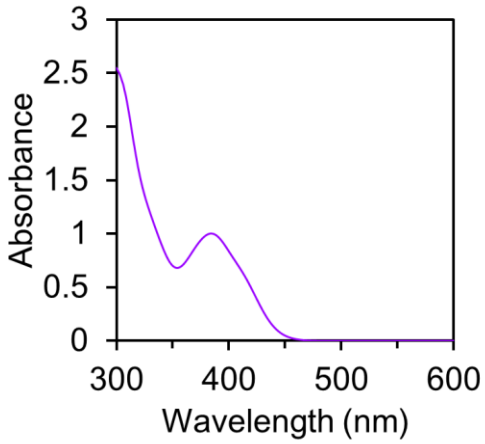

Figure 4.5. UV-vis absorption of InP MSC after purification.

All glassware was dried in a 160 °C oven overnight prior to use. InP MSCs were prepared following a previously reported procedure.[21] A 100 mL three-neck round-bottom flask was loaded with 0.936 g of indium acetate (3.2 mmol, 1 eq) and 2.66 g of myristic acid (11.5 mmol, 3.6 eq) and heated at 105 °C overnight with stirring under vacuum to pull off acetic acid as a byproduct. The resulting indium myristate complex was then dissolved in 20 mL of anhydrous toluene under

nitrogen. In a nitrogen-filled glovebox, 500 μL of $P(SiMe_3)_3$ (1.72 mmol, 0.54 eq) was added to 10 mL of anhydrous toluene and the solution transferred to a syringe. The contents were rapidly injected into the reaction flask. The reaction then proceeded at 105 °C until no further changes were observed by UV–vis (Cary Agilent 5000), about 50 min. The MSCs were then cooled and the toluene removed by vacuum distillation. The clusters were brought into the glovebox and redissolved in toluene and precipitated with acetonitrile. This was repeated for a minimum of three rounds of precipitation. One final spin was done in toluene alone to remove any undissolved species. The clusters were purified by size exclusion chromatography over 40-80 μm Bio-Beads S-X1 Support from Bio-Rad and stored dry as a waxy solid.

4.4.2 *FTIR Measurements*

FTIR measurements were conducted in a Jasco 4100 FTIR spectrophotometer under a positive pressure of N_2. An 8 mg/mL solution of MSCs was flowed through a liquid cell with a 300 μm Teflon spacer. Heated measurements were conducted with a temperature-controlled demountable liquid cell (Harrick) paired with a Peltier heater at 1 °C/min. The sample was left to equilibrate for 10 min at each temperature point. Flowing was stopped when recording spectra and then resumed to ensure thermal equilibrium.

4.4.3 *MCMC Sampling*

A homebuilt sampling algorithm was constructed in Python 3.8 following the parallelisable walker update scheme laid out by Foreman-Mackey et al.[45] Affine invariant sampling was used in the form of the stretch move described by Goodman and Weare.[46] A prior distribution was constructed based off a room temperature fit of the InP MSC FTIR spectrum, with standard

deviations equal to those of the fit parameters. Following a proposed step, the predicted spectrum was generated by least squares fitting the amplitude of the five Gaussian peaks, corresponding to the proposed point in parameter space, to the FTIR spectrum at each temperature point. The log likelihood was then calculated as the negative sum of squared residuals. In order to ensure that the assumption of normally distributed error was met, the fits and data were converted to transmission prior to calculating the residuals. Chains were thinned down to every 10 steps, and runs were typically performed with 200 walkers and a total of ~300,000 proposed moves. The acceptance proportion was kept between 0.2 and 0.4 by adjusting the step size of the stretch move prior to a run if needed. The elliptical distributions of all of the peak parameter correlations demonstrate adequate parameterisation of the model. Additionally, the results with the given prior distribution were validated by performing the MCMC global fitting again using wider prior distributions, as well as once more with uninformed priors. Importantly, while we observe an increase in the uncertainty moving to wider and then uninformed prior distributions, we do not see a significant change in the extracted parameters or relative energies.

4.5 REFERENCES

(1) Klein, M. D.; Bisted, C. H.; Dou, F. Y.; Sandwisch, J. W.; Cossairt, B. M.; Khalil, M. Measuring Relative Energies of Ligand Binding Conformations on Nanocluster Surfaces with Temperature-Dependent FTIR Spectroscopy. *J. Phys. Chem. C* **2023**, *127* (34), 16970–16978. https://doi.org/10.1021/acs.jpcc.3c03951.

(2) Nguyen, H. A.; Dixon, G.; Dou, F. Y.; Gallagher, S.; Gibbs, S.; Ladd, D. M.; Marino, E.; Ondry, J. C.; Shanahan, J. P.; Vasileiadou, E. S.; Barlow, S.; Gamelin, D. R.; Ginger, D. S.; Jonas, D. M.; Kanatzidis, M. G.; Marder, S. R.; Morton, D.; Murray, C. B.; Owen, J. S.; Talapin, D. V.; Toney, M. F.; Cossairt, B. M. Design Rules for Obtaining Narrow Luminescence from Semiconductors Made in Solution. *Chem. Rev.* **2023**, *123* (12), 7890–7952. https://doi.org/10.1021/acs.chemrev.3c00097.

(3) Coropceanu, I.; Bawendi, M. G. Core/Shell Quantum Dot Based Luminescent Solar Concentrators with Reduced Reabsorption and Enhanced Efficiency. *Nano Lett.* **2014**, *14* (7), 4097–4101. https://doi.org/10.1021/nl501627e.

(4) Yuan, Y.; Jin, N.; Saghy, P.; Dube, L.; Zhu, H.; Chen, O. Quantum Dot Photocatalysts for Organic Transformations. *J. Phys. Chem. Lett.* **2021**, *12* (30), 7180–7193. https://doi.org/10.1021/acs.jpclett.1c01717.

(5) Nguyen, H. A.; Sharp, D.; Fröch, J. E.; Cai, Y.-Y.; Wu, S.; Monahan, M.; Munley, C.; Manna, A.; Majumdar, A.; Kagan, C. R.; Cossairt, B. M. Deterministic Quantum Light Arrays from Giant Silica-Shelled Quantum Dots. *ACS Appl. Mater. Interfaces* **2023**, *15* (3), 4294–4302. https://doi.org/10.1021/acsami.2c18475.

(6) Houtepen, A. J.; Hens, Z.; Owen, J. S.; Infante, I. On the Origin of Surface Traps in Colloidal II–VI Semiconductor Nanocrystals. *Chem. Mater.* **2017**, *29* (2), 752–761. https://doi.org/10.1021/acs.chemmater.6b04648.

(7) Hughes, K. E.; Stein, J. L.; Friedfeld, M. R.; Cossairt, B. M.; Gamelin, D. R. Effects of Surface Chemistry on the Photophysics of Colloidal InP Nanocrystals. *ACS Nano* **2019**, *13* (12), 14198–14207. https://doi.org/10.1021/acsnano.9b07027.

(8) Stein, J. L.; Mader, E. A.; Cossairt, B. M. Luminescent InP Quantum Dots with Tunable Emission by Post-Synthetic Modification with Lewis Acids. *J. Phys. Chem. Lett.* **2016**, *7* (7), 1315–1320. https://doi.org/10.1021/acs.jpclett.6b00177.

(9) Owen, J. The Coordination Chemistry of Nanocrystal Surfaces. *Science* **2015**, *347* (6222), 615–616. https://doi.org/10.1126/science.1259924.

(10) De Roo, J. The Surface Chemistry of Colloidal Nanocrystals Capped by Organic Ligands. *Chem. Mater.* **2023**, *35* (10), 3781–3792. https://doi.org/10.1021/acs.chemmater.3c00638.

(11) Hens, Z. Ligands on Nanocrystal Surfaces, the 1H Nuclear Magnetic Resonance Fingerprint. *Acc. Chem. Res.* **2023**. https://doi.org/10.1021/acs.accounts.3c00170.

(12) Chakraborty, I. N.; Roy, P.; Rao, A.; Devatha, G.; Roy, S.; Pillai, P. P. The Unconventional Role of Surface Ligands in Dictating the Light Harvesting Properties of Quantum Dots. *J. Mater. Chem. A* **2021**, *9* (12), 7422–7457. https://doi.org/10.1039/D0TA12623C.

(13) Chen, Y.; Yu, S.; Fan, X.-B.; Wu, L.-Z.; Zhou, Y. Mechanistic Insights into the Influence of Surface Ligands on Quantum Dots for Photocatalysis. *J. Mater. Chem. A* **2023**. https://doi.org/10.1039/D2TA09293J.

(14) Anderson, N. C.; Hendricks, M. P.; Choi, J. J.; Owen, J. S. Ligand Exchange and the Stoichiometry of Metal Chalcogenide Nanocrystals: Spectroscopic Observation of Facile Metal-

Carboxylate Displacement and Binding. *J. Am. Chem. Soc.* **2013**, *135* (49), 18536–18548. https://doi.org/10.1021/ja4086758.

(15) Ritchhart, A.; Cossairt, B. M. Quantifying Ligand Exchange on InP Using an Atomically Precise Cluster Platform. *Inorg. Chem.* **2019**, *58* (4), 2840–2847. https://doi.org/10.1021/acs.inorgchem.8b03524.

(16) Calvin, J. J.; Ben-Moshe, A.; Curling, E. B.; Brewer, A. S.; Sedlak, A. B.; Kaufman, T. M.; Alivisatos, A. P. Thermodynamics of the Adsorption of Cadmium Oleate to Cadmium Sulfide Quantum Dots and Implications of a Dynamic Ligand Shell. *J. Phys. Chem. C* **2022**, *126* (30), 12958–12971. https://doi.org/10.1021/acs.jpcc.2c04223.

(17) Aruda, K. O.; Bohlmann Kunz, M.; Tagliazucchi, M.; Weiss, E. A. Temperature-Dependent Permeability of the Ligand Shell of PbS Quantum Dots Probed by Electron Transfer to Benzoquinone. *J. Phys. Chem. Lett.* **2015**, *6* (14), 2841–2846. https://doi.org/10.1021/acs.jpclett.5b01256.

(18) Kessler, M. L.; Kelm, J. E.; Starr, H. E.; Cook, E. N.; Miller, J. D.; Rivera, N. A.; Hsu-Kim, H.; Dempsey, J. L. Unraveling Changes to PbS Nanocrystal Surfaces Induced by Thiols. *Chem. Mater.* **2022**, *34* (4), 1710–1721. https://doi.org/10.1021/acs.chemmater.1c03888.

(19) Calvin, J. J.; O'Brien, E. A.; Sedlak, A. B.; Balan, A. D.; Alivisatos, A. P. Thermodynamics of Composition Dependent Ligand Exchange on the Surfaces of Colloidal Indium Phosphide Quantum Dots. *ACS Nano* **2021**, *15* (1), 1407–1420. https://doi.org/10.1021/acsnano.0c08683.

(20) Elimelech, O.; Aviv, O.; Oded, M.; Banin, U. A Tale of Tails: Thermodynamics of CdSe Nanocrystal Surface Ligand Exchange. *Nano Lett.* **2020**, *20* (9), 6396–6403. https://doi.org/10.1021/acs.nanolett.0c01913.

(21) Gary, D. C.; Flowers, S. E.; Kaminsky, W.; Petrone, A.; Li, X.; Cossairt, B. M. Single-Crystal and Electronic Structure of a 1.3 Nm Indium Phosphide Nanocluster. *J. Am. Chem. Soc.* **2016**, *138* (5), 1510–1513. https://doi.org/10.1021/jacs.5b13214.

(22) Sandeno, S.; Schnitzenbaumer, K.; Krajewski, S.; Beck, R.; Ladd, D.; Levine, K.; Dayton, D.; Toney, M.; Li, X.; Kaminsky, W.; Cossairt, B. *Ligand Steric Profile Tunes the Reactivity of Indium Phosphide Clusters*; preprint; Chemistry, 2023. https://doi.org/10.26434/chemrxiv-2023-555vg.

(23) Zhao, Q.; Kulik, H. J. Electronic Structure Origins of Surface-Dependent Growth in III–V Quantum Dots. *Chem. Mater.* **2018**, *30* (20), 7154–7165. https://doi.org/10.1021/acs.chemmater.8b03125.

(24) Nguyen, K. A.; Pachter, R.; Day, P. N. Systematic Study of the Properties of CdS Clusters with Carboxylate Ligands Using a Deep Neural Network Potential Developed with Data from

Density Functional Theory Calculations. *J. Phys. Chem. A* **2020**, *124* (50), 10472–10481. https://doi.org/10.1021/acs.jpca.0c06965.

(25) Bealing, C. R.; Baumgardner, W. J.; Choi, J. J.; Hanrath, T.; Hennig, R. G. Predicting Nanocrystal Shape through Consideration of Surface-Ligand Interactions. *ACS Nano* **2012**, *6* (3), 2118–2127. https://doi.org/10.1021/nn3000466.

(26) Rempel, J. Y.; Trout, B. L.; Bawendi, M. G.; Jensen, K. F. Density Functional Theory Study of Ligand Binding on CdSe (0001), (000$\bar{1}$), and (11$\bar{2}$0) Single Crystal Relaxed and Reconstructed Surfaces: Implications for Nanocrystalline Growth. *J. Phys. Chem. B* **2006**, *110* (36), 18007–18016. https://doi.org/10.1021/jp064051f.

(27) Puzder, A.; Williamson, A. J.; Zaitseva, N.; Galli, G.; Manna, L.; Alivisatos, A. P. The Effect of Organic Ligand Binding on the Growth of CdSe Nanoparticles Probed by Ab Initio Calculations. *Nano Lett.* **2004**, *4* (12), 2361–2365. https://doi.org/10.1021/nl0485861.

(28) Xie, L.; Zhao, Q.; Jensen, K. F.; Kulik, H. J. Direct Observation of Early-Stage Quantum Dot Growth Mechanisms with High-Temperature Ab Initio Molecular Dynamics. *J. Phys. Chem. C* **2016**, *120* (4), 2472–2483. https://doi.org/10.1021/acs.jpcc.5b12091.

(29) Zhang, J.; Zhang, H.; Cao, W.; Pang, Z.; Li, J.; Shu, Y.; Zhu, C.; Kong, X.; Wang, L.; Peng, X. Identification of Facet-Dependent Coordination Structures of Carboxylate Ligands on CdSe Nanocrystals. *J. Am. Chem. Soc.* **2019**, *141* (39), 15675–15683. https://doi.org/10.1021/jacs.9b07836.

(30) Leger, J. D.; Friedfeld, M. R.; Beck, R. A.; Gaynor, J. D.; Petrone, A.; Li, X.; Cossairt, B. M.; Khalil, M. Carboxylate Anchors Act as Exciton Reporters in 1.3 Nm Indium Phosphide Nanoclusters. *J. Phys. Chem. Lett.* **2019**, *10* (8), 1833–1839. https://doi.org/10.1021/acs.jpclett.9b00602.

(31) Rotem, M.; Goldberg, I.; Shmueli, U.; Shvo, Y. Chemistry of Bridged Carboxylate Ruthenium Complexes. Crystal Structures of [Ru(PhCOO)(CO)2(PhCOOH]2, [Ru(4-FC6H4COO)2(CO)5(H2O)]2·0.5 C6H6, and [Ru2(s-BuCO2)2(CO)4(s-BuCO2H)]2. *Journal of Organometallic Chemistry* **1986**, *314* (1), 185–212. https://doi.org/10.1016/0022-328X(86)80363-1.

(32) Taheri, P.; Wielant, J.; Hauffman, T.; Flores, J. R.; Hannour, F.; de Wit, J. H. W.; Mol, J. M. C.; Terryn, H. A Comparison of the Interfacial Bonding Properties of Carboxylic Acid Functional Groups on Zinc and Iron Substrates. *Electrochimica Acta* **2011**, *56* (4), 1904–1911. https://doi.org/10.1016/j.electacta.2010.10.079.

(33) Friedfeld, M. R.; Johnson, D. A.; Cossairt, B. M. Conversion of InP Clusters to Quantum Dots. *Inorg. Chem.* **2019**, *58* (1), 803–810. https://doi.org/10.1021/acs.inorgchem.8b02945.

(34) Ashner, M. N.; Winslow, S. W.; Swan, J. W.; Tisdale, W. A. Markov Chain Monte Carlo Sampling for Target Analysis of Transient Absorption Spectra. *J. Phys. Chem. A* **2019**, *123* (17), 3893–3902. https://doi.org/10.1021/acs.jpca.9b00873.

(35) Su, E.; Guven, A.; Kani, I. Oxygen Bridged Homobinuclear Mn(II) Compounds with Anthranilic Acid: Theoretical Calculations, Oxidation and Catalase Activity. *Applied Organometallic Chemistry* **2018**, *32* (2), e4105. https://doi.org/10.1002/aoc.4105.

(36) Hemmert, C.; Verelst, M.; Tuchagues, J.-P. Pentadentate Dinucleating Ligands Affording Bis(μ-Carboxylato-O,O′)Diiron(II) Complexes. *Chem. Commun.* **1996**, No. 5, 617–618. https://doi.org/10.1039/CC9960000617.

(37) Guyot-Sionnest, P.; Shim, M.; Matranga, C.; Hines, M. Intraband Relaxation in CdSe Quantum Dots. *Phys. Rev. B* **1999**, *60* (4), R2181–R2184. https://doi.org/10.1103/PhysRevB.60.R2181.

(38) Kambhampati, P. Hot Exciton Relaxation Dynamics in Semiconductor Quantum Dots: Radiationless Transitions on the Nanoscale. *J. Phys. Chem. C* **2011**, *115* (45), 22089–22109. https://doi.org/10.1021/jp2058673.

(39) Ripberger, H.; Schnitzenbaumer, K.; Nguyen, L.; Ladd, D.; Levine, K.; Dayton, D.; Toney, M.; Cossairt, B. *Navigating the Potential Energy Surface of CdSe Magic-Sized Clusters: Synthesis and Interconversion of Atomically Precise Nanocrystal Polymorphs*; preprint; Chemistry, 2023. https://doi.org/10.26434/chemrxiv-2023-jzwm3.

(40) Mule, A. S.; Mazzotti, S.; Rossinelli, A. A.; Aellen, M.; Prins, P. T.; van der Bok, J. C.; Solari, S. F.; Glauser, Y. M.; Kumar, P. V.; Riedinger, A.; Norris, D. J. Unraveling the Growth Mechanism of Magic-Sized Semiconductor Nanocrystals. *J. Am. Chem. Soc.* **2021**, *143* (4), 2037–2048. https://doi.org/10.1021/jacs.0c12185.

(41) Zhang, C.; Xia, Y.; Zhang, Z.; Huang, Z.; Lian, L.; Miao, X.; Zhang, D.; Beard, M. C.; Zhang, J. Combination of Cation Exchange and Quantized Ostwald Ripening for Controlling Size Distribution of Lead Chalcogenide Quantum Dots. *Chem. Mater.* **2017**, *29* (8), 3615–3622. https://doi.org/10.1021/acs.chemmater.7b00411.

(42) Shrestha, A.; Spooner, N. A.; Qiao, S. Z.; Dai, S. Mechanistic Insight into the Nucleation and Growth of Oleic Acid Capped Lead Sulphide Quantum Dots. *Phys. Chem. Chem. Phys.* **2016**, *18* (20), 14055–14062. https://doi.org/10.1039/C6CP02119K.

(43) Park, N.; Beck, R. A.; Hoang, K. K.; Ladd, D. M.; Abramson, J. E.; Rivera-Maldonado, R. A.; Nguyen, H. A.; Monahan, M.; Seidler, G. T.; Toney, M. F.; Li, X.; Cossairt, B. M. Colloidal, Room-Temperature Growth of Metal Oxide Shells on InP Quantum Dots. *Inorg. Chem.* **2023**, *62* (17), 6674–6687. https://doi.org/10.1021/acs.inorgchem.3c00161.

(44) Hamachi, L. S.; Jen-La Plante, I.; Coryell, A. C.; De Roo, J.; Owen, J. S. Kinetic Control over CdS Nanocrystal Nucleation Using a Library of Thiocarbonates, Thiocarbamates, and Thioureas. *Chem. Mater.* **2017**, *29* (20), 8711–8719. https://doi.org/10.1021/acs.chemmater.7b02861.

(45) Foreman-Mackey, D.; Hogg, D. W.; Lang, D.; Goodman, J. Emcee: The MCMC Hammer. *PASP* **2013**, *125* (925), 306. https://doi.org/10.1086/670067.

(46) Goodman, J.; Weare, J. Ensemble Samplers with Affine Invariance. *CAMCoS* **2010**, *5* (1), 65–80. https://doi.org/10.2140/camcos.2010.5.65.

Chapter 5. Seeded Growth of Nanoscale Semiconductor Tetrapods: Generality and Cation Exchange

Significant portions of the following chapter have previously been published.[1]

5.1 INTRODUCTION

The synthesis of nanomaterials of various shapes and sizes is well established, and the importance of size and structure tunability is comprehensively understood.[2,3] However, methodologies for assembling multicomponent heterostructures with independently tuneable components are less ubiquitous.[4–6] Heterostructure design is an ideal strategy to tune charge carrier localisation for optoelectronic or charge separation applications. Choosing the appropriate material combinations allows Type-I, Type-II or Quasi Type-II band alignments.[7] Despite this, synthetic techniques to access a broad spectrum of material combinations with independently customisable dimensions are currently underdeveloped.

The simplest and most well-studied heterostructure is the spherical core/shell motif. These systems have an outer shell that serves as a protective layer capable of passivating surface traps and defects to enhance luminescence.[8] However, while the core/shell motif is a leading architecture for enhancing emission, this structure presents several disadvantages for applications where charge separation and extraction is necessary, such as photocatalysis. In a type-II core/shell heterostructure, one charge carrier localises to the shell and the other remains confined to the core. The carrier in the shell may be easily extracted but there is a physical and energetic barrier that impedes quenching of the carrier in the core. This may lead to deleterious effects on the stability of the nanocrystal and cause degradation.[9]

Dot-in-rod (DIR) heterostructures begin to address these challenges by having exposed or nominally shelled faces to enable more efficient quenching of charge carriers after separation.[10,11] The excited state lifetimes of DIRs are also typically longer than core/shells, due to better charge carrier separation, which increases the probability of quenching of both charge carriers. Within these motifs, the rod dimensions, dot dimensions, and dot location within the rod can be controlled.[12] However, DIRs require a wurtzite-phase QD to serve as a seed for rod growth, and many nanomaterials do not have easily accessible wurtzite crystal phases.[6,13,14] Composition variation in nanorods achieved via cation exchange broadens the number of accessible products, however wurtzite crystal structures are still necessary.[15] Thus, the spectrum of material combinations and the tunability of heterostructure rod architectures are limited to materials with accessible wurtzite crystal phases.

Tetrapod heterostructures represent a potentially versatile system capable of addressing the shortcomings of 0-D and 1-D structures. One major advantage of the tetrapod architecture is the customisability of the zinc blende phase QD seed. A wide variety of QDs can be straightforwardly synthesised in the zinc blende phase with tuneable sizes to serve as seeds.[16] In addition to controlling the composition and size of the seed, the arm length and width can also be modified independently.[4,5] Tetrapod heterostructures have been shown to have even longer excited state lifetimes than DIRs of comparable dimensions, due to four points of branching instead of two, leading to even better charge carrier separation.[6] However, it remains to be seen if this results in enhanced charge carrier extraction or improved photocatalytic activity.

Initial tetrapod syntheses were products of polytypism in which the small energy difference between zinc blende and wurtzite phases (>10 meV) enabled initial nucleation of spherical zinc blende seeds followed by elongation of wurtzite arms on the (111) facets of the seed.[17,18] Seeded

growth approaches have since received a significant amount of attention due to the ability to separate nucleation and growth steps, leading to higher monodispersity, yield, and control over optoelectronic properties.[4,16] In theory, seeded tetrapod architectures should be accessible from any QD with accessible (111) faces for (0001) wurtzite arm elongation. However, most tetrapod studies focus exclusively on materials from the II–VI family. It is also known that cation exchange between cadmium and zinc, copper, or indium in chalcogenide lattices is readily facilitated under typical nanomaterial growth conditions.[19–21] In this work, we expand the library of QDs that can seed tetrapod growth and we also re-examine the structures of known tetrapod systems in the context of cation exchange.[22–24]

First, we present a versatile synthetic approach to obtain tetrapod nanostructures with tuneable arm dimensions from a series of QD seeds (ZnTe, $CuInS_2$, and InP) and find that many cores are susceptible to cation migration and exchange. We next explored cation diffusion within a model tetrapod system formed from InP/ZnS core/shell seeds. Despite retaining the core's phosphide lattice, cation exchange could not be fully mitigated. Finally, we have demonstrated the first near-IR emissive tetrapod synthesised from II–V seeds while tuning the dimensions of the arms and core independently of one another.

5.2 General Synthesis of Core/CdS Tetrapods with Two Distinct Arm Morphologies

A library of tetrapods was synthesised using eight different starting QD seeds and the two reaction pathways depicted in Scheme 5.1 (16 unique tetrapod systems). We first synthesised and purified ZnTe, two sizes of $CuInS_2$ (3 nm and 6 nm), two morphologies of InP (spherical and tetrahedron), InP/ZnSeS, InP/ZnS, and Cd_3P_2 QDs as our starting library of seeds. We then

performed the two tetrapod syntheses in Scheme 5.1, varying the ratio of octadecylphosphonic acid (ODPA) to oleic acid. Higher amounts of more strongly binding ODPA yielded thinner CdS arms, as has been previously demonstrated in the literature.[5] We summarise the resulting dimensions of the tetrapods in Table 5.1. Images of the resulting tetrapods are shown in Figure 5.1 and 5.2. We hypothesise that the different arm lengths resulting from the same reaction conditions may be a result of inconsistent QD concentrations measured by sizing curves (less QDs grow longer arms), or reflective of lattice mismatch and ease of growth of CdS arms on QD facets (less mismatch yields shorter arms and higher yield).

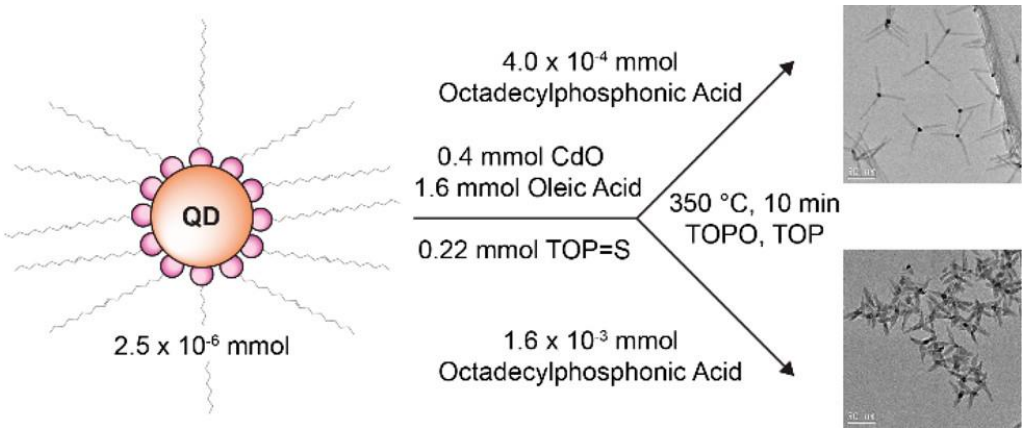

Scheme 5.1. General reaction conditions for the synthesis of thick and thin arm tetrapods. TEM of example thick and thin arm tetrapods grown from ZnTe seeds.

Table 5.1. Arm dimensions of library of 16 tetrapod heterostructures.

Seed	**Thin arms**		**Thick arms**	
	Length (nm)	**Width (nm)**	**Length (nm)**	**Width (nm)**
ZnTe	47 ± 5	5.9 ± 0.7	26 ± 4	9.1 ± 1.2
$CuInS_2$ (3 nm)	59 ± 17	5.5 ± 0.7	18 ± 2	9.2 ± 1.2
$CuInS_2$ (6 nm)	81 ± 15	4.6 ± 0.6	20 ± 4	9.6 ± 1.8
InP (sphere)	88 ± 10	5.5 ± 0.6	23 ± 4	10 ± 2
InP (tetrahedron)	49 ± 6	4.7 ± 0.6	22 ± 3	8 ± 1
InP/ZnSeS (thin shell)	16 ± 2	4.0 ± 0.6	12 ± 1	6.4 ± 0.9
InP/ZnS (thick shell)	12 ± 1	4.3 ± 0.5	10 ± 1	6.5 ± 0.9
Cd_3P_2	42 ± 5	5.2 ± 0.7	15 ± 2	7.7 ± 0.9

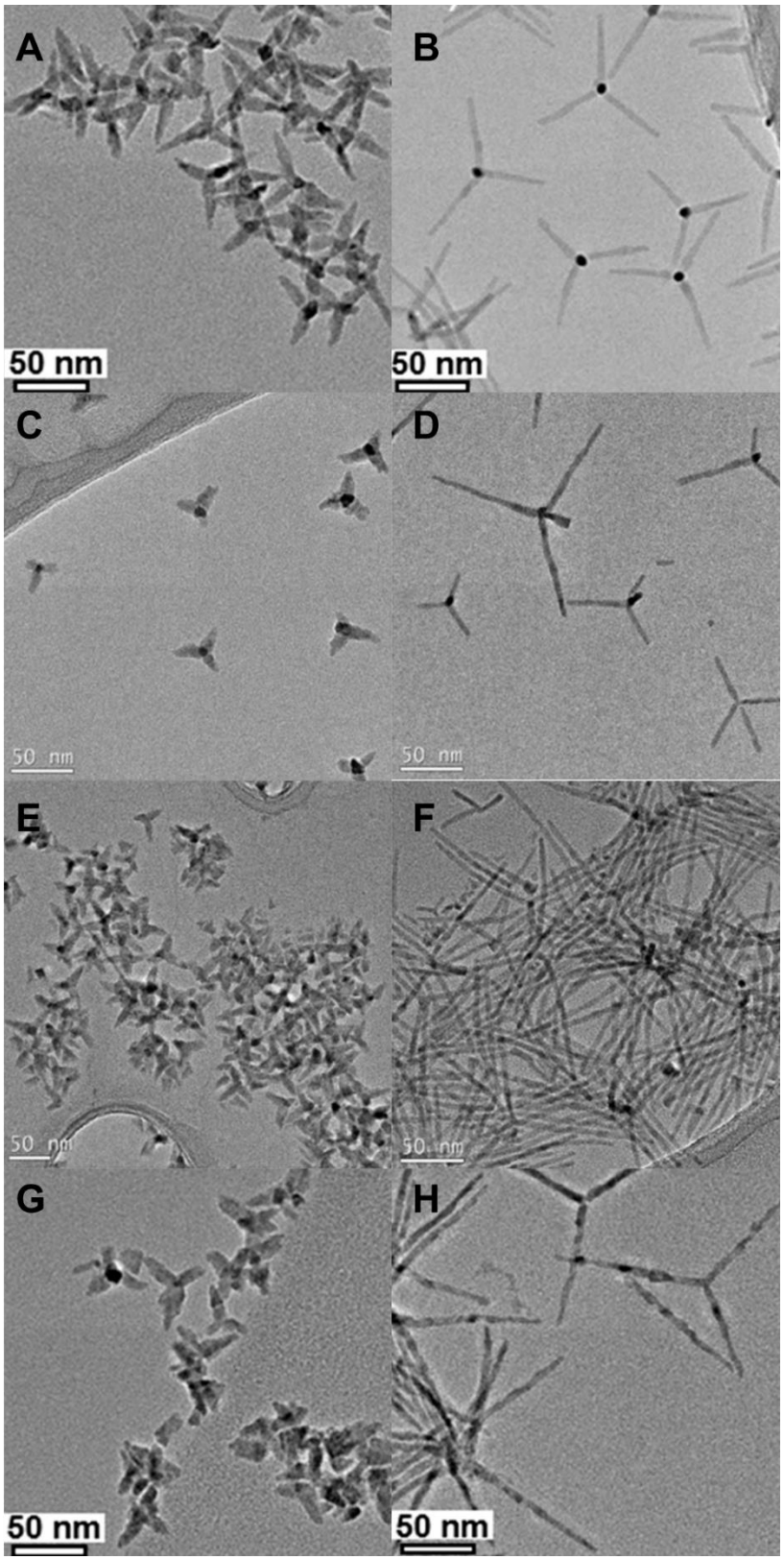

Figure 5.1. TEM images of thick (left column) and thin (right column) tetrapods grown from (A-B) ZnTe, (C-D) 3 nm $CuInS_2$, (E-F) 6 nm $CuInS_2$ and (G-H) spherical InP QD seeds.

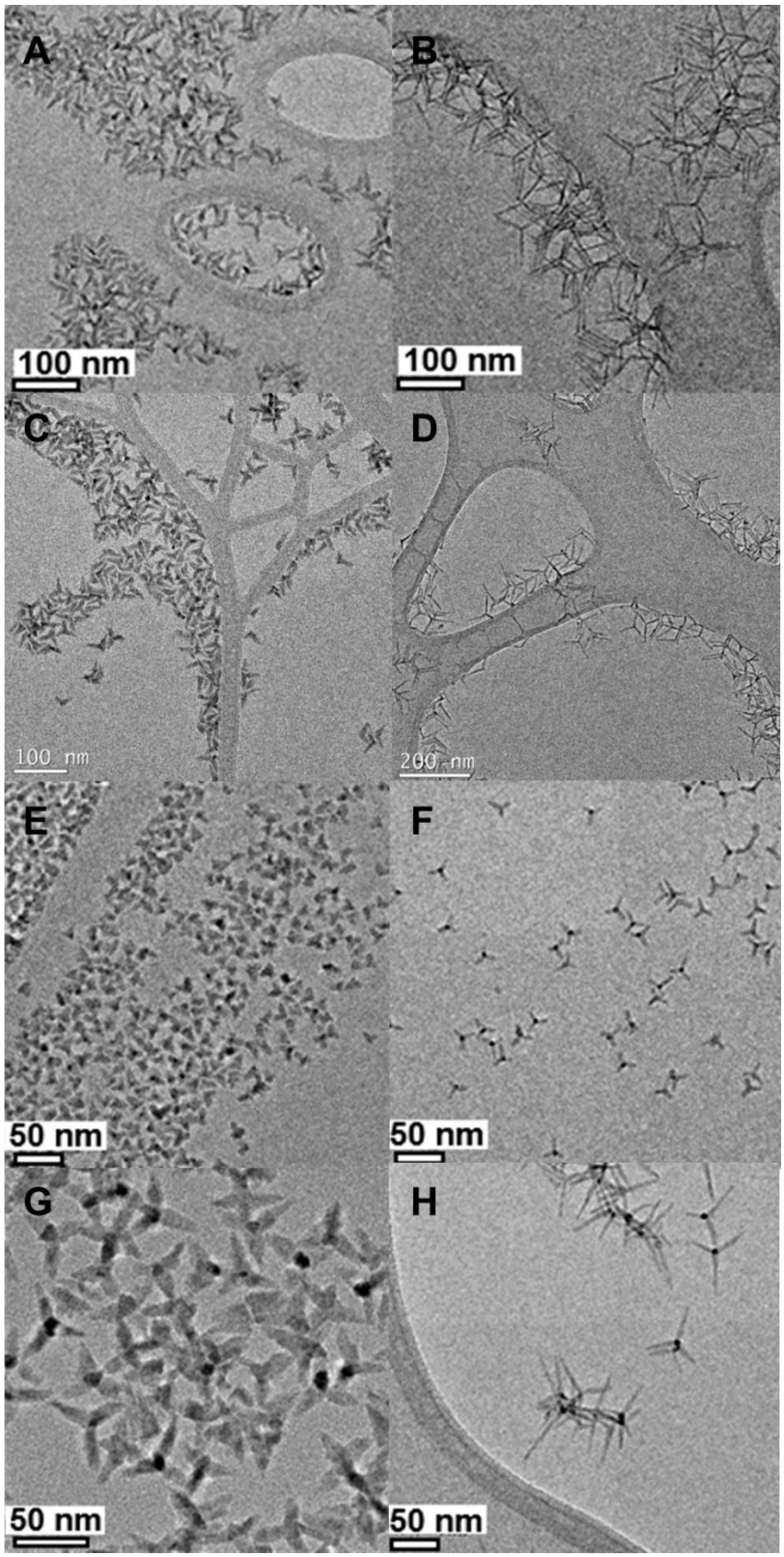

Figure 5.2. TEM images of thick (left column) and thin (right column) tetrapods grown from (A-B) tetrahedron InP, (C-D) InP/ZnSeS, (E-F) InP/ZnS and (G-H) Cd_3P_2.

Given the large volume taken up by the CdS arms compared to the QD cores, the optical properties of the tetrapods are dominated by CdS signal. Representative absorption and emission spectra of CdS arms are shown in Figure 5.3. The thin CdS arms appear to still be quantum-confined based on the visible higher energy transitions in the absorption spectrum, however the absorbance of the thick arms appear to be closer to bulk CdS. This makes sense as the Bohr radius of CdS is ~ 5.7 nm and all of the thick CdS arms are > 6 nm.

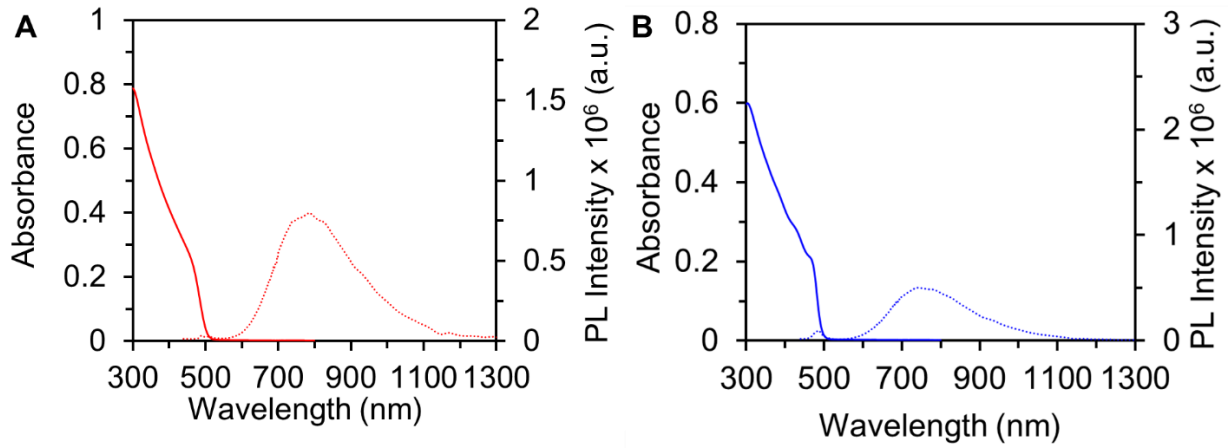

Figure 5.3. Absorbance and emission spectra of (A) thick and (B) thin CdS arms.

5.3 Evidence for Cation Exchange

We analysed our ZnTe/CdS architecture by ICP-OES and observed partial cation exchange in the final tetrapod products. Starting from 1.1:1 Zn:Te cores, this ratio diminished to 1:5 and 1:3 in the thick and thin arm morphologies, respectively. Elemental analysis of $CuInS_2$/CdS tetrapods by ICP-OES showed no detectable levels of indium, suggesting that all indium from the core was extruded during arm growth. The remaining copper content in both the thin and thick arm tetrapods assembled from both 3 and 6 nm CIS was 0.1%. Cation exchange between cadmium and zinc for

copper is known to occur in sulphide lattices.[20] Surprisingly, however, indium also appears to be mobile under our synthesis conditions.

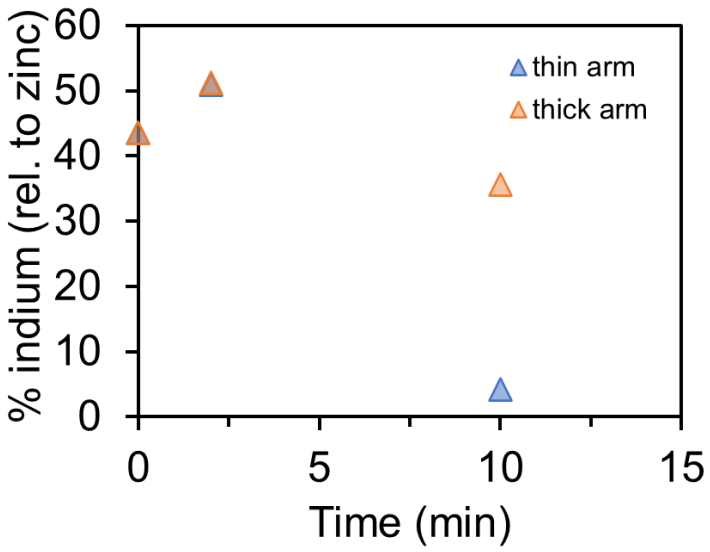

Figure 5.4. ICP-OES of indium and zinc over the course of tetrapod growth.

Our InP cores also did not retain their initial structure in the final tetrapods. Starting from 2:1 In:P cores, indium was not observed by ICP-OES within detectable limits, which may point to cation exchange whereby indium is removed and replaced with cadmium as seen previously.[19] Phosphorous was still detected at 3% of the structure. These observations suggest the core of the final tetrapod is primarily cadmium phosphide in character. The same outcome was observed when starting from thinly shelled (~1 monolayer) InP/ZnSeS QDs with a 69% quantum yield. Evaluation by ICP-OES reveals < 0.02% indium, indicating cation exchange is unimpeded by the presence of a thin shell. InP cores with ~8 monolayers of ZnS were next examined. We measured the composition of indium and zinc by ICP-OES over the course of tetrapod growth and found that by the end of the reaction, almost all of the indium is gone in thin tetrapods (Figure 5.4). The indium content is also decreased in the thick morphology.

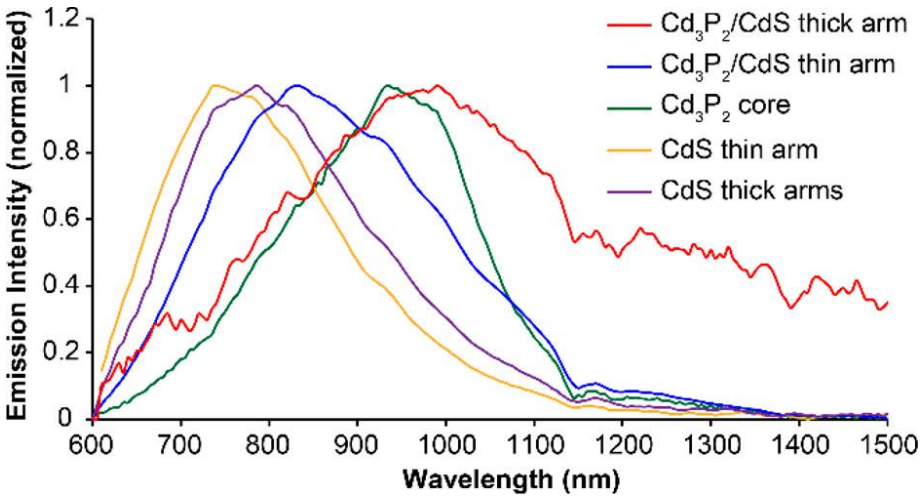

Figure 5.5. Emission of Cd_3P_2 nanocrystals, Cd_3P_2/CdS tetrapods, and CdS arms with thick and thin arm morphologies. Strong emission features from the Cd_3P_2 core are observed at 1100 nm (1.13 eV) prior to tetrapod assembly. This emission shifts up to 82 meV when incorporated into tetrapods.

One system where this general approach to heterostructure development was successful in retaining clean interfaces between the core and arm components is Cd_3P_2/CdS tetrapods. Evaluation of the optical properties of Cd_3P_2/CdS tetrapods confirms electronic communication between the arm and core components. In Figure 5.5, we show type-I emission in the case of thick Cd_3P_2/CdS that is distinct from arm emission. However, the emission from the thin arm tetrapods undergoes a hypsochromic shift. This may be due to etching of the seed's surface prior to arm growth, or increased asymmetrical strain induced by the thin arms relative to their thick arm counterparts. In any case, this emission is still distinct from arm emission and demonstrates electronic communication.

5.4 CONCLUSIONS

A seeded growth approach was used to obtain tetrapod nanostructures. Essentially almost any seed with accessible (111) planes could be used as a scaffold for tetrapod arm growth. This

approach extends beyond cubic cores to those with tetragonal lattices that have distorted (111) planes, such as $CuInS_2$. However, cation exchange accompanies the process of arm growth in many systems, precluding access to clean interfaces and desirable heterostructure band alignments. This work demonstrates that cation migration should always be a consideration when designing and characterising heterostructures since both processes are often favourable under the same reaction conditions as crystal growth. Ultimately, we use our general principles of arm growth to synthesise NIR emissive Cd_3P_2/CdS tetrapod heterostructures. Identifying conditions to suppress ion migration while still enabling wurtzite structure arm growth would be a productive next step in the synthesis of anisotropic nanoscale heterostructures.

5.5 EXPERIMENTAL

5.5.1 *Materials*

All glassware was dried in an oven overnight at 160 °C before use. All manipulations were performed by using standard Schlenk or glovebox techniques under dry N_2. Zinc acetate (99.99%), zinc chloride (99.99%), zinc stearate (technical grade), cadmium oxide (CdO, 99.9%), cadmium chloride (99.99%), cadmium acetate (Cd(OAc)2, 98%), indium acetate (99.99%), indium chloride (98%), copper iodide (≥99.5%), metallic tellurium (Te, 99.997%), selenium (Se, 99.999%), sulphur (S, 99.5%), superhydride ($LiBH(CH_2CH_3)_3$) solution in THF (1 M), tris(diethylamino)phosphine (97%), trioctylphosphine (TOP, 97%), octylamine (99%), oleic acid (OA, 90%), myristic acid (≥99%), dodecanethiol (98%), and oleylamine (70%) were purchased from Sigma-Aldrich and used as received without further purification. Octadecylphosphonic acid (ODPA, 99%) was purchased from PCI Synthesis and used as received. 1-Octadecene (ODE, 90%) was purchased from Sigma-Aldrich and distilled prior to use. Trioctylphosphine oxide (TOPO,

90%) was purchased from Sigma-Aldrich and twice recrystallized from acetonitrile until no impurities remained by ^{31}P and ^{1}H NMR spectroscopy. Methanol, ethanol, 2-propanol, acetonitrile, ethyl acetate, toluene, and pentane were purchased anhydrous and/or dried over CaH_2 and stored over 4 Å molecular sieves prior to use.

5.5.2 *Synthesis of ZnTe QDs*

ZnTe QDs (8 nm) were synthesized by using a modified literature procedure.[20] In a 50 mL three-neck flask, 0.26 g (1.4 mmol) of zinc acetate was mixed with 4 mL (12.7 mmol) of OA and 20 mL of 1-ODE. The mixture was degassed for at least 30 min before being heated to 200 °C under N_2. After 1 h a clear solution formed, and the temperature was dropped to 160 °C. The Te precursor was prepared by adding 1.6 mL of superhydride solution (1 M in THF) and 2 mL of oleylamine to 1.0 mL of TOP═Te (1.0 M Te in TOP). This tellurium precursor was stirred for 1 h at room temperature until the solution became homogeneous and subsequently injected rapidly into the zinc solution at 160 °C. The temperature was increased to 190 °C and maintained for 60 min before quenching the reaction by cooling to room temperature. Excess solvent and volatile organics were removed by vacuum distillation at 180 °C. The ZnTe nanorods were purified by repeated precipitation/resuspension in EtOH and pentane five times. The resulting ZnTe QDs have an aspect ratio of 2. Note of comparison to other procedures: similar procedures have been used to give ZnTe nanorods with aspect ratios of ≥3. The present synthesis stirred the tellurium precursor for longer times (1 h as opposed to 20 min), and vacuum distillation was performed at a higher temperature (180 °C vs 150 °C).

5.5.3 *Synthesis of Copper Indium Sulphide QDs*

$CuInS_2$ QDs were synthesized by using a literature procedure.[25] First, 73 mg (0.25 mmol) of indium acetate, 47.5 mg (0.25 mmol) of copper iodide, and 4 mL of dodecanethiol were added to a 50 mL three-neck flask. The flask was purged with N_2 for 30 min and subsequently heated while stirring to 120 °C over 20 min. The solution was maintained at 120 °C for an additional 10 min, until a clear yellow solution was formed. The solution was then heated to 230 °C and gradually changed colour from yellow to dark red. After refluxing for a set time (1–30 min), the reaction was quenched by removing the flask from heat.

5.5.4 *Synthesis of Spherical InP QDs*

Indium phosphide QDs were synthesized via a two-step synthetic procedure reported previously.[26] Briefly, 0.93 g (3.20 mmol) of indium acetate and 2.65 g (11.6 mmol) of myristic acid were heated under vacuum at 100 °C in a 100 mL three-neck flask for 12 h to generate indium myristate. After indium myristate was formed, the apparatus was placed under N_2, and 20 mL of toluene was added. This solution was heated to 110 °C, and a mixture of 465 μL of tris(trimethylsilyl)phosphine ($P(SiMe_3)_3$) and 10 mL of toluene was quickly injected to form InP magic size clusters (MSCs). InP MSC formation was monitored by UV–vis absorbance until no changes were observed. Purification of MSCs was achieved by repeated precipitation with acetonitrile and resuspension in toluene.

To obtain 3.0 nm InP QDs, 200 mg of MSCs was dissolved in 2 mL of ODE and injected into a 100 mL three-neck flask with 38 mL of additional ODE at 270 °C. Growth for 20 min yielded 3.0 nm InP nanoparticles. Excess ODE was removed by vacuum distillation at 150 °C, and QDs were purified by multiple resuspensions in toluene and precipitation with ethanol.

5.5.5 *Synthesis of Tetrahedron InP and InP/ZnS QDs*

InP/ZnS core/shell QDs were prepared by following a procedure by Tessier et al.[27] Briefly, 100 mg (0.45 mmol) of indium (III) chloride and 300 mg (2.2 mmol) of zinc (II) chloride were mixed in 5.0 mL (15 mmol) of technical grade oleylamine in a 50 mL three-neck flask. The reaction mixture was degassed at 120 °C for an hour and then heated to 180 °C under N_2. At 180 °C, 0.45 mL (1.6 mmol) of tris(diethylamino)phosphine was swiftly injected. For tetrahedral InP QDs, quench reaction after 30 min.

For core/shell InP/ZnS, at 20 min, 1 mL of TOP-S (2.2 M) was dropwise injected. At 60 min, the temperature was increased from 180 to 200 °C. At 120 min, 1 g of Zn(stearate)$_2$ in 4 mL of octadecene (ODE) was dropwise injected, and the temperature was increased from 200 to 220 °C. At 150 min, 0.7 mL of TOP═S (2.2 M) was dropwise injected, and the temperature was increased from 220 to 240 °C. At 180 min, 0.5 g of Zn(stearate)$_2$ in 2 mL of ODE was dropwise injected, and the temperature was increased from 240 to 260 °C. At 210 min, the reaction was arrested and cooled to room temperature. Both InP and InP/ZnS were purified by repeated precipitation and resuspension in 2-propanol and toluene, respectively, four times. Indium phosphide tetrahedron-shaped quantum dots were obtained by quenching the reaction after 20 min of InP growth instead of adding TOP-S.

5.5.6 *Synthesis of InP/ZnSeS QDs*

InP/ZnSeS core/shell QDs were prepared according to a previous report.[28] Briefly, 50 mg (0.003 mmol) of myristate-ligated InP MSCs was dissolved in 1 mL of ODE and injected into a 25 mL three-neck flask with 5 mL of additional ODE at 290 °C. Growth for 15 min yielded InP cores as determined by UV–vis spectroscopy. The reaction temperature was reduced to 220 °C,

and a solution of zinc stearate prepared by suspending 0.171 g (1.124 mmol) in 5 mL of ODE was injected into the reaction. After 15 min after temperature equilibration, TOP═Se (0.112 mL, 0.112 mmol) was added slowly over the course of 1 min, and the reaction equilibrated for 20 min. Next, TOP═S (1.011 mL, 1.011 mmol) was added slowly over the course of 5 min, and the reaction equilibrated for 15 min. The temperature was then set to 300 °C, and the photoluminescence was monitored until no further increases were measured (40 min following TOP═S injection). The reaction was cooled to room temperature, and the ODE was removed under vacuum distillation. The solid was suspended in toluene and centrifuged (7000 rpm for 10 min) to isolate the supernatant, which was then precipitated with acetonitrile. The precipitate was then resuspended in minimal toluene and purified by gel permeation chromatography.

5.5.7 *Synthesis of Cd_3P_2 QDs*

The 3.5 nm Cd_3P_2 cores were synthesized based on a prior report.[29] Briefly, 0.692 g (3.0 mmol) of $Cd(OAc)_2$ and 0.910 g (7.05 mmol) of octylamine were added to 8 mL of toluene in a 50 mL three-neck flask. This solution was heated 30 °C, and 2 mL of ($P(SiMe_3)_3$) solution (0.5 M in toluene) was injected rapidly. The reaction temperature was maintained at 30 °C for 24 h before the solution was removed from heat, precipitated with ethanol, and resuspended in toluene five times.

5.5.8 *Synthesis of Tetrapods with CdS Arms*

Core/CdS tetrapod heterostructures were synthesized by using modifications of existing literature procedures.[5] Briefly, 2.65 g of TOPO (99%), 0.05175 g of CdO, 0.5 mL OA, and either 135 mg of ODPA (for thin arms) or 54 mg of ODPA (for thick arms) were degassed at 150 °C for

1.5 h in a 50 mL three-neck flask. The reaction mixture was heated to 350 °C under N_2, and the reddish-brown solution turned colourless. Separately, a stock solution of TOP═S was made from 70 mg of sulphur with 6 mL of TOP (0.364 M). 0.6 mL of TOP═S was mixed with 2.5 nmol of QDs as determined by the optical absorbance of the QD solution. Upon reaching the desired injection temperature of 350 °C, 1.8 mL of TOP was added, and the temperature was allowed to recover to 350 °C before the mixture of TOP═S and QDs was swiftly injected. Anisotropic CdS arms were grown at this temperature for 10 min. The heating mantle was removed, and the solution was cooled to room temperature. The core/CdS tetrapods were purified by repeated precipitation in methanol and redispersion in toluene five times.

5.5.9 *Characterisation methods*

UV-Vis spectra were collected on a Cary 5000 spectrophotometer from Agilent. Fluorescence spectra were collected on a Horiba Jobin Yvon FluoroMax4 fluorescence spectrophotometer. Near-infrared photoluminescence was acquired on a home-built spectrometer by using amplitude-modulated excitation and phase-sensitive detection. Emission was separated with a monochromator and then detected by using a dual-band Si/InGaAs photodetector, and all traces were corrected for detector response. Samples were irradiated with a modulated (200 Hz) 365 nm LED or 550 nm LED by using appropriate long pass filters to remove scattered pump light prior to entrance into the monochromator. A PerkinElmer Optima 8300 inductively coupled plasma–optical emission spectrophotometer was used for elemental analysis. TEM images were collected on an FEI Tecnai G2 F20 microscope.

5.6 REFERENCES

(1) Enright, M. J.; Dou, F. Y.; Wu, S.; Rabe, E. J.; Monahan, M.; Friedfeld, M. R.; Schlenker, C. W.; Cossairt, B. M. Seeded Growth of Nanoscale Semiconductor Tetrapods: Generality and the Role of Cation Exchange. *Chem. Mater.* **2020**, *32* (11), 4774–4784. https://doi.org/10.1021/acs.chemmater.0c01407.

(2) Manna, L.; Scher, E. C.; Alivisatos, A. P. Synthesis of Soluble and Processable Rod-, Arrow-, Teardrop-, and Tetrapod-Shaped CdSe Nanocrystals. *J. Am. Chem. Soc.* **2000**, *122* (51), 12700–12706. https://doi.org/10.1021/ja003055+.

(3) Peng, X.; Manna, L.; Yang, W.; Wickham, J.; Scher, E.; Kadavanich, A.; Alivisatos, A. P. Shape Control of CdSe Nanocrystals. *Nature* **2000**, *404* (6773), 59–61. https://doi.org/10.1038/35003535.

(4) Mishra, N.; Vasavi Dutt, V. G.; Arciniegas, M. P. Recent Progress on Metal Chalcogenide Semiconductor Tetrapod-Shaped Colloidal Nanocrystals and Their Applications in Optoelectronics. *Chem. Mater.* **2019**, *31* (22), 9216–9242. https://doi.org/10.1021/acs.chemmater.8b05363.

(5) Mishra, N.; Wu, W.-Y.; Srinivasan, B. M.; Hariharaputran, R.; Zhang, Y.-W.; Chan, Y. Continuous Shape Tuning of Nanotetrapods: Toward Shape-Mediated Self-Assembly. *Chem. Mater.* **2016**, *28* (4), 1187–1195. https://doi.org/10.1021/acs.chemmater.5b04803.

(6) Talapin, D. V.; Nelson, J. H.; Shevchenko, E. V.; Aloni, S.; Sadtler, B.; Alivisatos, A. P. Seeded Growth of Highly Luminescent CdSe/CdS Nanoheterostructures with Rod and Tetrapod Morphologies. *Nano Lett.* **2007**, *7* (10), 2951–2959. https://doi.org/10.1021/nl072003g.

(7) Reiss, P.; Protière, M.; Li, L. Core/Shell Semiconductor Nanocrystals. *Small* **2009**, *5* (2), 154–168. https://doi.org/10.1002/smll.200800841.

(8) Van Avermaet, H.; Schiettecatte, P.; Hinz, S.; Giordano, L.; Ferrari, F.; Nayral, C.; Delpech, F.; Maultzsch, J.; Lange, H.; Hens, Z. Full-Spectrum InP-Based Quantum Dots with Near-Unity Photoluminescence Quantum Efficiency. *ACS Nano* **2022**, *16* (6), 9701–9712. https://doi.org/10.1021/acsnano.2c03138.

(9) Bang, J. H.; Kamat, P. V. Quantum Dot Sensitized Solar Cells. A Tale of Two Semiconductor Nanocrystals: CdSe and CdTe. *ACS Nano* **2009**, *3* (6), 1467–1476. https://doi.org/10.1021/nn900324q.

(10) Bridewell, V. L.; Alam, R.; Karwacki, C. J.; Kamat, P. V. CdSe/CdS Nanorod Photocatalysts: Tuning the Interfacial Charge Transfer Process through Shell Length. *Chem. Mater.* **2015**, *27* (14), 5064–5071. https://doi.org/10.1021/acs.chemmater.5b01689.

(11) Wu, K.; Hill, L. J.; Chen, J.; McBride, J. R.; Pavlopolous, N. G.; Richey, N. E.; Pyun, J.; Lian, T. Universal Length Dependence of Rod-to-Seed Exciton Localization Efficiency in Type I

and Quasi-Type II CdSe@CdS Nanorods. *ACS Nano* **2015**, *9* (4), 4591–4599. https://doi.org/10.1021/acsnano.5b01245.

(12) Kim, D.; Lee, Y. K.; Lee, D.; Kim, W. D.; Bae, W. K.; Lee, D. C. Colloidal Dual-Diameter and Core-Position-Controlled Core/Shell Cadmium Chalcogenide Nanorods. *ACS Nano* **2017**, *11* (12), 12461–12472. https://doi.org/10.1021/acsnano.7b06542.

(13) Dacal, L. C. O.; Cantarero, A. Ab Initio Electronic Band Structure Calculation of InP in the Wurtzite Phase. *Solid State Communications* **2011**, *151* (10), 781–784. https://doi.org/10.1016/j.ssc.2011.03.003.

(14) De, A.; Pryor, C. E. Predicted Band Structures of III-V Semiconductors in the Wurtzite Phase. *Phys. Rev. B* **2010**, *81* (15), 155210. https://doi.org/10.1103/PhysRevB.81.155210.

(15) Enright, M. J.; Sarsito, H.; Cossairt, B. M. Kinetically Controlled Assembly of Cadmium Chalcogenide Nanorods and Nanorod Heterostructures. *Mater. Chem. Front.* **2018**, *2* (7), 1296–1305. https://doi.org/10.1039/C8QM00056E.

(16) Fiore, A.; Mastria, R.; Lupo, M. G.; Lanzani, G.; Giannini, C.; Carlino, E.; Morello, G.; De Giorgi, M.; Li, Y.; Cingolani, R.; Manna, L. Tetrapod-Shaped Colloidal Nanocrystals of II−VI Semiconductors Prepared by Seeded Growth. *J. Am. Chem. Soc.* **2009**, *131* (6), 2274–2282. https://doi.org/10.1021/ja807874e.

(17) Manna, L.; Milliron, D. J.; Meisel, A.; Scher, E. C.; Alivisatos, A. P. Controlled Growth of Tetrapod-Branched Inorganic Nanocrystals. *Nature Mater* **2003**, *2* (6), 382–385. https://doi.org/10.1038/nmat902.

(18) Lim, J.; Bae, W. K.; Park, K. U.; zur Borg, L.; Zentel, R.; Lee, S.; Char, K. Controlled Synthesis of CdSe Tetrapods with High Morphological Uniformity by the Persistent Kinetic Growth and the Halide-Mediated Phase Transformation. *Chem. Mater.* **2013**, *25* (8), 1443–1449. https://doi.org/10.1021/cm3035592.

(19) Stein, J. L.; Steimle, M. I.; Terban, M. W.; Petrone, A.; Billinge, S. J. L.; Li, X.; Cossairt, B. M. Cation Exchange Induced Transformation of InP Magic-Sized Clusters. *Chem. Mater.* **2017**, *29* (18), 7984–7992. https://doi.org/10.1021/acs.chemmater.7b03075.

(20) Enright, M. J.; Sarsito, H.; Cossairt, B. M. Quantifying Cation Exchange of Cd2+ in ZnTe: A Challenge for Accessing Type II Heterostructures. *Chem. Mater.* **2017**, *29* (2), 666–672. https://doi.org/10.1021/acs.chemmater.6b04215.

(21) Groeneveld, E.; Witteman, L.; Lefferts, M.; Ke, X.; Bals, S.; Van Tendeloo, G.; de Mello Donega, C. Tailoring ZnSe–CdSe Colloidal Quantum Dots via Cation Exchange: From Core/Shell to Alloy Nanocrystals. *ACS Nano* **2013**, *7* (9), 7913–7930. https://doi.org/10.1021/nn402931y.

(22) Wu, W.-Y.; Li, M.; Lian, J.; Wu, X.; Yeow, E. K. L.; Jhon, M. H.; Chan, Y. Efficient Color-Tunable Multiexcitonic Dual Wavelength Emission from Type II Semiconductor Tetrapods. *ACS Nano* **2014**, *8* (9), 9349–9357. https://doi.org/10.1021/nn503343c.

(23) Kim, B.; Kim, K.; Kwon, Y.; Lee, W.; Shin, W. H.; Kim, S.; Bang, J. CuInS2/CdS-Heterostructured Nanotetrapods by Seeded Growth and Their Photovoltaic Properties. *ACS Appl. Nano Mater.* **2018**, *1* (6), 2449–2454. https://doi.org/10.1021/acsanm.8b00250.

(24) Xie, R.; Kolb, U.; Basché, T. Design and Synthesis of Colloidal Nanocrystal Heterostructures with Tetrapod Morphology. *Small* **2006**, *2* (12), 1454–1457. https://doi.org/10.1002/smll.200600298.

(25) Booth, M.; Brown, A. P.; Evans, S. D.; Critchley, K. Determining the Concentration of CuInS2 Quantum Dots from the Size-Dependent Molar Extinction Coefficient. *Chem. Mater.* **2012**, *24* (11), 2064–2070. https://doi.org/10.1021/cm300227b.

(26) Gary, D. C.; Terban, M. W.; Billinge, S. J. L.; Cossairt, B. M. Two-Step Nucleation and Growth of InP Quantum Dots via Magic-Sized Cluster Intermediates. *Chem. Mater.* **2015**, *27* (4), 1432–1441. https://doi.org/10.1021/acs.chemmater.5b00286.

(27) Tessier, M. D.; Dupont, D.; De Nolf, K.; De Roo, J.; Hens, Z. Economic and Size-Tunable Synthesis of InP/ZnE (E = S, Se) Colloidal Quantum Dots. *Chem. Mater.* **2015**, *27* (13), 4893–4898. https://doi.org/10.1021/acs.chemmater.5b02138.

(28) Friedfeld, M. R.; Stein, J. L.; Johnson, D. A.; Park, N.; Henry, N. A.; Enright, M. J.; Mocatta, D.; Cossairt, B. M. Effects of Zn2+ and Ga3+ Doping on the Quantum Yield of Cluster-Derived InP Quantum Dots. *The Journal of Chemical Physics* **2019**, *151* (19), 194702. https://doi.org/10.1063/1.5126971.

(29) Ojo, W.-S.; Xu, S.; Delpech, F.; Nayral, C.; Chaudret, B. Room-Temperature Synthesis of Air-Stable and Size-Tunable Luminescent ZnS-Coated Cd3P2 Nanocrystals with High Quantum Yields. *Angewandte Chemie International Edition* **2012**, *51* (3), 738–741. https://doi.org/10.1002/anie.201104864.

VITA

Florence Yimin Dou was born and raised in Trinidad and Tobago to Chinese immigrant parents. Her parents and older brother moved from Guangzhou, China in 1991. She made her own move to the US to attend Trinity College in Hartford, CT majoring in Chemistry and working in Dr. Timothy Curran's group. After, she worked for two years as a Research Technician at Dana-Farber Cancer Institute in Boston, MA in Dr. Bruce Spiegelman's group. She then made the big move out West to attend the University of Washington. In her spare time, Florence is dedicated to advancing her tennis career. She also loves eating, karaoke, travelling, and spending time doing anything or nothing with loved ones.